博士論文

微生物型ロドプシンのレチナール結合部位の構造に関する固体 NMR 研究

Solid-state NMR study on structure of retinal-binding site in microbial rhodopsin

横浜国立大学大学院

工学府

Yokohama National University
Graduate School of Engineering

重田 安里寿

Arisu SHIGETA

2018 年 3 月

Contents

List of publications

Doctoral Dissertation

1. K. Oshima, **A. Shigeta**, Y. Makino, I. Kawamura, T. Okitsu, A. Wada, S. Tuzi, T. Iwasa, A. Naito. "Characterization of photo-intermediates in the photo-reaction pathways of bacteriorhodopsin Y185F mutant using in situ photo-irradiation solid-state NMR spectroscopy" (2015) *Photochem. Photobiol. Sci.,* **14**, 1694-1702.

2. **A. Shigeta**, S. Ito, K. Inoue, T. Okitsu, A. Wada, H. Kandori, I. Kawamura. "Solid-state NMR structural study of retinal-binding pocket of sodium ion pump rhodopsin" (2017) *Biochemistry*, **56**, 543-550.

3. **A. Shigeta**, S. Ito, R. Kaneko, S. Tomida, K. Inoue, H. Kandori, I. Kawamura. "Long-distance perturbation on Schiff base–counterion interaction by His30 and the extracellular Na^+-binding site in *Krokinobacter* rhodopsin 2" (2018) *Phys. Chem. Chem. Phys.*, **20**, 8450-8455.

Reference Articles

4. R. Matsui, N. Uchida, M. Ohtani, K. Yamada, **A. Shigeta**, I. Kawamura, T. Aida, Y. Ishida. "Magnetically Alignable Bicelles with Unprecedented Stability by Tunable Surfactants Derived from Cholic Acid." (2016) *ChemPhysChem,* **17**, 3916-3922.

Abbreviations

AR	Archaerhodopsin
ASR	*Anabaena* sensory rhodopsin
ATP	adenosine triphosphate
ATR	Attenuated Total Reflection
BO	Bacterioopsin
BR, *Hs*BR	Bacteriorhodopsin, *H. salinarum* bacteriorhodopsin
CCCP	carbonylcyanide-m-chlorophenylhydrazone
CP-MAS	Cross polarization-Magic Angle Spinning
ChR	Channelrhodopsin
DARR	dipolar-assisted rotational resonance
DDM	n-dodecyl-b-D-maltoside
DNP	dynamic nuclear polarization
FID	free induction decays
FR	*Fulvimarina pelagi* rhodopsin
FTIR	Fourier transform infrared spectroscopy
G state	ground state
GLR	*Gillisia limnaea* rhodopsin
GPCR	G-protein coupled receptor
GPR	green proteorhodopsin
GR	*Gloeobacter* rhodopsin
HR	halorhodopsin
*Hs*HR	*Halobacterium salinarum* halorhodopsin
*Hw*BR	*Haloquadratum walsbyi* bacteriorhodopsin
I-SAD	iodide-single-wavelength anomalous diffraction
*Ia*NaR	*Indibacter alkaliphilus* Na-pump rhodopsin
KR1	*Krokinobacter* rhodopsin 1
KR2	*Krokinobacter* rhodopsin 2
MD	molecular dynamics
MR	Middle rhodopsin
NMR	Nuclear Magnetic Resonance
*Np*HR	*Natronomonas pharaonis* halorhodopsin
*Np*SRII	*Natronomonas pharaonis* Sensory Rhodopsin II
PDSD	proton-driven spin diffusion
PEG	polyethylene glycol
PM	purple membrane
POPE	1-palmitoyl-2-oleoyl-sn-glycero-3-phosphoethanolamine
POPG	1-palmitoyl-2-oleoyl-sn-glycero-3-phospho(1′-rac-glycerol)
PR	Proteorhodopsin
PRG	proton release group
(p)SB	(protonated) Schiff base
RF	Radio-frequency
Ret	retinal
*Sy*HR	*Synechocystis* halorhodopsin
TMS	tetramethylsilane
TPP^+	tetraphenylphosphonium bromide
TR	Thermophilic rhodopsin

Introduction

Rhodopsins

Microbial and animal rhodopsins

One of the membrane protein, rhodopsin, is a photoreceptor protein which converts lights to an energy source. Rhodopsins are classified to microbial and animal rhodopsin, termed as type-I and type-II as well, respectively. Animal rhodopsin exists in rod and cone in eye and functions as a visual pigment. Rhodopsin-like G-protein coupled receptor (GPCR) is known as well which classified in a member of family A in GPCRs, which utilizes light, small molecules and peptides as ligands.[1] Structural change of one of the protein in family A, rhodopsin, to meta-rhodopsin II occurs by photo-isomerization from 11-*cis* to all-*trans* and then activates trimeric G-protein to transmit the photo signal. They share common structure of seven transmembrane α-helices with bound retinal, aldehyde of vitamin A, inside the protein and its N- and C-terminus facing out- and inside- of the cell, respectively. In addition to that, animal rhodopsins have short 8th helix at cytoplasmic side and some microbial rhodopsins have N-helix at extracellular side. Retinal inside the protein is bound to side chain of Lys locates in the middle of the protein. The light absorption by this retinal is a generally first movement in expression of function. Retinal in microbial rhodopsin takes all-*trans* conformation in dark state and isomerizes to 13-*cis*, where in animal rhodopsin changes from 11-*cis* to all-*trans* by light excitation.[2]

Variety in microbial rhodopsins

Recent metagenomic analysis since 2000 expanded the discovery of new-functional rhodopsins from microorganism. The first discovery of rhodopsin was in 1876 where the visual rhodopsin was found. After a decade, bacteriorhodopsin was found as a first microbial rhodopsin. The study on microbial rhodopsin followed by the structural determination by electron microscopy in 1971, discovery of chloride pumping halorhodopsin (HR) in 1977-1981[3–7] and sensory rhodopsin in 1984 and structural determination of bacteriorhodopsin by X-ray crystallographic analysis in 1997 as well as spectroscopic studies for functional analysis and structural mechanisms. Until 2000 the target protein was limited although it expanded widely followed by the discovery of eubacterial proton pump in 2000, cation channelrhodopsin in 2002[8], eukaryotic proton pump rhodopsin with carotenoid antenna called Xanthorhodopsin (XR) in 2005[9], thermophilic proton pump rhodopsin called thermophilic

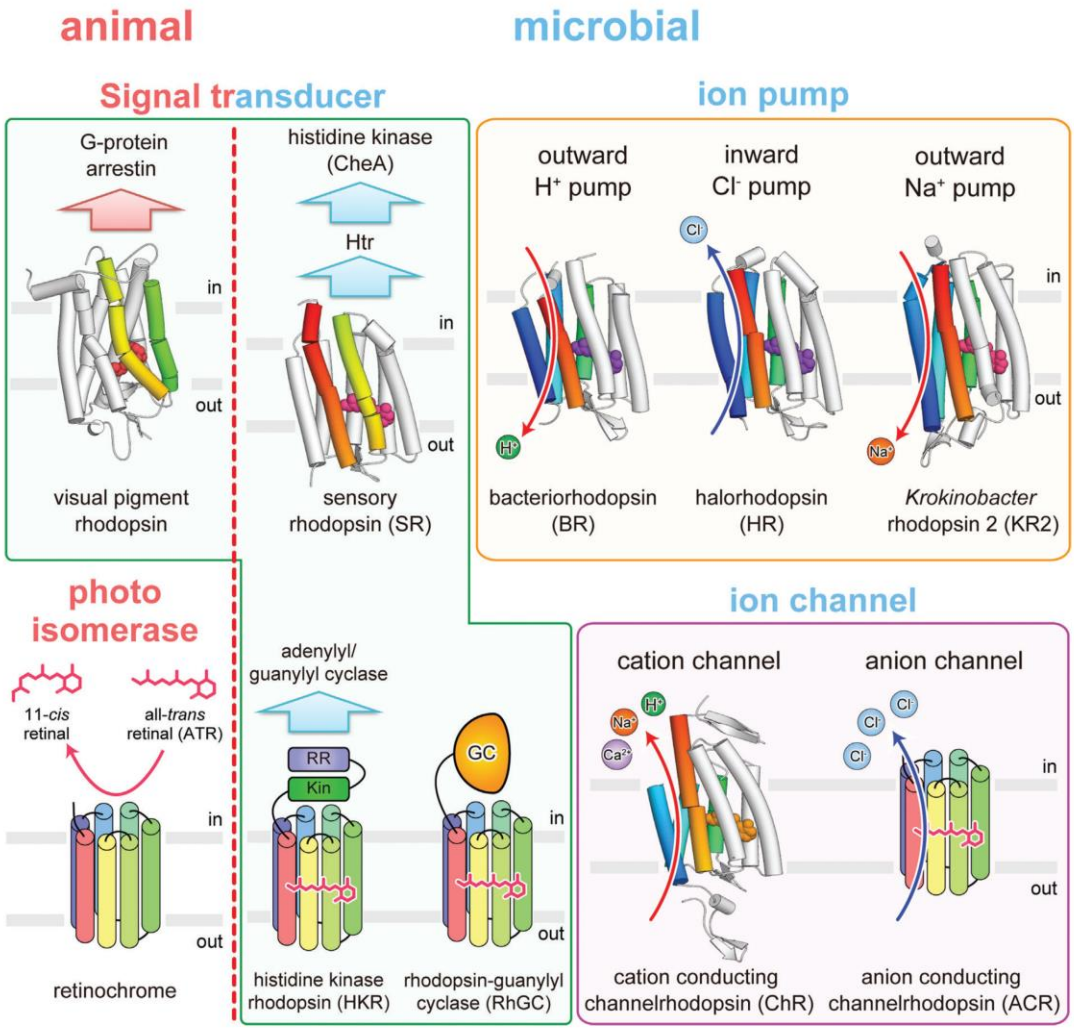

Figure 1. Functional classification of rhodopsin family proteins.
Structures of bovine rhodopsin (PDB code: 1F88), sensory rhodopsin II (PDB code: 1H2S), bacteriorhodopsin (PDB code: 1C3W), halorhodopsin (PDB code: 1E12), *Krokinobacter* rhodopsin 2 (KR2; PDB ID: 3X3C), chimeric channelrhodopsin (C1C2) (PDB code: 3UG9) are shown as cylinder models. The colored cylinders denote helices forming the ion-conducting pathway in BR, HR, KR2, and ChR, and helices which bind to the respective signal transducers in bovine rhodopsin and SRII. Adapted from [10].

---

rhodopsin (TR) in 2013[11], and sodium ion pump rhodopsin, *Krokinobacter* rhodopsin (KR2), in 2013[12]. Now more than 10000 microbial rhodopsins are found in genome of archaea, bacteria and eukaryotes and the functions varies from ion pump, ion channel to sensor.[13] Ion pumps control the transportation of ion into and out of cell against potential gradient while channels let the potential gradient to be cancelled. Sensors form complex with transducer to transmit the light-induced signals to flagellar motor.

Bacteriorhodopsin

One of the most well-known microbial rhodopsins is bacteriorhodopsin (BR) from *Halobacterium salinarum* which expresses light-driven proton pump[14,15] and generates H^+-gradient in cell to activate adenosine triphosphate (ATP) synthase.[16,17] This protein forms patch of hexagonal lattice in *H. salinarum* cellular membrane.[17] There is only one protein present in this membrane fragment[18] which is called purple membrane (PM), thus, it can be easily purified to obtain pure bacteriorhodopsin with homo-trimer.[17,19] Oesterhelt and Stoekenius revealed that this purple color is caused by the retinal[20] bound to Lys216 side chain in helix 7 via Schiff base[17] and locates in the middle of 7-transmembrane helices.[21] As this protein takes similar structure of seven helices and covalent retinal to visual rhodopsins, structural and mechanistic research has been conducted into the details.

Retinal bound in microbial rhodopsin takes mainly all-*trans* conformation, however, bacteriorhodopsin has two conformations of retinal in dark: all-*trans* (13-*trans*, 15-*anti*) and 13-*cis* (13-*cis*, 15-*syn*) conformations.[22] Two conformations are in equilibrium and the ratio of these conformations in dark is 1:1 called dark-adapted state.[23] The unidirectional transmembrane ion transport is driven by isomerization of the retinal[24] and the retinal conformation changes to ~100% all-*trans* by light irradiation which is called light-adapted state. Conformational change to all-*trans* is followed by the change to 13-*cis* (13-*cis*, 15-*anti*) conformation at J or K-intermediate and then photocyclic pathway of proton pumping activity.

First structure of bacteriorhodopsin was revealed by Henderson et al. using cryo-electron microscopy reported in 1975.[25] The three-dimensional potential map showed the packing of bacteriorhodopsin forming trimer in a purple membrane. A single molecule of bacteriorhodopsin showed seven-transmembrane structure, however, the resolution is limited showing 7 Å, which eliminates the conformation of retinal and residues. Structural study was followed by some groups and the conformational information of residues were revealed by crystallographic study and cryo-electron microscopy.[26–29] In 1999, Luecke et al. revealed the full structure of bacteriorhodopsin at the resolution of 1.55 Å (PDB code: 1C3W)[21] This enabled to see the protein inner structure including water molecules forming hydrogen bonds with surrounding residues which interactions are essential for understanding of proton pump as its transportation occurs with proton hopping.[30–32] In this crystal structure, only all-*trans* retinal was shown. 13-*cis* retinal contained structure was later shown by Nishikawa et al.[33] and Patzelt et al.[34] by means of crystallography and NMR, respectively.

This protein functions with light; therefore, the structural change after the light-irradiation should occur. The photo-intermediates were distinguished by visible spectroscopy.[35–37] The maximum absorption wavelengths of the states are 568 nm for ground state of all-*trans*, 548 nm for ground state of 13-*cis*, 590 nm for K, 550 nm for L, 412 nm for M, 560 nm for N and 640 nm for O state. Excitation from ground state to K-intermediate occurs in ~4 ps, then the relaxation time of K, L, M, N and O are ~1 μs, ~40 μs, ~5 ms, ~5 ms, and ~5 ms, respectively.[38]

Unidirectional proton transportation between key residues starts with photon absorption of retinal and retinal isomerization followed by the contiguous structural change of protein (Figure 2). First, retinal is excited from all-*trans* to 13-*cis*, 15-*anti* (transition of ground state (G state) to J or K-intermediate) and then protonated Schiff base (pSB) releases its proton and transfer to the proton acceptor, Asp85 (formation of M-intermediate, where retinal takes 13-*cis*, 15-*anti* conformation, deprotonated), the counterion of retinal Schiff base,[39] which forms pentagon cluster with Asp212, Arg82 and three water molecules (defined as Wat401, Wat402 and Wat406 in crystal structure shown by Luecke et al. (PDB code: 1C3W) where Asp85, Schiff base, Asp212 and Arg82 interact with Wat401 and Wat402, Wat402, Wat402 and Wat406, and Wat406, respectively[21]). Protonation of counterion is followed by breakage of hydrogen bonding interactions in this pentagon cluster and leads Arg82 to face to the side of proton release group (PRG), Glu194 and Glu204. Before passing proton to proton release group via hydrogen bonding water molecules, proton release to extracellular side from proton release group (transition from M_1- to M_2-intermediate) by opening proton diode gate of Ser193.[30] Proton transfer occurs by the stepwise changes in the sidechain pK_a values of ionizable residues, such as Asp85, Asp96, Glu194 and Glu204, caused by the changes in the packing of the helices, which results in H^+ ion flux to the extracellular side of the protein.[40] Then, proton at Asp96 is transferred to retinal to reprotonate Schiff base (formation of N-intermediate with 13-*cis*, 15-*anti* conformation, protonated). Reprotonation of Asp96 from cytoplasmic side occurs (transition from N- to O-intermediate, where retinal takes 13-*trans*, 15-*anti* conformation at O-intermediate). In order to transport vertically, change of accessibility from extracellular to cytoplasmic side is needed for Schiff base before Asp96 is reprotonated from cytoplasmic then retinal reisomerizes thermally and to switch back the accessibility of SB to extracellular side.[39]

Crystal structure of ground state revealed the hydrogen bonding network inside the protein which connects the key residues and water molecules to transport proton by proton hopping.[21] At the

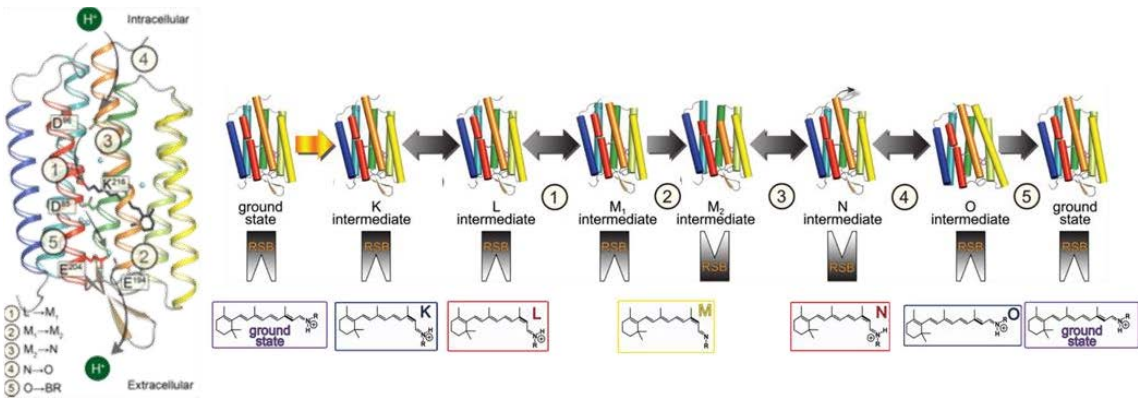

Figure 2. Proton transfer in BR and structural change at each intermediate.
Adapted and modified from [109].

state. Asp85 forms hydrogen bond with Thr89 with rest of the oxygen at Cδ and two oxygen at the side chain of Asp212 interacts with phenolic OH of Tyr57 and Tyr185 as well as the W406, where W406 connects to the positively charged Arg82. Disruption of these interactions by retinal isomerization decreases the stability of active site and induces the structural change over the protein. The hydrogen bonds between Arg82 and water molecules are connected to the extracellular side of BR by forming hydrogen bonds with other water molecules, such as Wat403, Wat404 and Wat405, to the proton release group of Glu194 and Glu204. In dark state and those of early intermediates (K, L and M_1), Schiff base is likely to be accessible to the extracellular side.[41]

Displacement of Wat402 occurs in K-intermediate.[38] In the initial state, Schiff base N-H bond vector points in the extracellular direction.[21] This is rotated at K-intermediate to weaken the Schiff base-counterion interaction as well as the twist around each bond in retinal polyene chain about < 20° compared to the planar 13-*cis*, 15-*anti* configuration.[42,43] The hydrogen bond between Schiff base and Wat402 is maintained as in ground state; however, the Nζ-H···O angle changed from linear 170-176° in ground state to 113° in K-intermediate.[42] Strong hydrogen bond held between Asp85 and Thr89 in K persists through M, contrary to the structural models based on x-ray crystallography of the photo-intermediates.[44] In the K state, retinal is the only displaced structure in the protein.[45]

L-intermediate is the stage for transition to M state where proton transfer from Schiff base to Asp85 occurs which implies a strong interaction between them at L state. Strong interaction between Schiff base and the counterion and particular double bond strain, C=N, in L-intermediate was observed by NMR.[46] Including FTIR studies, a water molecule bound to both Schiff base and the counterion at ground state, Wat402 as previously described, established stronger hydrogen bonds to both of them in L state.[47–51] Wat402 is then dragged to a space that is originally occupied by Leu93 according to the crystallography of L-intermediate[52,53] although an electron diffraction study of the L-intermediate showed no lateral displacements large enough to be seen at a resolution of 0.35 nm compared to the ground state.[54] Diffraction data from a crystal containing the M intermediate showed that this water molecule moves further towards the intracellular side in the L-to-M transition.[52,53] Additional small local perturbations lead to a decrease in the pK_a of Schiff base[55,56] and an increase of pK_a of Asp85[57,58] detected by FTIR which allows the proton transfer in the L-to-M transition. Changes near Asp85 were suggested to transmit the hydrogen bonds in the cytoplasmic channel involving Thr46, C=O of Val49, Asp96 and water molecules.[49,50] Indeed in L state crystal, approach of the phenyl ring of Phe42 to the carboxyl O of Asp96, and movement of the closest atom of the ring of Phe219 away from carboxyl OH of Asp96 was revealed compared to the ground state which explains the later change of deprotonation of Asp96 at M-to-N-intermediate because of the changed dipole environment of this protonated aspartic acid.[59] Mutation at retinal-binding site effects the kinetics of photocyclic process. Interaction of Trp182 indole ring with retinal C19 decreases the proton affinity of the Schiff base, thus, alteration of Trp182 to Phe slows L-decay and M-formation.[51,60,61]

M-intermediate in BR is one of the state which cannot be denied in a proton pump process as the proton is released from the retinal Schiff base to counterion, Asp85, to form 13-*cis*, 15-*anti* retinal with deprotonated state. Asp85 will be protonated when the pK_a of the proton release site is decreased later at N-intermediate. M-intermediate is characteristic in a sense that several substrates for M-intermediates were reported, such as M_1, M_2 and M_2'. H^+ is simultaneously released from a PRG in the extracellular side in the transition of M_1 and M_2. H^+ is then transported from Asp96 to Schiff base, which causes reprotonation of the SB in the process of transition from the M_2- to N-intermediate. In M_1, Wat402 moves nearly 1 Å away from the deprotonated retinal Schiff base nitrogen and breaks the hydrogen bond that bridges them, and initiates rearrangements of the hydrogen-bonded network of the extracellular region that develop fully in the intermediates that follow.[45] The breakage of hydrogen bonding interaction between the water and Asp85 enables Asp85 to move closer to the position originally occupied by the Schiff base.[62] Although both Asp85 and Asp212 can be proton acceptor, only Asp85 is protonated because of its flexible interaction with Wat401 and Thr89 which are both hydrogen-bonded to Asp85. On the other hand, Asp212 is hydrogen-bonded to Tyr57 and Tyr185, bulky residues that do not move during the photocycle and its pK_a is retained low.[40] In the M_1 to M_2 transition, relaxation of the C14–C15 and C15=N torsion angles to near 180° reorients the retinylidene nitrogen atom from the extracellular to the cytoplasmic direction, Wat402 becomes undetectable, and the side-chain of Arg82 is displaced strongly toward Glu194 and Glu204 (Figure 3).[45] In the M_2 states, the side-chain of Arg82 is displaced from its original position where it is hydrogen-bonded to Wat406, and thus to Wat401 and Asp85, toward the extracellular

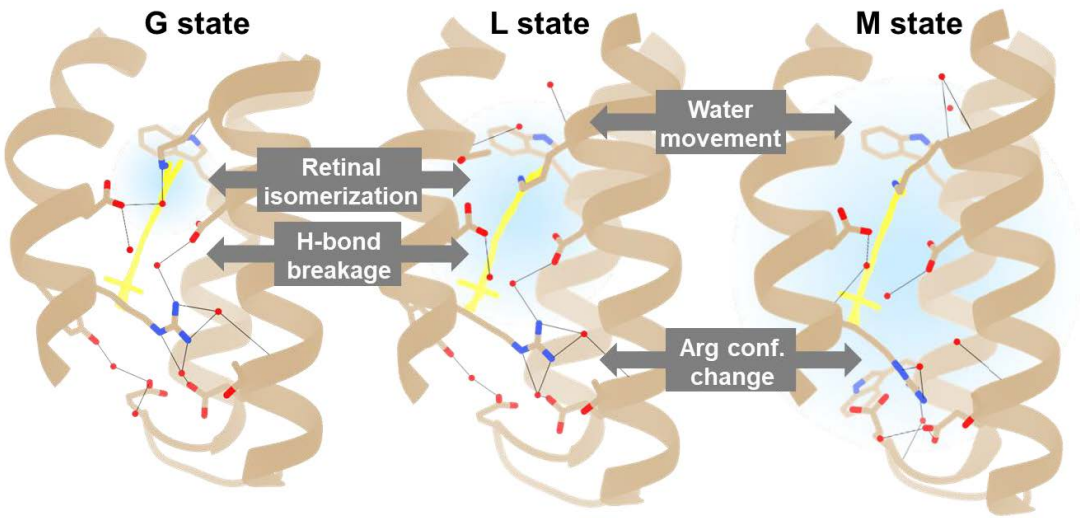

Figure 3. Disruption of hydrogen bonding networks in retinal-binding site at G, L and M states in Bacteriorhodopsin.
Hydrogen bond network changes were illustrated based on [63].

surface which explains that protonation of Asp85 is coupled to the release of a proton to the extracellular surface.[64–66] In the M_2 to M_2' transition, correlated with release of a proton to the extracellular surface, the retinal assumes a virtually fully relaxed bent shape, and the retinal C20 thrusts against the indole ring of Trp182 which tilts in the cytoplasmic direction.[45] Crystal structure of M2' or MN revealed the large displacement of retinal retinylidene nitrogen into a highly hydrophobic region by isomerization of the retinal causing the decrease in the pK_a of the Schiff base.[67] Solid-state NMR studies of bacteriorhodopsin, isotope-labelled in the protein and the retinal, revealed at least two different M states, an early and a late one which corresponds to the M_1 and M_2.[68] The H–C14–C15–H dihedral angle was more distorted than in the ground state, but to the same extent in the two M states of M_1 and M_2.[69]

At N-intermediate, deprotonated Asp96 created by the reprotonation of retinal Schiff base uptakes proton from cytoplasmic site. During formation of the L intermediate it is subjected to a change in the H-bonding character of Asp96 carboxylic group, but deprotonation occurs later at this reaction step.[70,71] Retinal takes 13-*cis*, 15-*anti* conformation during N-intermediate. Electron diffraction difference map revealed the F and G helices movement in the M- to N-intermediate transition when observed with F219L mutant which has longer life-time of N-intermediate at neutral pH instead of WT forming N-intermediate-like structure at high pH.[72] It was suggested that this originates from the Tyr185-Pro186 bond because of the importance of Pro186 to the photocycle[73,74] and Tyr185 to the hydrogen bond with Asp212 which undergoes significant changes during the photocycle[75,76]. Later Schobert et al. showed crystallographic structure of N-intermediate with V49A and F219L mutants[77] where carbonyl oxygen of Val49 is proposed to be the acceptor in H-bonding with the protonated Schiff base in the N intermediate[78]. The movements of F and G helices were seen as well with EPR measurements during M-to-N transition as well as the structural change of E-F loop to facilitate the release of a proton from Asp96 and the formation of a proton-conduction pathway from Asp96 to the Schiff base.[79] Re-isomerization of retinal induces conformational changes within the protein, such as tilt in helix E and F.[24,67] Outward tilt of helix F on the cytoplasmic side[26,41,80–82], followed by outward tilt of helix E on the extracellular side[83] linked to the protonation of the Schiff base by Asp96, reprotonation of Asp96, reisomerization of the retinal to all-*trans*, and the recovery of the initial state of the proton acceptor Asp85.[45] The proton donor to the SB, Asp96, locates at a distance of 10 Å from the Schiff base and about 6 Å from the cytoplasmic surface.[40] A cavity near Asp96 is capable of holding one or two water molecules[39], thus, forms the cluster possibly[40]. This appears to be caused by the deprotonation of Schiff base as well as the mobility of Lys216 side chain resulting in repacking of side chains between helices F and G and increasing cavity size.[40]

In the process of transition from the N- to O-intermediate, a H^+ is transported from the cytoplasmic side to Asp96, which causes uptake from the cytoplasmic side to BR as well as the retinal conformation change from 13-*cis*, 15-*anti* to all-*trans*, 15-*anti*.[40,84] Steric interaction between Trp182

and retinal C20 is known to control the transition from N- to O-intermediate, probably affects to the retinal conformational change at this step.[51]

Crystallographic structure of O-intermediate was not yet revealed with WT and instead L93A mutant was used to show the O-like structure as it delays the relaxation of O-intermediate.[85–87] The O-intermediate structure observed in L93A mutant showed similarity to the M-intermediate in WT-BR. The disappearance of the Wat402 (numbering based on the crystallographic structure (PDB code: 1C3W)[88]) that interacts with the Schiff base in the dark state. Deformation of the extracellular half of helix C, from Arg82 to Phe88, was also similarly observed as well as a profound swing in the side chain of Phe88. The paired structure of Glu194 and Glu204 is broken in O-intermediate by the flipping of Arg82 toward the extracellular side and formation of salt bridges with Glu194 and Glu204. Sliding movement of the extracellular half of helix G toward the extracellular side, which is associated with a large deformation of the FG loop. On the contrary, the major differences observed between O in L93A mutant and M in WT are the less-distorted main-chain conformation of Lys216, and sliding of the cytoplasmic half of helix G toward the extracellular side and the deformation of helix F around Arg175. The difference in the Lys216 is attributed in the configuration of retinal since the retinal in O-intermediate in L93A takes 13-*cis*/15-*syn* configuration, while the retinal in M state in WT takes 13-*cis*/15-*anti* configuration.

As the studies above shows, pumping mechanism and structures supporting the mechanism of bacteriorhodopsin are well-known. This makes BR the basic model of present studies on rhodopsins. However, even well-studied bacteriorhodopsin is not perfectly understood to show the clear relationship of structure and mechanism and create a new artificial rhodopsin with a new function.

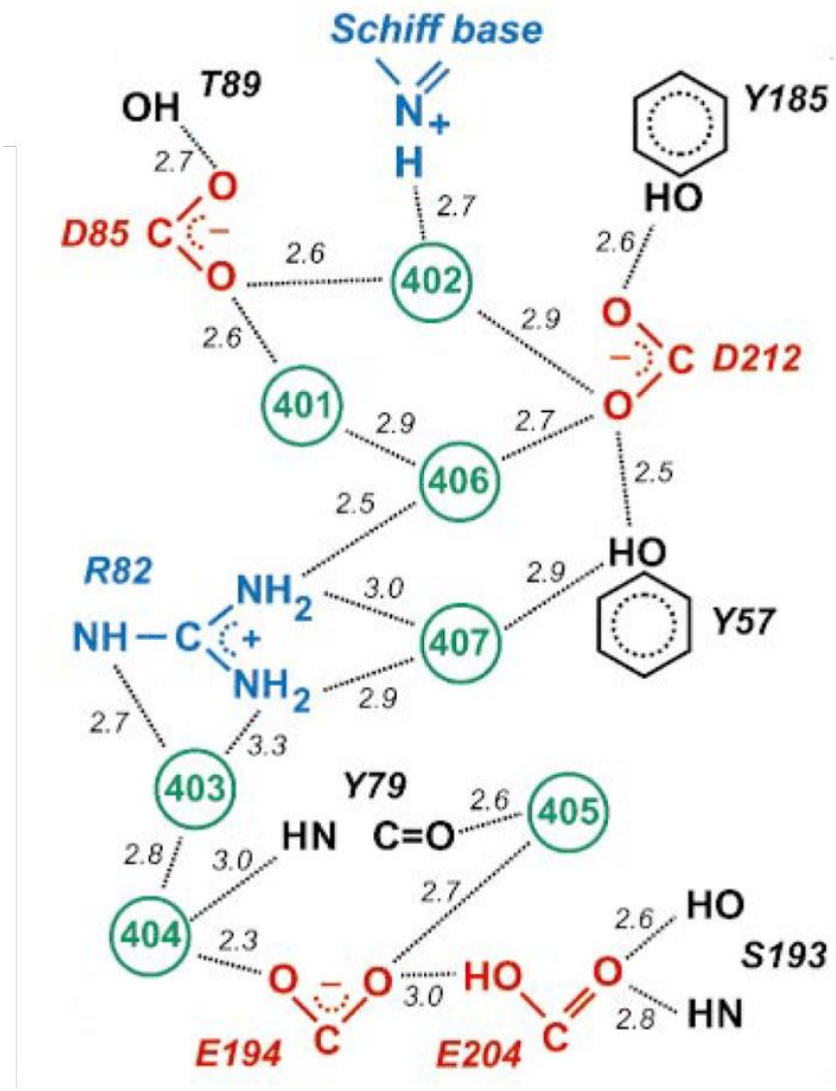

Figure 4. Hydrogen bond network from retinal Schiff base to the extracellular surface of Bacteriorhodopsin.
Positively and negatively charged residues are shown in blue and red, respectively. Green circles represent water molecules with the number definition. Dotted lines represent hydrogen bonds and N-O or O-O distances. Adapted from [21].

Studies on retinal-binding pocket of rhodopsins

As the expression of function is triggered by the light absorption which is followed by the retinal reisomerization from all-*trans* to 13-*cis*, structure of and around retinal has been targeted for better understandings of pump mechanism.

Retinal conformation varies among rhodopsins at ground state. Bacteriorhodopsin has two conformations of all-*trans* and 13-*cis* with the ratio of 1:1 as revealed by various methods such as high performance liquid chromatography (HPLC), which indicates that both conformations are at similar energy level in the retinal-binding pocket of bacteriorhodopsin. However, in the most rhodopsin, all-*trans* conformation is major at ground state which ratio is up to 70~90%.[89–91] Some rhodopsins have unique retinal conformation, for example, middle rhodopsin (MR) from *Haloquadratum walsbyi* is known to have three conformations of all-*trans*, 13-*cis*, and 11-*cis* at ground state.[92,93] As the common photocyclic process of rhodopsin starts from all-*trans* conformation which is followed by the reisomerization to 13-*cis*, the existence of 13-*cis* and/or 11-*cis* conformation raises the question of relation of photocyclic process starting from each conformation with that from all-*trans*. In the case of bacteriorhodopsin, the 13-*cis* retinal changes to all-*trans* retinal directly by light absorption and another photon absorption excites the retinal to form K-intermediate. Nevertheless, the direct pathway of conformation change from 13-*cis*, 15-*syn* to all-*trans*, 15-*anti* in bacteriorhodopsin needs to be cleared as some report indicate the existence of 13-*cis* photocycle in addition to all-*trans* photocycle.[94,95]

Residues around retinal are essential for pump rhodopsins and their sequence are conserved among the rhodopsins with same functions. As is written above, Asp85 and Asp96 are crucial for proton pump in bacteriorhodopsin and together with Thr89, these three residues are called DTD motif which is conserved among archaeal proton pumping rhodopsins,[96] such as Archaerhodopsin 1 (AR1)[97], Archaerhodopsin 2 (AR2)[97–99], and *Haloquadratum walsbyi* bacteriorhodopsin (*Hw*BR).[11,91] Proton pumps in bacteria, such as Thermophilic rhodopsin[11,100,101], Proteorhodopsin (PR)[102–104], and *Gloeobacter* rhodopsin (GR)[105,106] share DTE or DTX motif, where sodium ion pump[12,107,108] share NDQ motif (Figure 5). These residual differences among function-varying rhodopsins are essential for function, however, surrounding residues around retinal are influenced by the retinal isomerization which causes rearrangements of interactions throughout the protein.[63] The distortion in polyene chain and/or β-ionone ring induced by the steric hindrance from surrounding residues and interaction between retinal Schiff base and counterion or ion location in or around retinal exhibit the color tuning.[109] Mutation at surrounding residues successfully changed color in the wavelength range of 425 to 644 nm.[110,111] Recently the machine learning was used to understand the tendency of effective residues in microbial rhodopsins.[112] This gives the information about further functional role of residues surrounding retinal and possibilities of color tuning for optogenetic application. Therefore, residual tendency on function and the structural changes from ground state to excited states may reveal the

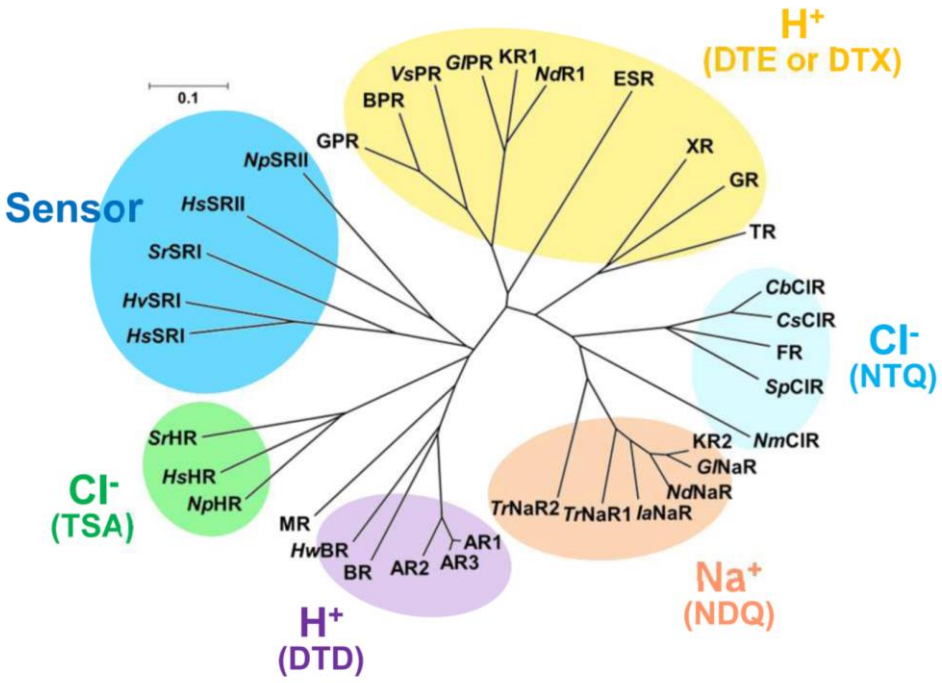

Figure 5. Phylogenic tree of rhodopsins.
Three letter represents the conserved residues among similar function at the location of Asp85, Thr89 and Asp96 in BR. Adopted from [96]

---

detailed mechanism of rhodopsin.

Functional conversion among rhodopsins

Functional conversions between rhodopsins give the information of how the functions of rhodopsins are separated. Functional conversions between H^+ pump, Cl^- pump and Na^+ pump were successful only in the directions of $Na^+ \rightarrow Cl^-$ pump, $Cl^- \rightarrow H^+$ pump and $Na^+ \rightarrow H^+$ pump using *Gleoeobacter* rhodopsin as a H^+ pump, *Fulvimarina pelagi* rhodopsin (FR) as a Cl^- pump and KR2 as a Na^+ pump.[113] Each rhodopsin has three residues at helix C conserved among genetically close rhodopsins with the same function which are DTD or DTE for H^+ pump (Asp121, Thr125 and Glu132 in GR), NTQ for Cl^- pump (Asn110, Thr114 and Gln121 in FR) and NDQ for Na^+ pump (Asn112, Asp116 and Gln123 in KR2) which corresponds to the positions of Asp85, Thr89, and Asp96 in BR. These conserved three residues are known to be essential for the function, thus, alteration of these residues may give the expected function. Indeed, correspondence in three residues and additional one mutation allowed the functional conversion as followings. The double mutation (NTQ/D102N) in KR2 was sufficient for converting Na^+ pump into a Cl^- pump. Triple mutant of DTE/S255F in FR and quadruple mutants of DTE/D102N and DTD/D102N in KR2 expressed H^+ pump. The asymmetric

results of functional conversions among the light-driven retinal-binding pumps relates to the course of evolution where the mutagenesis was successful when it reverse the course of evolution, but not when it follows the evolutionary direction. Another functional conversion showed the successful conversion of H^+ pumping AR3 to an H^+ channel by replacing three residues around the retinal chromophore (M128A/G132V/A225T mutant).[114] The modifications of two residues in the upper and lower sides of the β-ionone ring, M128A and G132V, respectively, and one around the Schiff base, A225T, lead to an increase in hydrophilicity of the ion transport pathway. Other studies on the functional conversions reported the conversion from a H^+ to a Cl^- pump,[115] from cation to anion channels[116,117] and from pump to sensor,[118] which were all achieved by the alteration of 1−3 amino acid(s). For this reason, the structural and functional information is essential for the further understandings of the rhodopsin protein as well as the optogenetics tool. Precise understandings on the relationship between structure and functionality are based on the inter-residual and inter-molecular interactions which controls the protein structural change during the photocyclic process and the efficiency of ion transportation.

Rhodopsins as an optogenetics tool

Studies on rhodopsins can be applied to optogenetics. Optogenetics is a powerful tool to control the behavior of cells using light. The light-sensitivity and the ion translocation ability of rhodopsins enabled to gain new insights into the brain in both health and disease. First report of rhodopsin application was the reliable and precise activation of neurons expressing the light-sensitive microbial rhodopsin, channelrhodopsin 2 (ChR2) from eukaryotic green alga *Chlamydomonas reinhardtii* by Deisseroth lab in 2005.[119] ChRs are the protein which transport ions in accordance with the concentration gradient, unlike the pumps like BR, HR and KR2, which transport ions against the gradient. A cation selective channel expressed in cells produce a high Na^+ conductance upon photo-irradiation and depolarize the cell membrane. ChRs have now been used to control neuronal activity in a wide range of animals, resulting in insights into fundamental aspects of circuit function as well as dysfunction and treatment in pathological states.[120,121] ChR2 expressed in neuron cells in mice and muscle cells in *C. elegans* successfully controlled the activation of motor cortex of mice and the forward and backward locomotion of *C. elegans*.[119,122–125] Activation control was now tested in nerve cells of mouse[126], rat[127], zebrafish[128] and monkey[129] as well.

As WT ChR2 has low ion transportation, thus, requires strong light-irradiation, and short absorption wavelength which is poisonous for the cells. ChR variants have been engineered with faster or extended open-state lifetimes[130–134] shifted absorption spectra[131,132,135], reduced desensitization,[123,135–137] and increased expression and photocurrent magnitude[123,130,131,134,136]. The highly effective variants of ChR was expressed in the neurons and used for the neural network analysis related to health and disease.[138–141] Nureki's group has revealed the structure of Channelrhodopsin where a C1C2 chimaera between ChR1[8] and ChR2 from *C. reinhardtii* was used to obtain the increased

resolution of 2.3 Å[142] from the former electron microscopy structure with rough helical arrangement of ChR2[143]. Variants of ChR has been constructed to the precise and selective control of the protein function, such as absorption wavelength, cation conductivity, photo-sensitivity, photocucrrents, cation selectivity and kinetics. The revealed structural information assists in the design of mutants with highly effective function as well as the interpretation of functional analyses of each variants.

In contrast to the neural excitation by cation influx created by ChR2, neural silencing was successfully induced using a Cl^- pumping rhodopsin HR from the archaeon *Natronomonas pharaonis* (*Np*HR)[144] and an H^+ pumping rhodopsin Archaerhodopsin 3 (AR3) from archaeon *Halorubrum sodomense*[145]. AR3 enabled color-tuning with mutations in retinal-binding pocket allowing the locomotion paralysis of *C. elegans* cells upon blue light illumination. As an optogenetics tool, new functions or characteristic features expands the possibility of application.

NMR studies on rhodopsins

Reconstitution of membrane proteins

Membrane proteins are structurally stable in lipid membrane. Original structure of these proteins as in the organisms can be reproduced in the lipid membrane with similar lipid composition and, therefore, mimic membrane is used for the NMR detection. There are various types of lipid membranes: micelle, bicelle, liposome, lipodisq, nanodisc etc. Liposome is often used for solid-state NMR analysis of membrane proteins. This is a closed bilayers which is formed when lipids are in water. The name of liposomes varies after its size: small unilamellar vesicle (SUV), large unilamellar vesicle (LUV), large multilamellar vesicle (MLV) and giant unilamellar vesicle (GUV) which are about ~20 nm, ~100 nm, 1000 nm and 10 μm in diameter.[146,147] For NMR sample, MLV is often used.

Whole structural determination of rhodopsins

Crystallography has been an informative way of showing detailed structures of rhodopsins, however, whole structural determination by solid-state NMR has been successful in *Anabaena* sensory rhodopsin (ASR).[148–150] Uniformly ^{13}C, ^{15}N-labeled ASR sample reconstituted in lipids was grown on glycerols labeled at positions 1, 3 or 2, which allowed us to obtain nearly complete backbone and side-chain ^{13}C and ^{15}N chemical shift assignments of ASR. 2D ^{13}C-^{13}C correlation experiment with DARR[151–153], 3D NCOCX[154–156], CANCO[157] and NCACX[156] experiment with DARR mixing time of 100 ms were applied for signal assignment. Correlation peaks obtained by these methods allows to assign the residues from the sequence and inter-helically close located residues. Obtained structure of ASR differed from that in the crystalline environment, especially on B–C loop, helix G, and single conformation of retinal, indicating that the retinal is in all-*trans* conformation in the dark state. Single

conformation of retinal corresponds to the earlier results.[158]

Structural determination for the loops of bacteriorhodopsin by Higman et al. revealed distinct structure at AB loop in comparison with crystallographic data.[159] One of the residue from assigned four out of seven residues at AB loop, Ser35, showed β-sheet structure based on the multi-dimensional NMR measurements of 2D DARR and 3D NCACX, 3D NCOCX, 3D CANCO and 4D CAN(CO)CX[160] and TALOS+ predictions[161] although the crystal structure favored the helical structure.

Trapping of photo-intermediates

In order to clarify the mechanism of photo-activated protein, structural changes during photocycle needs to be revealed. Solid-state NMR has low time resolution, therefore, methods to trap photo-intermediates are essential to obtain the structural information. Herzfeld's group was the first that reported the structure of cryo-trapped photo-intermediates of bacteriorhodopsin.[46,68] Their studies focus on the retinal conformation and Schiff base protonation and deprotonation. They targeted L-, early and late M-, and N-intermediates. Samples were illuminated at low temperature directly in the probe and magnet via a glass optic fiber bundle. The selection of light frequencies is needed for the preparation of different photo-intermediates which was achieved by inserting glass filters between the fiber and the light source. A water filter was used to eliminate the heat caused by near-IR components. Light-adapted bacteriorhodopsin was accumulated at 0°C by illuminating for several hours with white light. L-, M_0-, M_n-, and N-intermediate were trapped by illuminating light with λ>610 nm for L-intermediate and 540 nm for rest three intermediates at -95 to -130 °C, -60 °C, -10 °C, and around -20 °C, respectively. M_0-intermediate was thermally relaxed to M_n and/or N-intermediates at –29 °C and to light-adapted state at 0 °C for about 1 h and M_n and/or N-intermediates to light-adapted state at 0 °C for about 1 h. Observation of [12,14-^{13}C]ret, [ε-^{13}C, ζ-^{15}N]Lys signals revealed the photo-cyclic pathway of LA→M_0→(M_n+N)→LA and retinal conformation of 13-*cis*, 15-*anti* at each intermediates.

The trapped amount of photo-intermediates are limited, especially on the early intermediates with short life time. To track the photo-conversion from ground state, Griffin's group applied dynamic nuclear polarization (DNP) to observation of K-intermediate in bacteriorhodopsin.[162,163] DNP has been demonstrated to provide large signal enhancements in bacteriorhodopsin in magnetic fields of 5 T[164] as the greater polarization of electron spins is transferred to the nuclear spins before the NMR experiment.[165,166] The DNP-enhanced solid-state NMR spectroscopy at cryogenic temperatures has provided the first NMR observation of the K-intermediate and relaxation to several L-intermediates of bacteriorhodopsin. The ^{15}N chemical shifts of retinal Schiff base in theses photo-intermediates indicate that the Schiff base loses contact with its counterion in K and establishes a new counterion interaction in L.[162] 2D ^{15}N-^{13}C correlation spectra obtained under DNP additionally revealed four substrates of L-intermediate with one functional and three shunts.[163]

DNP-enhanced observations of photo-intermediates were reported by Glaubitz's group and Oschkinat's group on other rhodopsins. Glaubitz's group has been reported the photo-chemical reaction in green proteorhodopsin (GPR) to show the cryo-trapped K- and M-intermediates. The K-state was trapped by direct illumination by light transferred via a glass fiber within the DNP probe at 100 K for 40 min. After illumination, the sample was directly measured without further illumination. The M-state was trapped by illuminating PR-E108Q mutant outside of the DNP probe for 1.5 min using a 525 nm LED at room temperature and then flash-frozen in liquid nitrogen within the precooled rotor catcher and transferred into the DNP probe precooled at 100 K. A high M-state population could be achieved by preventing reprotonation of the Schiff base through a mutation of the primary proton donor (E108Q). The retinal was labeled at the position of C10-C15 to obtain the detailed conformational change.[167] ^{13}C–^{13}C proton-driven spin diffusion (PDSD) correlation spectra and double quantum−single quantum (DQ-SQ) correlation experiments allowed chemical shift assignments of each labeled nuclei. Obtained chemical shifts of C14 and C15 allows to calculate the dihedral angle at each intermediate by converting the chemical shift to HCCH dephasing curves.[168] Glaubitz's group was also successful in trapping photo-intermediates of ChR2 using DNP-enhanced photo-irradiation system with transparent sapphire sample tube.[169] Oschkinat's group was also successful to trap photo-intermediate of ChR2 with DNP and revealed the retinal conformation at P_{500} and P_{390}.[170]

NMR methods

Basis of nuclear magnetic resonance

The NMR phenomenon

The magnetic resonance phenomenon occurs as a result of the quantum mechanical property of spin.[171] The spin angular momentum confers a magnetic moment on a nucleus and a given energy in a magnetic field. The nuclear spin (I) takes I = 0, 1/2, 1, 1(1/2), etc. depending on the nuclear mass number and the atomic number where I=0 when both of them are even, I = n/2 (n = 1, 3, 5, ...) when former is odd, I = n (n = 1, 2, 3, …) when former is even and latter is odd. Frequently used ^{1}H, ^{13}C and ^{15}N are I = 1/2, however, ^{2}H, ^{12}C and ^{14}N are I = 1, 0, 1, respectively. The nuclear magnetic moment, μ, is given by the following equation.

$$\mu = \gamma I \hbar$$

The gyromagnetic ratio, γ, is the proportionality constant which determines the resonant frequency of the nucleus for a given external field. A nucleus of spin I has $2I + 1$ possible orientations in a magnetic field, which is given by the value of magnetic quantum number m_I, taking the values of $-I$, $-I + 1$, …$I - 1$, I. When spin-1/2 nucleus is placed in a static field, two orientations of the small magnet

corresponds to the m_I (± 1/2) which are parallel and antiparallel against the external magnetic field. The transition between energy levels like these by radiofrequency radiation consequences the NMR absorption.

In the presence of an applied magnetic field $\mathbf{B}_0$, the magnetic moment experiences a torque which is the vector product of the nuclear angular momentum **J** and the magnetic moment μ. This torque equals the rate of change of the angular momentum.

$$\frac{d\mathbf{J}}{dt} = \boldsymbol{\mu} \times \mathbf{B}_0$$

$$J = I\hbar$$

Using the equation of $\boldsymbol{\mu} = \gamma \boldsymbol{I}\hbar = \gamma \mathbf{J}$,

$$\therefore \frac{d\mu}{dt} = \gamma \boldsymbol{\mu} \times \mathbf{B}_0$$

Spin takes two states of energy level, parallel and antiparallel to magnetic field (or mentioned later as up and down spins). The energy between two spins can be expressed as the following equation. The energy of the interaction is proportional to μ and $\mathbf{B}_0$.

$$E = -\gamma \hbar m_I B_0$$

The difference in energy between the two states of the nucleus is

$$\Delta E = \gamma \hbar \mathbf{B}_0$$

Magnetic moment process about the direction of the magnetic field can be described with an angular frequency as following:

$$\boldsymbol{\omega}_0 = \gamma \mathbf{B}_0 = 2\pi \mathbf{f}_0$$

$\mathbf{f}_0$ is called the Larmor Precession frequency. This is parallel to $\mathbf{B}_0$, but will be in the opposite direction if γ is positive.[172] The Larmor Precession frequency of radiation required to cause transitions between the two levels. This transition is called nuclear magnetic resonance (NMR). The splitting of energy level is called as Zeeman splitting. The two energy states of α and β will be unequally populated, the ratio being given by the Boltzmann equation.[171]

$$\frac{N_\beta}{N_\alpha} = e^{-\Delta E/k_B T}$$

Chemical shifts

Chemical shift (δ) is one of the basic parameters of NMR which is defined as follows.[171]

$$\delta = \frac{\omega - \omega_0}{\omega_0} \times 10^6$$

δ is always written in parts per million (ppm). ω_0 is the Larmor frequency in Hz and ω is the resonant frequency of the interest. This shift is caused by induced local magnetic field by change in electric charges of the electron cloud around a nucleus. Nucleus is shielded, hence, the effective field

at the nucleus is

$$\boldsymbol{B_{eff}} = \boldsymbol{B_0}(1-\sigma)$$

The level of shielding is given by the shielding constant, chemical shift tensor, σ. This is directly related to the electron density ρ at a distance *r* from the nucleus by Lamb's equation shown bottom.

$$\sigma = \frac{4\pi e^2}{3mc^2}\int_{-\infty}^{\infty} r\rho(r)\mathrm{dr}$$

The shift tensor σ is related to the Larmor frequency, ω_0 and to the chemical shift:

$$\omega_0 = \frac{\gamma}{2\pi}\boldsymbol{B_0}(1-\sigma)$$

$$\delta = 10^6(\sigma_{ref} - \sigma_{sample})$$

An anisotropic C-H bond shows the difference in local magnetic fields of the nuclei. These differences are reflected in the chemical shift tensor which has main three components of σ_{11}, σ_{22}, σ_{33} and the isotropic shift tensor σ_{iso} is given by:

$$\sigma_{iso} = \frac{1}{3}(\sigma_{11} + \sigma_{22} + \sigma_{33})$$

J coupling

There is an interaction between the nuclei themselves arising from an intdirect coupling through the electron spins called the spin-spin interaction, or the *J* interaction.[172] Considering two environments as A and X, energy of interaction with an external field is

$$V(m_A, m_X) = -\hbar\omega_A m_A - \hbar\omega_X m_X$$

$$\omega_A = \gamma_A B_0(1-\sigma_A)$$

$$\omega_X = \gamma_X B_0(1-\sigma_X)$$

where possible values are

$$m_A, m_X = \pm\frac{1}{2}$$

The modification in the energy causes a further splitting in the energy level system.

$$V(m_A, m_X) = -\hbar\omega_A m_A - \hbar\omega_X m_X + hJ_{AX} m_A m_X$$

Whether the last term is positive or negative depending on the values of m_A and m_X. ω is B_0 dependent; however, the *J* splitting is not and expressed in Hertz as *h* in the equation. The complication in spectrum can be simplified through decoupling shown below.

Radio-frequency (RF) radiation and the rotating frame

For NMR experiment, in addition to a magnetic moment **μ** processing about the direction of an external magnetic field $\mathbf{B}_0$ along the *z* axis with angular velocity ω, small, time-dependent, additional magnetic field $\mathbf{B}_1$ needs to be considered.[172] $\mathbf{B}_1$ is rotating in the x-y plane in the same sense

and with the same angular velocity as **μ**. In the rotation frame, $\mathbf{B}_1$ is taken to be along the *x'* axis.

Of two components rotating with opposite senses, only the component rotating in the same sense as **μ** has significant effect on it and the other can be disregarded. In the presence of both $\mathbf{B}_0$ and $\mathbf{B}_1$, μ obeys the equation

$$\frac{\mathrm{d}\boldsymbol{\lambda}}{dt} = \gamma\boldsymbol{\mu} \times (\mathbf{B}_0 + \mathbf{B}_1)$$

Transforming to a coordinate system rotating about the *z* axis with angular velocity in which $\mathbf{B}_1$ will stand still,

$$\frac{d\boldsymbol{\mu}}{dt} = \frac{d\boldsymbol{\mu}'}{dt} + \boldsymbol{\omega} \times \boldsymbol{\mu}'$$

$$\gamma\mu' \times (\mathbf{B}_0 + \mathbf{B}_1) = \frac{d\mu'}{dt} + \omega \times \mu'$$

$$\frac{d\mu'}{dt} = \omega'_0 \times \mu'$$

$$\boldsymbol{\omega}'_0 = -(\boldsymbol{\omega} + \gamma\mathbf{B}_0 + \gamma\mathbf{B}_1)$$

In the rotating frame, equation of motion of the dipole is

$$\frac{d\mu'}{dt} = \gamma\mu' \times \mathbf{B}_{\mathrm{eff}}$$

thus

$$\gamma\mathbf{B}_{\mathrm{eff}} = (\omega - \omega_0) + \gamma\mathbf{B}_1 = -\omega_{\mathrm{eff}}$$

μ' will be stationary in the rotating frame when $\omega = \omega_0$ and $B_1 = 0$. Rotating frame is used to simplify the calculations.

Relaxation

The obtained magnetization at *xy* plane after the exposure of RF pulse will return to the initial state by thermal equilibrium along the *z* axis.[171] Two main relaxations of longitudinal relaxation (T_1) and transverse relaxation (T_2) are described as followings.

$$\frac{\mathrm{dM}_z}{\mathrm{d}t} = \frac{\mathrm{M}_0 - \mathrm{M}_z}{T_1}$$

$$\frac{\mathrm{dM}_x}{\mathrm{d}t} = -\frac{\mathrm{M}_x}{T_2}$$

$$\frac{\mathrm{dM}_y}{\mathrm{d}t} = -\frac{\mathrm{M}_y}{T_2}$$

After a π/2 pulse, the magnetization precesses about the *z* axis in the *xy* plane and the *z* magnetization reappears with the time constant T_1. T_2 relaxation is given as followings: when the magnetization is in

the *xy* plane and the phase coherence between the spins in the transverse plane, and loss of this phase coherence due to mutual exchange of spin energies which gives rise to T_2 relaxation.

Decoupling

To simplify the analysis of NMR spectra, decoupling is used to suppress the interaction between nuclear spins, either the scalar interaction or the direct dipole-dipole interaction.[172] The effect of a scalar *J* coupling between two nuclei with different chemical shifts on the NMR spectrum is caused by the shift in the energy levels of nucleus *X* between the cases in which the coupling nucleus *A* has its spin up and down which results in the splitting of the line of nucleus *X* due to its *J* coupling with nucleus *A*. By inducing rapid transitions between the up and down states of nucleus *A*, two states of nucleus *A* are averaged and the splitting of the *X* line collapses. These decoupling transitions can be brought by the irradiation of radio frequency at the resonance frequency of the nuclear spin to the decoupled *X*. This technique can be applied to identify the nuclei coupled by the J interaction. Decoupling on a particular nuclear spin gives simplified nuclear spin while others represent multiplets.

For solid-state NMR, this technique can also be used to narrow the broad lines. Broad linewidth in solid samples is due to the dipole-dipole interaction of the ^{13}C nuclear spin with the abundant proton spins. Decoupling in the solid state differs experimentally in that the rf power in the decoupling radiation must be several orders of magnitude higher in order to stir the proton spins over the wide range of frequencies in the broad line proton NMR spectrum. The ^{13}C linewidth can be reduced by high power irradiation of the proton spectrum. The heteronuclear decoupling differs from homonuclear decoupling, for instance, linewidth of proton resonance is reduced by suppressing the dipole-dipole interactions among protons themselves.

Cross polarization-Magic Angle Spinning (CP-MAS)

Cross-polarization is a technique for increasing the sensitivity in the NMR of sparse nuclear spins by utilizing those spins' interactions with a collection of abundant spins such as protons.[172] Population difference between the spin up and down states for the sparse species is increased. In addition to that, time between successive free induction decays (FID) can be cut down by the effectively shortened relaxation time of the sparse nuclei.

The mechanism of cross polarization is as followings. In order to obtain narrow peak in solid-state NMR spectra, a trick of sparse spins is used.[171] For example, ^{13}C interact with another ^{13}C but in a distance that the term $\mathcal{H}_{SS}(\theta)$ can be neglected,

$$\mathcal{H}_{TOTAL} = \mathcal{H}_Z + \mathcal{H}_\delta + \mathcal{H}_{II(\theta)} + \mathcal{H}_{IS(J)} + \mathcal{H}_{TOTAL}$$

By applying high-power decoupling to the I spins, the total Hamiltonian can be simplified more.

$$\mathcal{H}_{TOTAL} = \mathcal{H}_Z + \mathcal{H}_\delta$$

Enhancement of sensitivity for the dilute spins can be achieved through a technique called cross-

polarization. This technique is achieved by polarization transfer from the abundant spins, such as ^{1}H, to the rare spins, for instance ^{13}C through matching the B_1 radio frequency fields of the nuclei. Hartmann-Hahn condition should be fulfilled in this technique known as follows:

$$\gamma_H B_{1H} = \gamma_C B_{1C}$$

where B_x is known as the radio frequency spin locking fields. γ_H is 26.75×10^7 [T^{-1} s^{-1}] and γ_C is 6.73×10^7 [T^{-1} s^{-1}],[173] hence,

$$B_{1H} = 4B_{1C}$$

which means the sensitivity of the ^{13}C spins are enhanced by the ^{1}H spins by a factor of 4.

Magic angle spinning (MAS) is a commonly used method to increase the resolution of solid-state NMR spectra.[171,174] Solid sample requires to average the chemical shift anisotropy and through-space dipolar couplings for sharp peak whereas in solution, it is averaged to zero by rapid isotropic motion. The angle satisfying the following equation is 54.7°, which is called magic angle, allows to average the narrowing facts of the peaks.

$$3\cos^2\theta - 1 = 0$$

The static line shape breaks into a group of sharp peaks under magic angle spinning, which peaks are spaced by the spinning frequency. With increase in MAS rate exceeding the magnitude of the anisotropic interactions, sharp signal appears at the center of the band with less number of side bands of the signal and no side decreases when the MAS frequency is large enough than the static linewidth. Value of the common anisotropic interactions are followings: ^{1}H-^{1}H dipolar coupling, 60 kHz (CH_3 group); ^{13}C-^{1}H dipolar coupling, 23 kHz (directly bonded CH pair); ^{15}N-^{1}H dipolar coupling, 11 kHz (directly bonded NH pair); ^{13}C-^{13}C dipolar coupling, 3 kHz (directly bonded CC pair); ^{13}C CSA, 100 ppm (carbonyl)/10-20 ppm (aliphatic); ^{15}N CSA, 100 ppm (amide N).

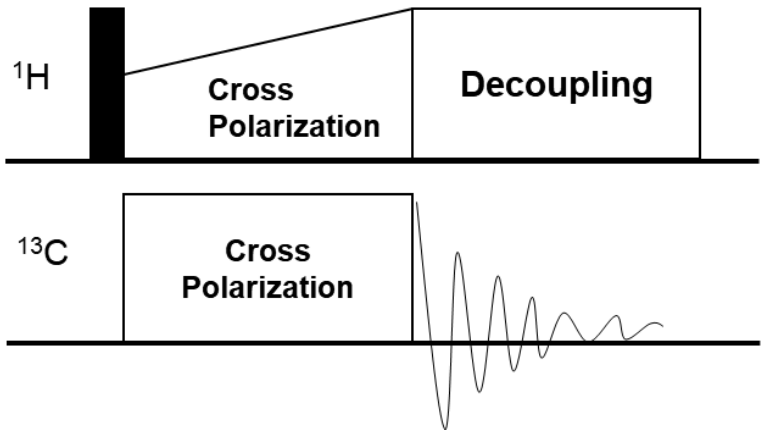

Figure 6. Pulse sequence of CP-MAS.

Proton-driven spin diffusion (PDSD) and dipolar-assisted rotational resonance (DAAR)

^{13}C-^{13}C Proton-driven spin diffusion[175,176] and dipolar-assisted rotational resonance (DARR)[151–153] are two-dimensional NMR experiment. These methods allows a coherent polarization exchange between coupled ^{13}C spins in the presence of the dipolar couplings to the ^{1}H bath, which provides the energy necessary for the transfer. Longer mixing time enable the detection of long-range contacts in the polypeptide chain (Table 1). The signal intensity of the cross-peaks contains the information about internuclear distances. PDSD and DARR methods are similar except that the rotary-resonance ^{1}H irradiation during mixing time to enhance the through-space spin diffusion.

The theory of DARR method can be described as followings.[152] The system of DARR can be considered to be composed of two dipolar-coupled ^{13}C spins (S_1 and S_2) and one ^{1}H spin (I). The homogeneous broadening originated from the other ^{1}H spins increases the efficiency of the ^{13}C-^{13}C polarization transfer. But the other ^{1}H spins are not explicitly treated as they are not directly related to the ^{13}C-^{13}C recoupling mechanism. The chemical shift anisotropy interaction was neglected and the rf field with the intensity ν_1 is applied to I spin on resonance. The ^{13}C-^{1}H interaction for the second S spin (S_2) is supposed to be negligible. In the double rotating frame, the total spin Hamiltonian consists of the Zeeman interaction $\mathcal{H}_Z$, the ^{13}C-^{13}C dipolar interaction $\mathcal{H}_D^{SS}(t)$, and the ^{13}C-^{1}H dipolar interaction $\mathcal{H}_D^{IS}(t)$ as

$$\mathcal{H} = \mathcal{H}_Z + \mathcal{H}_D^{SS}(t) + \mathcal{H}_D^{IS}(t)$$

with

$$\mathcal{H}_Z = \Delta_1 S_{Z1} + \Delta_2 S_{Z2} + \nu_1 I_x$$

$$\mathcal{H}_D^{SS}(t) = d(t)\left\{S_{1Z}S_{2Z} - \frac{1}{4}(S_{1+}S_{2-} + S_{1-}S_{2+})\right\}$$

$$\mathcal{H}_D^{IS}(t) = D(t)S_{1Z}I_Z$$

where Δ_n is the resonance offset of the S_n spin, and

$$d(t) = d_0\{g_1(\alpha_d, \beta_d)\cos(2\pi\nu_R t + \gamma_d) + g_2(\alpha_d, \beta_d)\cos(4\pi\nu_R t + 2\gamma_d)\}$$

$$D(t) = D_0\{G_1(\alpha_D, \beta_D)\cos(2\pi\nu_R t + \gamma_D) + G_2(\alpha_D, \beta_D)\cos(4\pi\nu_R t + 2\gamma_D)\}$$

Here, d_0 and D_0 are the dipolar coupling constants for ^{13}C-^{13}C and ^{13}C-^{1}H, respectively, ν_R is an MAS frequency, and (α_d, β_d, γ_d) and (α_D, β_D, γ_D) are the Eular angles describing the orientation of the S_1-S_2 and the S_1-I internuclear vectors in the rotor-fixed frame, respectively.

The total Hamiltonian is transferred into the interaction frame defined by the unitary transformation shown below when the rotary-resonance condition is n = 1 among two conditions of two rotary-resonance conditions of $\nu_1 = n\nu_R$ (n = 1 or 2).

$$U = \exp(2\pi i \nu_1 I_X t)$$

This transformation affects to only the ^{13}C-^{1}H dipolar interaction, thus, zeroth-order average Hamiltonian is obtained as following:

$$\overline{\mathcal{H}_D^{IS}(t)} = \pm D_1 S_Z$$

with

$$D_1 = \frac{1}{4} D_0 G_1(\alpha_D, \beta_D) cos\gamma_D$$

by replacing I_z by ±1/2. D_1 represents the recovered ^{13}C-^{1}H dipolar coupling. The total Hamiltonian is further transformed by the unitary transformation

$$U = \exp[2\pi i\{(\Delta_1 \pm D_1)S_{1Z} + \Delta_2 S_{2Z}\}t]$$

Thus, the ^{13}C-^{13}C dipolar interaction $\mathcal{H}_D^{SS}(t)$ in this new frame is given by

$$\widetilde{\mathcal{H}_D^{SS}(t)} = d(t)\left[S_{1Z}S_{2Z} - \frac{1}{4}\{S_{1+}S_{2-}\exp(2\pi i\Delta t) + S_{1-}S_{2+}\exp(-2\pi i\Delta t)\}\right]$$

with

$$\Delta = \Delta_1 \pm D_1 - \Delta_2$$

^{1}H decoupling applied eliminates D_1, leading to the rotational resonance (R^2) recoupling condition of $\Delta_1 - \Delta_2 = m\nu_R$ $(m = \pm 1, \pm 2, \ldots)$ in the conventional rotational resonance whereas in the present case, the non-zero ^{13}C-^{1}H dipolar coupling modifies the conventional R^2 condition as

$$\Delta_1 \pm D_1 - \Delta_2 = m\nu_R$$

This corresponds to a situation that one of the spinning side bands of S_2 overlaps the ^{13}C-^{1}H dipolar powder pattern of S_1. This recoupling is referred as the dipolar-assisted rotational resonance recoupling. The pulse sequences of PDSD and DARR are shown in Figure 7 and Figure 8, respectively.

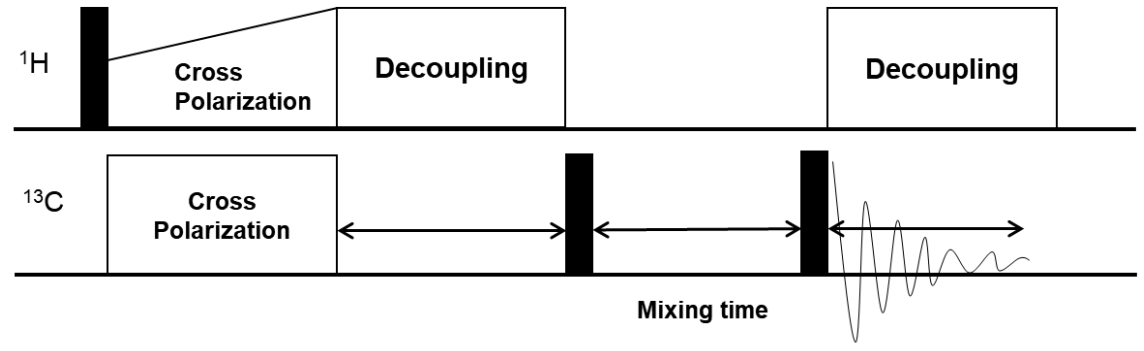

Figure 7. Pulse sequence of PDSD.

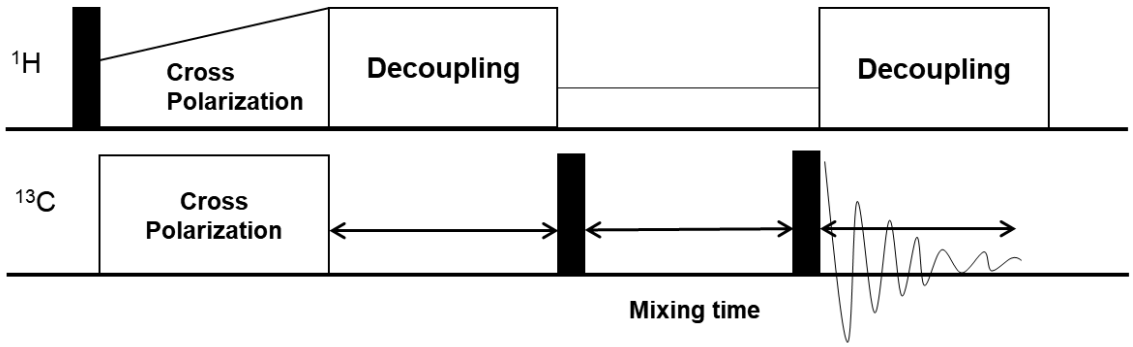

Figure 8. Pulse sequence of DARR.

Table 1. Correlation between length of mixing time and the observable ^{13}C-^{13}C distances (Å) [174]

Mixing time (ms)	Strong	Medium	Weak
50	3.3	4.5	5.6
100	4.5	5.1	6.3
200	4.8	5.7	7.0
300	5.3	6.1	7.5
400	5.5	6.4	7.9
500	5.8	6.7	8.2

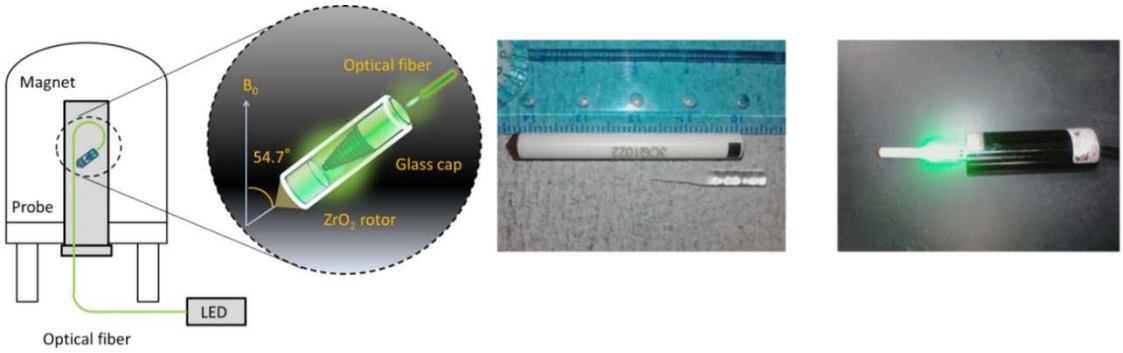

Figure 9. *In-situ* photo-irradiation solid-state NMR.
(Left) optical fiber connected to LED source is lead into probe and light goes directly into sample tube through glass cap. Adapted from [178]. (Middle) Sample tube and glass cap. (Right) Light irradiation through glass cap when no sample is inside the sample tube.

In-situ photo-irradiation solid-state NMR

In-situ photo-irradiating solid-state NMR is a way to trap intermediates by controlling on/off of LED light from outside of probe.[177–179] As shown in Figure 9, optical fiber connected to LED source is lead into probe and light goes directly into sample tube through glass cap. Since switch for LED is outside of the probe, light irradiation control can be done without taking sample tube which means measurements can be done continuously without changing conditions. Light wavelength is changeable among 520 nm, 595 nm and 365 nm by switching light source one to another.

Interactions at retinal-binding pocket in KR2

Introduction

Cation transportation into/out the cell

Ion transportation from inside and outside of cell to another is essential for biological activity since the concentration gradient i.e. electric potential at membrane are used for signaling transfer etc. Several membrane protein conduct the cation transportation, such as Na^+/K^+-ATPase, ion channel and ion pump. Among these membrane proteins, rhodopsin family conducts these functions by using light as an energy source. Ion transporting rhodopsins are classified roughly into H^+ pump, Cl^- pump, $Na^+/K^+/H^+$ channel. Recently a new group was added to the rhodopsin family called Na^+ pump and rhodopsins in this group are called NaR. So far 12 NaRs were found, namely, *Krokinobacter eikastus* 2 (KR2), *Dokdonia* sp. PRO95[107,180–183], NdNaR2 from *Nonlabens (Donghaeana) dokdonensis*[183,184], GLR from *Gillisia limnaea*[183,185], *Fd*NaR from *Flagellimonas* sp_DIK[186,187], NMR2 from *Nonlabens marinus*[188], *Ny*NaR from *Nonlabens* sp. YIK[186,187], *Ia*NaR from *Indibacter alkaliphilus*[108,180,183,189], *Desulhohustis* sp. PB-SRB1[187], *Tr*NaR from *Treupera radiovictrix*[183,187,190], *Micromonospora* sp. CNB 394-2, *Salinarimonas rosea* DSM21201 (*Sr*NaR), and *Lyngbya aestuarii*. These NaRs have conserved N-helix.

First-found sodium ion pump, Krokinobacter *rhodopsin 2*

First-found sodium ion-pumping rhodopsin *Krokinobacter* rhodopsin 2 is a microbial rhodopsin (type I)[191] extracted from marine flavobacterium *Krokinobacter eikastus*.[12,192] This bacterium possesses two rhodopsins, *Krokinobacter* rhodopsin 1 (KR1) and KR2, which pump protons and sodium ions, respectively, but the latter also pumps protons at low NaCl concentrations.[193] Although other sodium ion-pumping rhodopsins have been reported,[182,184,185,194] crystal structures have been determined for only KR2 (Figure 10).[183,195] Functions of rhodopsins are related to sequences that are proximal to retinal. Bacteriorhodopsin (BR)-like proton pumps have DTD motifs with Asp85, Thr89, and Asp96 residues.[196] Whereas Asp85 works as a counterion of the Schiff base, Asp96 takes a proton from the cytoplasmic side. The corresponding residues in sodium ion pumps are known as Asn, Asp, Gln (NDQ) motifs and comprise Asn112, Asp116, and Gln123 in KR2 (Figure 11).[196] In contrast with those in BR, Asp116 functions as a counterion and is located one helical pitch toward the cytoplasmic side.

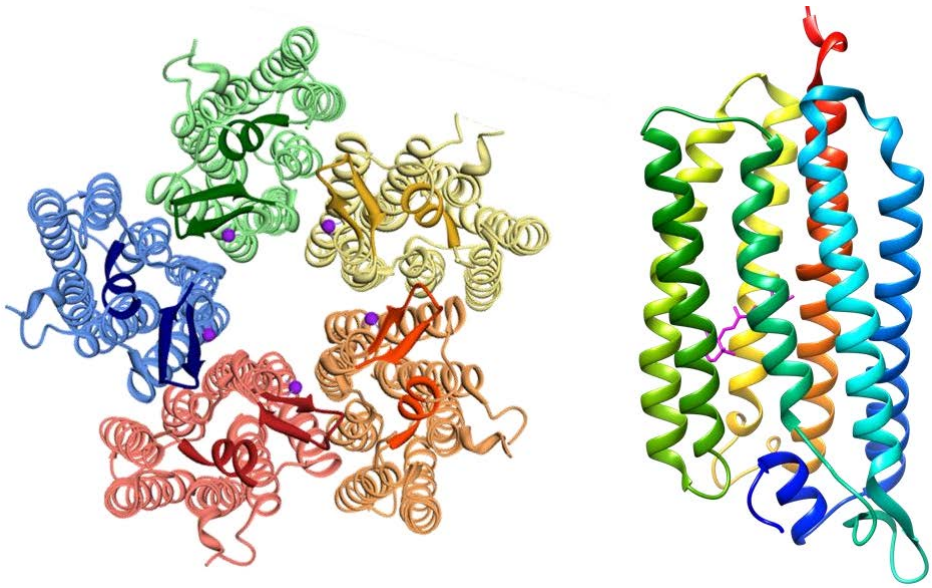

Figure 10. Crystallographic structure of KR2.
(Left) KR2 forming pentamer holding Na^+ between each protomer (PDB code: 4XTO). View from extracellular side. Purple sphere represents the bound Na^+. (Right) Structure of KR2 monomer (PDB code: 3X3C). Retinal is shown in pink in the middle of helix bundle.

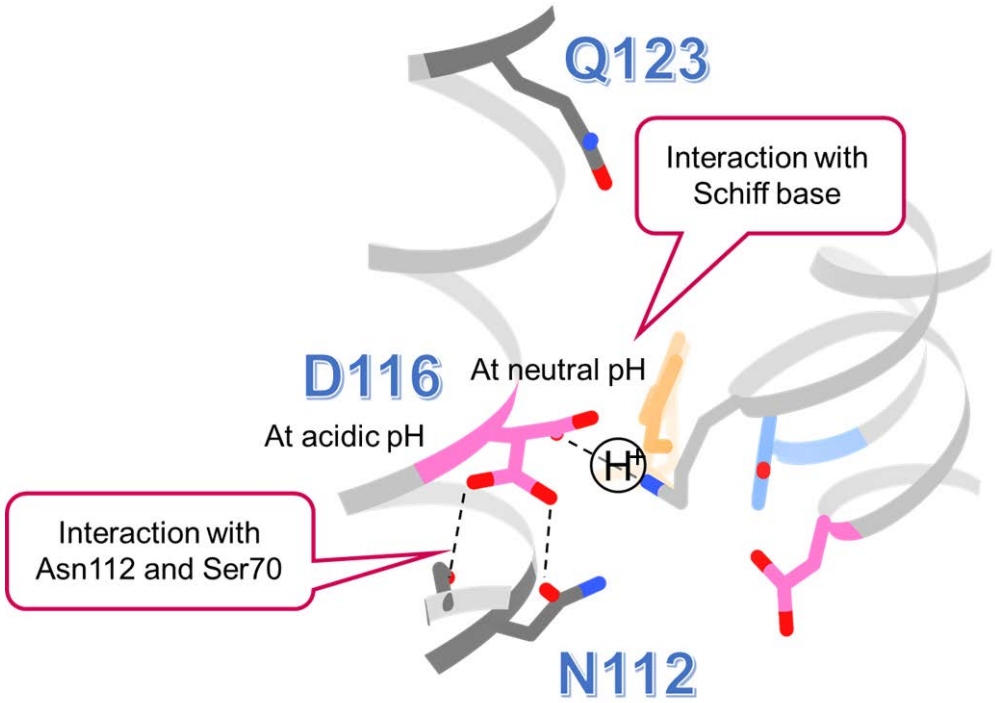

Figure 11. NDQ motif in KR2 and conformation of Asp116 at neutral and acidic pH.

Pumping assay and ion selectivity

Dual-functional KR2 were proved as shown in Figure 12. The experiment was conducted by observing the light-induced pH change of solution with *E.coli* cells which target proteins are over-expressed. KR1 in 100 mM NaCl showed pH decrease under light-irradiation and no change with addition of protonophore, carbonylcyanide-m-chlorophenylhydrazone (CCCP). CCCP destroys the proton gradient created in a living cell membrane, thus, increase in pH change in pump assay indicate the secondary proton movement across the membrane. The decrease in pH reveals the acidification of solution was induced by the proton transportation to extracellular side under light. KR2, on the other hand, showed increase in pH with light and further increase with addition of CCCP. Addition of both protonophore, CCCP, and ionophore, tetraphenylphosphonium bromide (TPP^+), induced no pH change which suggests the transportation of non-proton ion. By the ion alteration in solution revealed that KR2 transports Na^+. Furthermore, KR2 in 100 mM KCl showed similar pattern as KR1 showing that

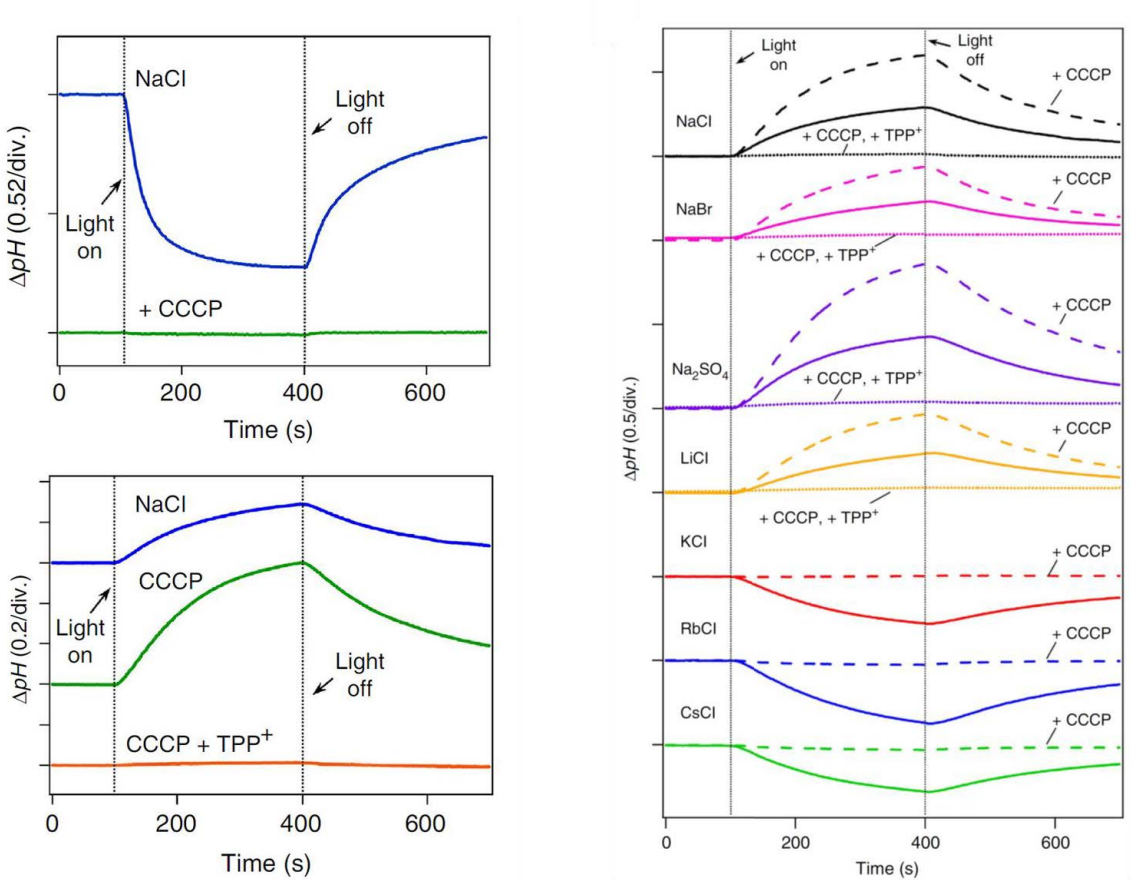

Figure 12. Pumping assay of KR1 and KR2 and ion selectivity of KR2.
(Left top) Pump assay of KR1 in 100 mM NaCl without (blue) and with (green) CCCP. (Left bottom) Pump activity of KR2 in 100 mM NaCl without (blue) and with (green) CCCP and with CCCP+TPP^+ (orange). (Right) Pump activity of KR2 in solutions with various ions. Adopted from [12].

proton transportation is occurring in this solution. Alteration of alkali metal ion revealed the ion selectivity of KR2 that Na^+ and Li^+ are transportable, but not K^+ or larger alkali metal ions and instead pumps proton.

Ion selectivity among alkali metal ions is also controlled at the cytoplasmic side. Konno et al. showed that pore formation with Gly263 and Asn61 at the cytoplasmic side prevented entry of K^+ or larger ions into the protein. In addition to Na^+ pump, Li^+ pump was observed in LiCl indicating that the water molecules bound around ion are taken off when ions are taken up to the protein since hydrated radius of Li^+ is larger than that of Na^+. The mutation to G263 and N61, G263F/N61L mutant, in which mutant the entrance was expanded by the induction of bulky residues, allowed uptake of larger ions such as cesium.[197] Only the change at cytoplasmic side enabled the Cs^+ pump, retinal-binding site and extracellular side can adapt larger ions to pump. The space at extracellular side is large enough to allow the iodide ion binding as was observed in iodide-single-wavelength anomalous diffraction (I-SAD),[198] hence, ion selectivity can be controlled at the cytoplasmic side.

Although the ion selectivity of alkali metal ion is size dependent, the selectivity in Na^+ and proton remains unclear. The pump activity assay of WT-KR2 revealed the increase in pH when light-irradiated under CCCP-contained solution compared to that without CCCP.[12] The transporting ion can be mainly determined by the concentrations of proton and Na^+. The kinetics of M-intermediate was observed in time-dependent absorption change to reveal the two separate photocyclic pathways for proton and Na^+ pump.[193] At the relaxation of M-intermediate and formation of O-intermediate, protons or sodium ions are taken up which was well shown by the accelerated O formation at high NaCl concentration.[12] The rate constant for proton pump was much larger than that for Na^+ pump at neutral pH; k_H/k_{Na} was 8700 at pH 8.0, 8600 at pH 7.0 and 7200 at pH 6.4. The midpoint NaCl concentration (CM) was 90 μM at pH 8.0 and increased at lower pH.[193] The similar competitive uptake of proton and Na^+ was reported in *Gillisia limnaea* rhodopsin (GLR) where GLR does not pump proton, thus, uptaken proton is soon released to the same side i.e. cytoplasmic side.[185] The equilibrium of the competitive transportation of these ions, however, is biased to pump Na^+ dominantly in marine salt condition where concentrations of proton and sodium ion are 1×10^{-8} M and 0.5 M, respectively.

Mutational and spectroscopic studies on KR2

Kinetics on the photocycle of KR2 was shown by flash-photolysis.[12] Sample reconstituted in DOPC membrane and suspended in 100 mM NaCl at pH 8.0 showed K-, L⇄M-, O-intermediates with their time constants of 26 ± 3 μs, 1.0 ± 0.1 ms, and 7.9 ± 0.3 ms and 112 ± 13 ms, respectively, The sample reconstituted in nanodiscs showed similar results of 40 us, 1.2 ms, and 3.7 ms and 30 ms for the life time of K-, L/M- and O-intermediates, respectively.[199] H^+ pumping photocycle in 100 mM KCl at pH 8.0 is completely different showing only K-, L-, and L⇄M⇄O-intermediates based on the calculation from transient absorbance change at 525, 420, 472 and 605 nm.[12]

Photocycle and sodium-ion pumping mechanism of KR2

Before the crystal structure was solved, NaR was guessed to possess sodium ion binding site as chloride-pumping *Np*HR has binding site at retinal Schiff base. This type of binding can be detected by maximum absorption wavelength where *Np*HR showed change of > 20 nm.[200] Contradictory, no color change was monitored for KR2 (523.7 nm in the existence of 100 mM NaCl and 522.6 nm in the absence).[12] These data suggested the binding site is in distant from retinal.

For these reasons, acidic and possible amino residues were targeted of mutational studies. Measurement of ATR-FTIR upon exchange of 50 mM NaCl/KCl revealed the spectral change in some mutants such as R109A, D116N, D251N, N112D, BC-loop and H30A. Here, each loops were introduced D/N and E/Q mutations.

Retinal absorbs light and triggers retinal conformational changes, followed by structural changes of functional residues around retinal that result in pumping of sodium ions. These structural changes comprise a cyclic pathway that follows formation of K, L⇄M, and O intermediates through flashphotolysis in the presence of Na^+.[12] Mutational and crystallographic studies suggested that an interaction between the protonated Schiff base and the counterion Asp116 plays a key role in the pumping function. In addition, Fourier transform infrared spectroscopy (FTIR) studies showed differing frequencies of N−D stretching of the KR2 Schiff base compared with that from BR, indicating a slightly stronger hydrogen bond between Asp116 and the Schiff base.[201] Formation of the J intermediate proceeds quickly after photoexcitation and is involved in the isomerization of chromophores.[202] Subsequently, the Schiff base proton is transferred to Asp116 at the M intermediate, followed by flipping of the Asp116 side chain to form hydrogen bonds with Ser70 and Asn112. Sodium ions are then taken up from the cytoplasmic side, while the electrostatic barrier around the Schiff base is removed and bind temporarily to Asp251 and Asn112 at the O intermediate.[185,196] Protonated Asp116 then returns the proton to the Schiff base, thus preventing the back flow of sodium ions to the cytoplasmic side. Transportation of sodium ions might be hampered by the positive charge of Arg109, although additional inversions may allow the transfer of sodium ions to the extracellular side. The Na^+ releasing site at extracellular side of the protein is completely shielded by the N-helix with some displacements in extracellular loop 1 (ECL1).[10] The acidic residues at extracellular side, Glu160 and Arg243, homologous to Glu194 and Glu204 in bacteriorhodopsin, do not affect Na^+ pump as revealed by E160A and R243A mutants, thus, suggesting a different pathway from *H. salinarum* bacteriorhodopsin (*Hs*BR) or halorhodopsin (*Hs*HR) for Na^+ release and large conformational changes of N-helix and/or transmembrane region during photocycle.

Na^+ translocation was shown by molecular dynamics (MD) simulations as well that Na^+ putatively binds to three sites during photocyclic pathway: Gln123, Ser60 and Ser64 at cytoplasmic side in the K/L state, Asp116 in the K/L state, and Asn112 and Ap251 in the M state.[203] They additionally showed

the movements of water molecules in the helix bundle and helices at cytoplasmic side during K/L to M transition that the water connectivity between cytoplasmic and extracellular side is broken by Leu120 and the distance between intracellular terms of helix B and G got shortened. The pump mechanism in KR2 is described as Panama Canal model as two gates control the ion translocation, Asp116-Schiff base interaction and Arg109, but the energy level change differs at state 7-to-8 transition.[204]

KR2 functions both as a sodium ion pump and as a proton pump, and these pump functions are in competition. Specifically, the rate constant for Na^+ uptake is much smaller than that of H^+ uptake. However, at higher sodium concentrations, sodium ion pumping becomes the major activity.[193] Following mutation of the NDQ motif in KR2 to a DTD motif with additional residues at extracellular Na^+-binding sites, the N112D/D116T/Q123D/D102N KR2 mutant lost Na^+ pumping functions and was converted to a H^+ pump in the presence of high concentrations of NaCl.[113] Hence, the NDQ motif and sodium ion-binding site at the extracellular side are essential for the Na^+ pumping function.

Application to optogenetics

KR2 works as an inhibitory optogenetics tool, like HR and AR3. This was tested by various means.[183] Robust outward photocurrent was evoked when green light exposed with voltage-clamp recordings independently to the voltage. Under current-clamp mode conditions, injected rectangular depolarizing current evoked repetitive spikes. The generation of an action potential was completely blocked during the green light irradiation where the membrane potential was hyperpolarized by KR2-activation. The stable KR2-mediated inhibition of spiking remained effective for more than one minute. A KR2–Venus fusion protein expressed *Caenorhabditis elegans* neurons for the examination of neural activity control *in vivo* showed the slowed forward locomotion by green light illumination, suggesting the decreased neural activity by the KR2 photoactivation under the experimental conditions. This is the first example of the successful application of a eubacterial rhodopsin to optogenetics.

Further characteristics of KR2 for application were tested as well as other 12 sodium-ion pumping rhodopsins (NaR).[187] A whole-cell patch clamp measurement using mammalian cells, ND7/23, and enhanced green fluorescent protein (eGFP)-tagged NaRs, revealed that KR2 exhibited small photocurrent in the range of 1 to 2 pA, which is similar to other two NaRs and rather weak compared to other six NaRs showing >10 pA. This result is in agreement with the weak fluorescence signals at the plasma membrane showing the poor membrane expression. Like previous report that KR2 constructs carrying an endoplasmic reticulum (ER) export signal and enhanced yellow fluorescent protein (eYFP) exhibited larger photocurrents in cortical neurons and cultured cells,[189] replacement of the C-terminally fused GFP to an ER export signal and eYFP allowed the larger photocurrents compared to the original construct of KR2-eGFP.

Similarly to the various channelrhodopsin variants, KR2 variant with altered ion selectivity

was engineered.[183] Two residues forming the intracellular vestibule, Asn61 and Gly263, were mutated to see the function. One of the variants with double mutation N61P/G263W preferentially transferred K^+ over Na^+. Although the K^+/Na^+ selectivity ratio is still not very high (1.17 ± 0.15), this works more efficiently as a K^+ pump *in vivo* because of its ten times higher concentration of K^+ than that of Na^+. This is a first example of light-driven K^+ pump, thus, provides a further possibility of expanding their applications of KR2 variants.

The chimeric NaR of KR2 and *Ia*NaR, I_1K_6NaR, exhibited some improvements in the membrane targeting and photocurrent properties over native NaRs.[189] I_1K_6NaR is a chimera protein which combined trans-membrane domain (TMD1) (Met1-Val52) of *Ia*NaR and TMD2-7 (Asp54-Ser280) of KR2. The I_1K_6NaR-expressed cortical neurons were stably silenced by green light illumination for a certain long duration. With its rapid kinetics and voltage dependency, photo-activation of I_1K_6NaR would specifically counteract the generation of action potentials with less hyperpolarization of the neuronal membrane potential than KR2, thus, it would be a potential candidate of the effective optogenetic neural silencer with minimal influence on the ionic/pH balance.

Understanding of retinal-binding pocket

Microbial rhodopsins have functionally important residues around retinal that transmit signals of changes in retinal conformation to the protein side. Previous crystallographic studies revealed the presence of Asp116 and Asp251 near the retinal Schiff base. In subsequent investigations, mutation of Asp116 to Asn caused a wide shift in the maximal absorption wavelength from 524 to 570 nm.[196] In addition, a D116N mutant lost pumping activity,[12] indicating that Asp116 is requisite for the function of this transporter. In addition, X-ray crystallographic data demonstrated that Asp116 takes varying conformations at neutral and acidic pH, and Asp116 formed hydrogen bonds with Ser70 and Asn112 at pH 4.0 and faced away from the Schiff base. At low pH, the counterion is protonated and shows an M-like structure. In contrast, after samples had been soaked in pH 7.5−8.5 buffer, ~35% of Asp116 residues faced the Schiff base and the other 65% took the same conformation that they did under acidic conditions.[183] Hence, conformations of Asp116 are highly dependent on pH, although the ensuing mechanisms remain poorly characterized. Gushchin et al. recently showed that Asp116 is flipped away from the Schiff base in the ground state.[205] Flipping of the counterion suggests that this conformational change is characteristic of KR2 during photocycles (Figure 13). The second Asp residue near the Schiff base is Asp251 and is located opposite Asp116 (Figure 14). The side chain of Asp251 is less mobile under varying pH conditions and forms hydrogen bonds with Tyr218 and Arg109, either directly or via water molecules.[183,195] Mutational studies indicated losses of the pumping ability of D251N similar to those observed for D116N,[12] which is unusual considering that BR D212N remained active.[206,207] Therefore, unlike in other rhodopsins, Asp251 is essential for the sodium ion pumping function of KR2 (Figure 14).

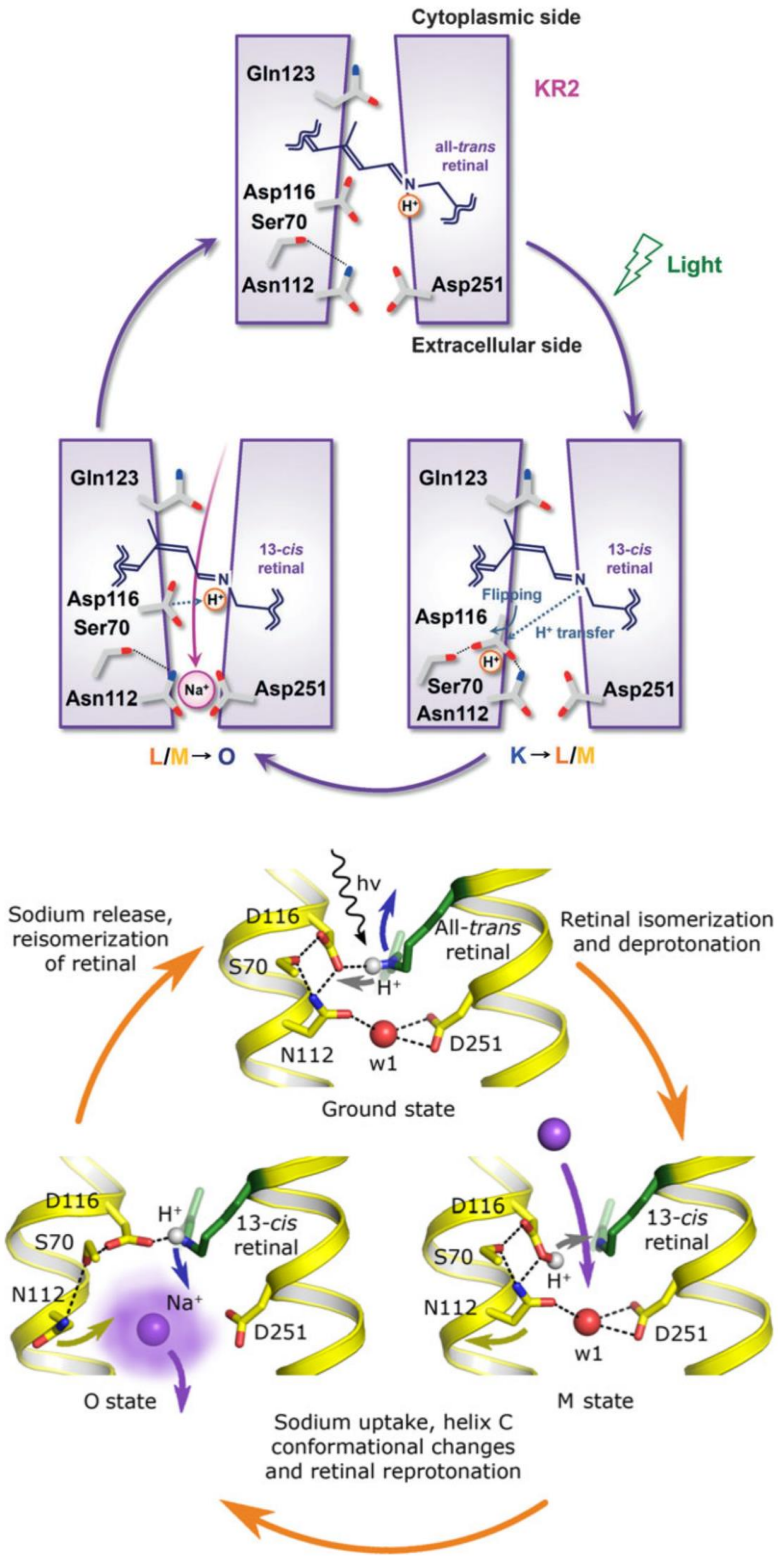

Figure 13. Photocycle based on the crystallographic structure.
(Top) Photocycle presented in [196] (Bottom) Photocycle presented in [205].

The residues interacting both with Asp116 and Asp251 during photocycle is Asn112. The mutational study of this residue replacing with 19 different amino acids revealed the importance of Asn112.[208] The mutants of this residue can be classified into three phenotypes. One phenotype is WT-like Na^+/H^+ compatible pump which was seen in N112D, N112G, N112S and N112T mutants. These four mutants pump H^+ even in 100 mM NaCl, the competition of Na^+ and H^+ pumps are biased probably caused by the increased efficiency of proton uptake. Another phenotype is exclusive H^+ pump, which was seen when replaced by A, C, P, V, E, Q, L, I, M, F and W. Replacement of Asn112 to non-hydrogen bonding amino acids, A, C, P, V, L, I, M and F, possibly lacks hydrogen bond with Asp116 and does not open the gate for Na^+ transportation. Insertion of bulky residues, such as F and W, largely changed structure of active center to pump only small amount of proton whereas N112E and -Q showed proton pump activity. This suggests the length of the side chain influences on the gate opening at M-intermediate and stable environment at O-intermediate. The other phenotype showed no pump activity which consists of N112H, -K, -Y and –R. In spite of the presence of proton acceptor, D116N, proton transfer from Schiff base to Asp116 did not occur possibly because of the formation of hydrogen bond with Asp116 which presumably lowered pK_a of Asp116.

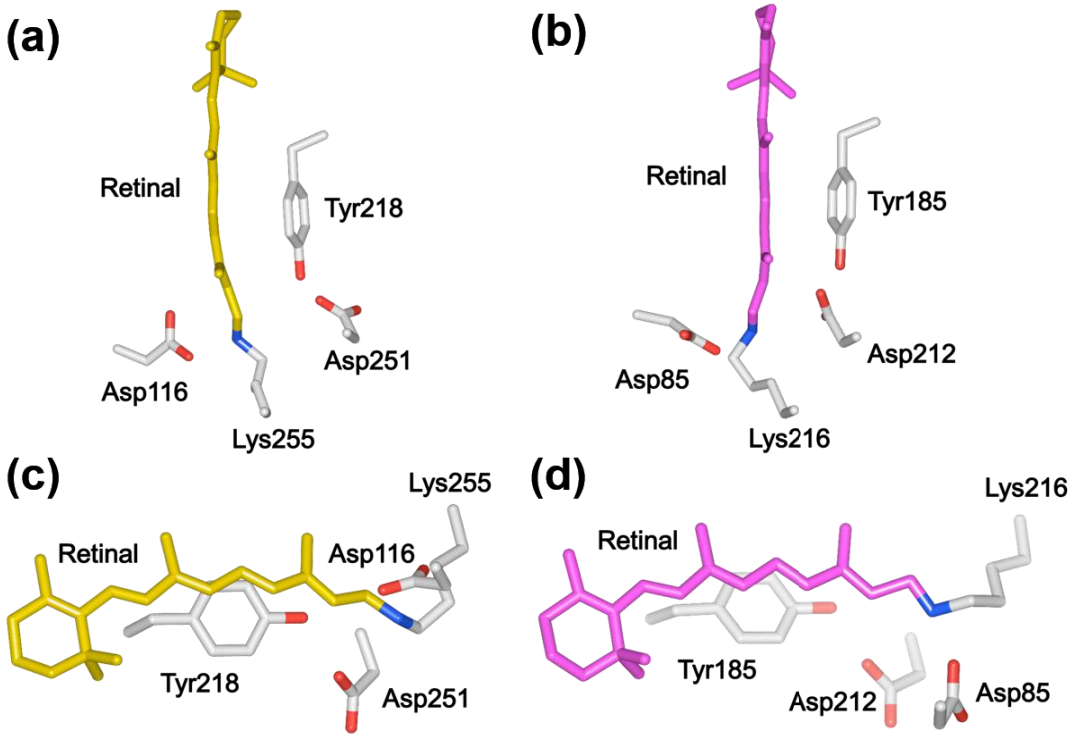

Figure 14. Structure of the retinal-binding pocket.
(a) Top view and (c) side view of *Krokinobacter* rhodopsin 2 (KR2, Protein Data Bank entry 3X3C). One of two rotamers of Asp116 is shown. (b) Top view and (d) side view of bacteriorhodopsin (BR, Protein Data Bank entry 1C3W).

Rhodopsins studied by solid-state NMR

Solid-state nuclear magnetic resonance has been used in structural analyses of less mobile proteins, such as membrane proteins. Hence, structural determinations of whole protein and functionally related local conformational changes have been performed. Among these, structural determinations of *Anabaena* sensory rhodopsin were performed using three-dimensional chemical shift correlation techniques and showed the whole structure in a lipid environment.[148] In addition, Park et al. determined the structure of seven-transmembrane chemokine receptor CXCR1 in a lipid environment.[209] To observe local changes in conformation, retinal and other residues are used as probes for local structural changes during photocycles. Accordingly, Lakshmi et al. demonstrated chemical shifts of retinal in BR in the ground state and in photointermediates.[210] Similarly, Ahuja et al. and Eilers et al. studied TyrCζ in bovine rhodopsin and showed changes in hydrogen bond strengths of some Tyr residues in the active state.[211,212] These studies indicate the utility of TyrCζ NMR signals as probes for determining hydrogen bond strength.[213–215] Thus, in the study presented here, we observed a hydrogen bonding strength of Tyr218 with Asp251 in KR2 using TyrCζ-labeled samples.

Aim

To reveal the sodium ion pump mechanism fully, we need to reveal the photo-induced structural change of retinal-binding pocket addition to the data shown here. Some residues are speculated to change dramatically at the M- and O-intermediate where Schiff base becomes deprotonated and sodium ion is taken up close to retinal at M-intermediate and then it binds to Asp251 and Asn112 at the O-intermediate. Relaxation time constants are 1.0 ms for the M-intermediate and 7.9 ms and 112 ms for the O-intermediate in DOPC membrane revealed by flash-photolysis.[12] We have been reporting the method of trapping photo-intermediates using *in-situ* photo-irradiation solid-state NMR. This method allows the continuous irradiation of light to microbial rhodopsin sample during measurements, thus, enables to trap intermediates steadily.[178,179,216] With this method, we try to understand the structure of KR2 at photo-intermediates to investigate the sodium ion pump mechanism further.

Materials and Methods

Sample preparation

Culture, expression and purification

KR2 samples with six histidines at the C terminus were overexpressed in *Escherichia coli* strain C41(DE3) cultured in M9 minimal medium and then purified. To perform NMR analyses, we labeled

samples with stable isotopes to obtain [14,20-^{13}C]retinal, [U-^{13}C]Asp, [phenol-4-^{13}C]Tyr, [6-^{13}C]Lys WT KR2 and [14,20-^{13}C]retinal, [1,4-^{13}C]Asp, [phenol-4-^{13}C]Tyr, [7-^{15}N]Lys WT KR2 (Figure 15). For comparison with acidic WT, [14,20-^{13}C]retinal, [phenol-4-^{13}C]Tyr, and [7-^{15}N]Lys D116N KR2 were prepared. Expression was done with three steps of culture: 19 hours of pre-culture with 100 mL M9 medium with freeze stock of KR2 transformed *E. coli* in 300 mL flask without baffles, 22 hours of main culture with 1 L M9 medium and 10 mL of bacterial solution from pre-culture in 2 L flask or 2 L medium with 20 mL of bacterial solution in 3 L flask. Induction was done when O.D. value was at 0.5, which was 7 hours from the start. Before induction 100 mg of labeled amino acids ([phenol-4-^{13}C]Tyr, [7-^{15}N]Lys) in 1 L medium were mixed into media and at the induction point 1 mL of 0.1 M IPTG, 500 μL of 10 mM [14,20-^{13}C]labeled retinal was added. Shaker was set to 180 rpm, 37°C for pre-culture and babbling was used for main culture instead of shaker in an incubator at 37°C.

The protein was solubilized in 1~2% n-dodecyl-b-D-maltoside (DDM) and purified via Co-affinity column chromatography. Buffer used for washing and elution were followings: For washing the buffer of 3 M NaCl, 500 mM Imidazole, 500 mM MES, 1% DDM, pH 6.5 was used. For elution the buffer of 300 mM NaCl, 300 mM Imidazole, 50 mM tris(hydroxymethyl)aminomethane (Tris)-HCl, 0.1% DDM was used. Buffer was changed by dialysis using dialysis buffer of 300 mM NaCl, 50 mM Tris-HCl, 0.05% DDM and kept in refrigerator before reconstitution into lipid membrane.

Samples were separately reconstituted into widely used 1-palmitoyl-2-oleoyl-sn-glycero-3-phosphoethanolamine (POPE)/1-palmitoyl-2-oleoyl-sn-glycero-3-phospho(1′-rac-glycerol) (POPG) membranes (3:1 POPE:POPG ratio, 1:20 protein:lipid ratio) (Figure 16) for the study of the bacterial membrane proteins as previous work characterizing KR2.[193,217,218] Liposome was prepared with buffer of 100 mM NaCl, 10 mM Tris- H_3PO_4, pH 8.0. Subsequently, samples were suspended first in 20 mM Tris-H_3PO_4 buffers at pH 8.0, 6.0, 5.0, or 4.0 with 200 mM NaCl or in 20 mM Tris-H_3PO_4 buffer at

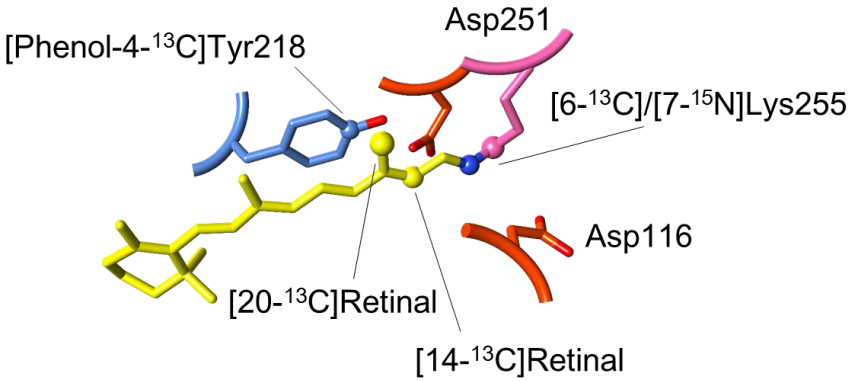

Figure 15. Labelling position at retinal-binding site.
Spheres represent the ^{13}C (yellow, light blue and pink) or ^{15}N (blue) isotope labeled position.

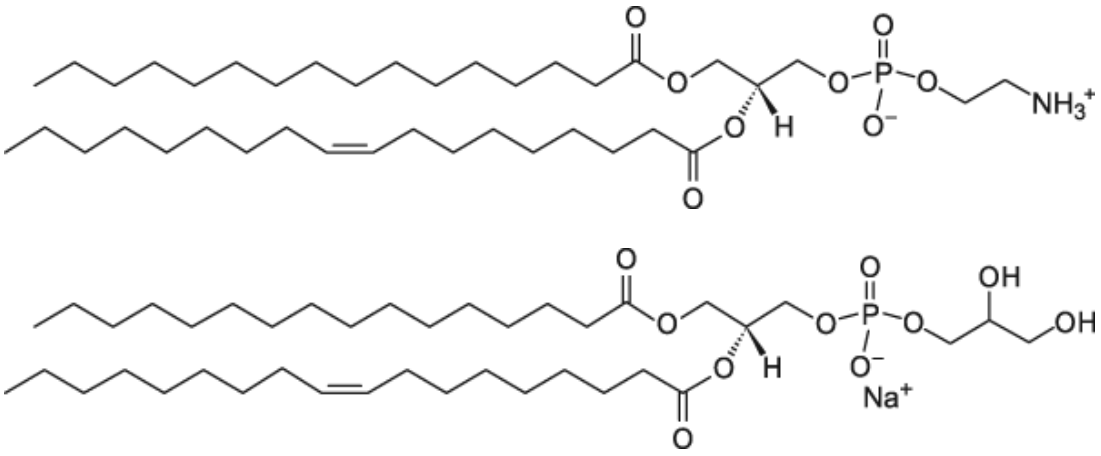

Figure 16. Molecular structure of POPE and POPG.
(Top) 1-palmitoyl-2-oleoyl-sn-glycero-3-phosphoethanolamine. (Bottom) 1-palmitoyl-2-oleoyl-sn-glycero-3-phospho(1′-rac-glycerol).

---

pH 8.0 with 200 mM CsCl, then, exchanged with 10 mM Tris-H_3PO_4 buffers at pH 8.0, 6.0, 5.0, or 4.0 with 100 mM NaCl or in 10 mM Tris-H_3PO_4 buffer at pH 8.0 with 100 mM CsCl.

Media protocols

Components of media for *E. coli* culture is shown in Tables below.

Table 2. Components for LB medium (per 1 L medium)

NaCl	10 g
Bacto-tryptone	10 g
Yeast extract	5 g

Table 3. Components for M9 medium (per 1 L medium)

NaCl	0.5 g
Na_2HPO_4	7 g
KH_2PO_4	3 g
Biotin	20 mg
Thiamine	20 mg
10 mM $FeCl_3$	128 μL
1 M $MgSO_4$	1 mL
50 mM $MnCl_2$	1 mL
[U-^{13}C] Glucose	2 g
[^{15}N] NH_4Cl	0.5 g

UV-Vis characterization

Lambert–Beer law is the easiest way to calculate concentration of purified protein by comparing the intensity of incident light and transmitted light. The difference between these intensities, absorbance [-], is shown bottom.

$$\mathrm{A} = -\log\frac{I}{I_0} = \log\frac{I_0}{I}$$

Here, I_0 is intensity of incident light and I is that of transmitted light. The ratio of these two are termed as transmittance, T [%].

$$\mathrm{T} = \frac{I}{I_0} \times 100$$

In order to obtain concentration from absorbance value, equation bottom is used.

$$\mathrm{A}(\lambda) = \log\frac{I_0(\lambda)}{I(\lambda)} = \varepsilon_\lambda c l$$

ε_λ [mol^{-1} ・ L ・ cm^{-1}] is molar extinction coefficient as cell length, l [cm] and sample concentration, c [mol/L] are used.

Sample for NMR measurement were calculated as followed. Purified bacteriorhodopsin is kept in HEPES buffer solution. Sample are diluted 10 times with buffer for UV-Vis measurement and put into cuvette. White light is irradiated to diluted sample and absorbance spectra is obtained. There is peak with maximum absorbance around 525 nm which is from retinal in KR2 (Figure 17). Absorbance value is applied to the equation above:

$$\mathrm{A}(\lambda) = \varepsilon_\lambda c l$$

$$10 \times \mathrm{Abs} = 50000 \times c \times 1$$

Molecular weight of KR2-WT is about 32000 [-][219] and molecular extinction coefficient of KR2-WT is 50000 [mol^{-1} ・ L ・ cm^{-1}][12]; therefore, yield of the protein can be obtained as follows.

$$\mathrm{V\ [L]} \times \mathrm{c\ [mol/L]} \times 32000 \times 10^3\mathrm{[g/mol]} = \mathrm{Yield_{KR2}\ [mg]}$$

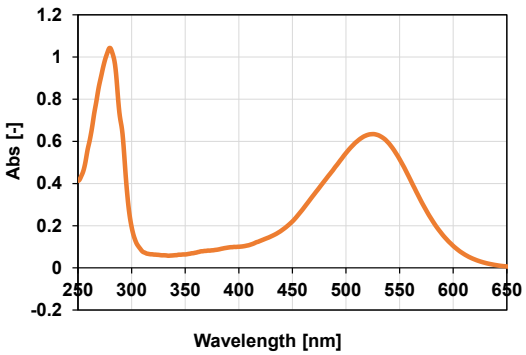

Figure 17. UV-Vis spectrum of solubilized KR2.

Solid-state NMR measurements

Reconstituted samples at pH 8.0, 6.0, 5.0, and 4.0 were concentrated by centrifugation and separately packed into 4.0 mm zirconia rotors after washing more than three times with 20 mM Tris-H_3PO_4, 200 mM NaCl buffer at targeted pH and then washed more than three times with 10 mM Tris-H_3PO_4, 100 mM NaCl buffer at targeted pH to exchange buffer fully. ^{13}C or ^{15}N NMR experiments were then performed at 278 K, and the magic angle spinning (MAS) speed was adjusted to 10.0 kHz on a Bruker Avance III spectrometer operated at 14.1 T (600 MHz as the ^{1}H Larmor frequency) with an E-free probe. ^{13}C CP-MAS, ^{15}N CP-MAS, and ^{13}C–^{13}C dipolar assisted rotational resonance (DARR) two-dimensional NMR[151,152] were applied with a mixing time of 500 ms[174,220] at each pH, and 64 points in the f1 dimension and 2048 points in the f2 dimension were acquired. Data for the sample with Tris-CsCl buffer were obtained using PDSD at 283 K. Spinal 64 proton decoupling[221] of 80 kHz was employed during acquisition. ^{13}C chemical shifts were referenced to the carbonyl resonance of glycine powder at 176.03 ppm [tetramethylsilane (TMS) at 0.0 ppm], and ^{15}N chemical shifts were referenced to Gly powder at 11.59 ppm (NH_4NO_3 at 0.0 ppm[222]).

Results and Discussions

Signal assignment of ^{13}C–^{13}C correlation peaks and retinal configuration.

In order to understand structure of retinal-binding pocket, we applied DARR to KR2 sample. DARR is a way to observe the magnetization transfer between ^{13}C nuclei.[151,152] Mixing time was set to 500 ms which allows to pick signals of labeled atoms in a distance of ~7 Å in order to observe ^{13}C–^{13}C correlation peaks of retinal with Tyr, Asp and Lys residues. This allows selective and specific observation of the structure in the vicinity of retinal by detecting magnetization transfer from retinal to nearby amino acids in spite of the fact that not only purposing amino residues but also all Tyr, Lys and Asp residues in KR2 are labeled during overexpression process of *E. coli*.[220] Figure 18(a) shows correlation peak between retinal C20, retinal C14, TyrCζ and LysCε at ground state at pH 8.0. Correlation peaks between retinal and TyrCζ or LysCε are assigned as Tyr218 and Lys255 (Table 4) based on the structural information from crystallographic data. Clear correlation peak of Asp was not observed. Formerly, the correlation peak between His75-Asp97 in [U-^{13}C]His and [1,4-^{13}C]Asp-labeled GPR has been successfully observed even though Asp scrambled to some other residues.[223] Thus, it can be detected with NMR, but we were unable to observe due to reduced isotope-labeling efficiency by the scrambling effect.

We used [14, 20-^{13}C]labeled retinal as C20 is a good probe for 13-*cis*/*trans* conformation change and C14 for 15-*syn*/*anti*.[224] Typical chemical shift of retinal C20 is about 13.0 ppm for all-*trans* and about 22.0 ppm for 13-*cis*, 15-*syn* at ground state. As for C14, retinal with all-*trans*

conformation shows peak at around 120.0 ppm and the one with 13-*cis*, 15-*syn* shows peak at about 110.0 ppm.[163] DARR spectra in Figure 18(a) shows correlation peaks of C20 and C14 at 14.2 ppm and 120.5 ppm, respectively; hence, we assigned retinal conformation of KR2 at ground state to be all-*trans,* 15-*anti* form. Chemical shift of retinal did not change at neutral and acidic pH. Additionally, we observed the D116N mutant for comparison with acidic WT, which showed retinal peaks at 13.2 and 119.8 ppm for C20 and C14, respectively (Figure 19).

DARR spectra also gave information about [^{13}Cε]Lys255. The chemical shifts of this are 52.05 ppm at pH 8.0. No significant change in chemical shift upon pH-change was observed. In the case of BR, all-*trans*, 15-*anti* retinal and 13-*cis*, 15-*syn* retinal at ground state showed peak at 53 ppm and 48 ppm, respectively.[225] This indicates that retinal conformation in KR2 is all-*trans*, 15-*anti*, but the chemical shift is 1 ppm towards that of 15-*syn* conformation.

Chemical shifts of retinal C20, C14 and Lys255Cε did not change by acidification (Figure 18(b)). This is corresponding to the case of bacteriorhodopsin showing change in chemical shift of

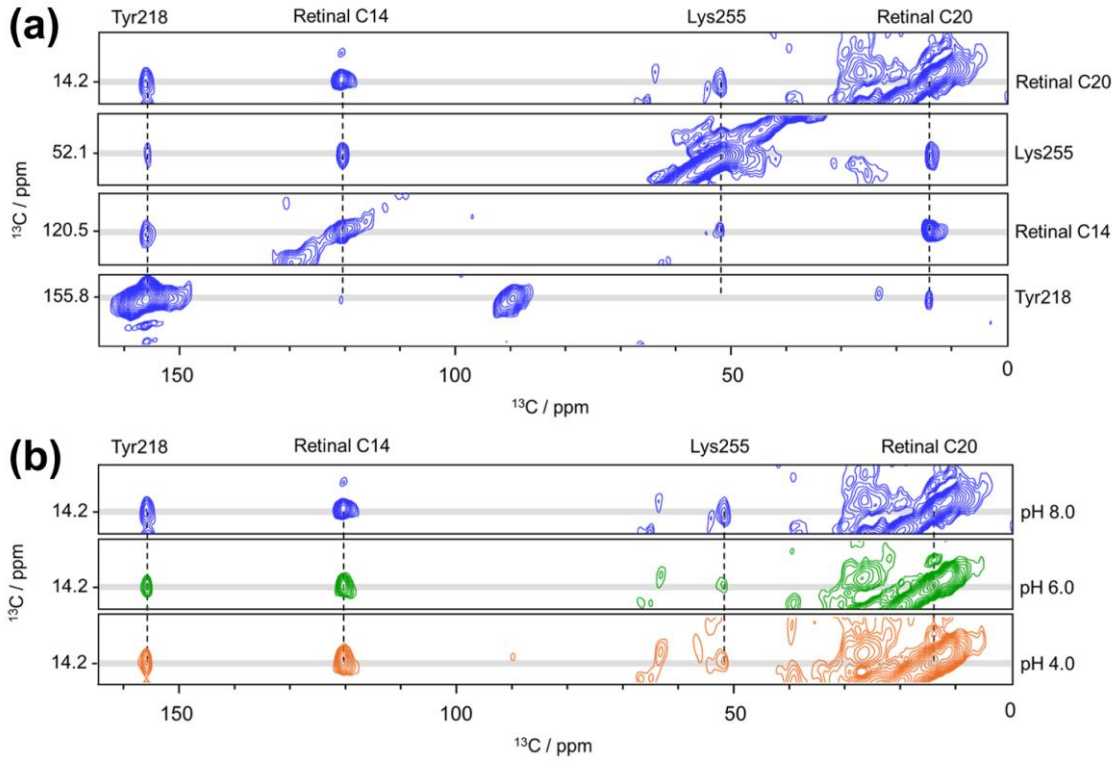

Figure 18. ^{13}C–^{13}C DARR spectra of wild-type KR2 in a POPE/POPG membrane in a Tris-NaCl solution.
(a) Correlation peaks of labeled residues at pH 8.0. Cross peaks and diagonal peaks are represented by the gray line. (b) Comparison of cross peaks at pH 8.0 (top, blue), pH 6.0 (middle, green), and pH 4.0 (bottom, orange). All columns show correlations with retinal C20. Cross peaks and diagonal peaks are represented by the gray line.

Table 4. ^{13}C and ^{15}N chemical shift values of KR2 in POPE/POPG.

	WT pH 4.0 NaCl	WT pH 6.0 NaCl	WT pH 8.0 NaCl	WT pH 8.0 CsCl	D116N pH 8.0 NaCl
Retinal $^{13}C20$	14.2	14.3	14.2	13.9	13.2
Retinal $^{13}C14$	120.5	120.5	120.5	120.9	119.8
Tyr218 $^{13}C\zeta$	155.8	155.8	155.8	155.9	155.7
Lys255 $^{13}C\varepsilon$	52.1	52.0	52.1	52.1	
Lys255 $^{15}N\zeta$	152.5	150.8	150.2	-	153.8, 145.2-140.4

[1)] Referenced to glycine powder for ^{13}C and ^{15}N.

smaller than 1 ppm. Hence, configuration of retinal remains the same as all-t*rans*, 15-*anti* at low pH. Retinal chemical shift showed slight change with sample suspended in Tris/CsCl solution, but it was very small (Figure 20).

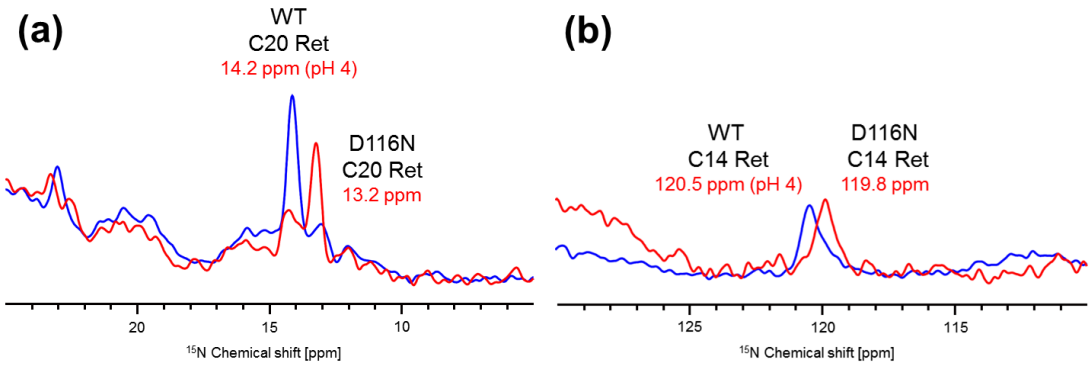

Figure 19. Comparison of retinal chemical shift between WT and D116N mutant.
^{13}C CP-MAS spectra of (a) retinal C20 and (b) retinal C14 of WT-KR2 at pH 4.0 at 278 K (blue) and D116N-KR2 at pH 8.0 at 268 K (red).

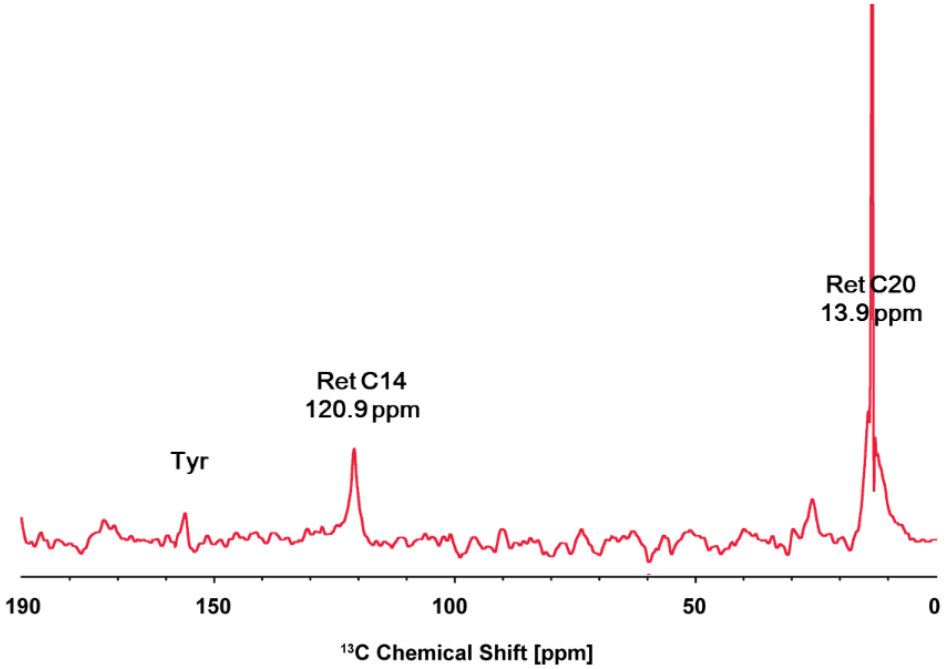

Figure 20. Cross section of C20 retinal in KR2 in CsCl solution.
^{13}C-^{13}C PDSD slice spectrum of wild-type KR2 in POPE/POPG membrane in Tris/CsCl solution at around 283K. Slice spectrum is taken at 13.9 ppm showing correlation with retinal C20.

---

^{15}N Schiff base NMR signals at neutral and acidic pH.

[^{15}Nζ]Lys255 signal was observed as shown in Figure 21(a). ^{15}N CP-MAS spectrum at pH 8.0 showed Schiff base peak at 150.2 ppm. Peak at 11.7 ppm is for other ten Lys residues with no significant difference in the environment and peak in the middle is for natural abundance of backbone. Chemical shift of Schiff base reflects the retinal structure, therefore, has correlation with maximum absorption wavelength.[46,169,226] In Figure 21(b), correlation of Schiff base chemical shift and maximum absorption wavelength is plotted. Dotted line is provided by all-*trans* retinylidene model compounds with different counterions.[46,227] BR (all-*trans*) and *Natronomonas pharaonis* Sensory Rhodopsin II (*Np*SRII) are on the upper side of linear trend of model compounds. In the contrast, KR2 plot was below the line at pH 8.0.

The chemical shift changed upon pH-change as follows: 150.8 ppm at pH 6.0, 152.4 ppm at pH 5.0 and 152.5 ppm at pH 4.0. Peak shifted most widely between pH 6.0 and 5.0 despite the small change between pH 6.0 and pH 8.0 (Figure 21(a) and Figure 22) indicating the protonation of Asp116. In order to confirm the Schiff base change upon pH titration, we measured ^{15}N CP-MAS of D116N

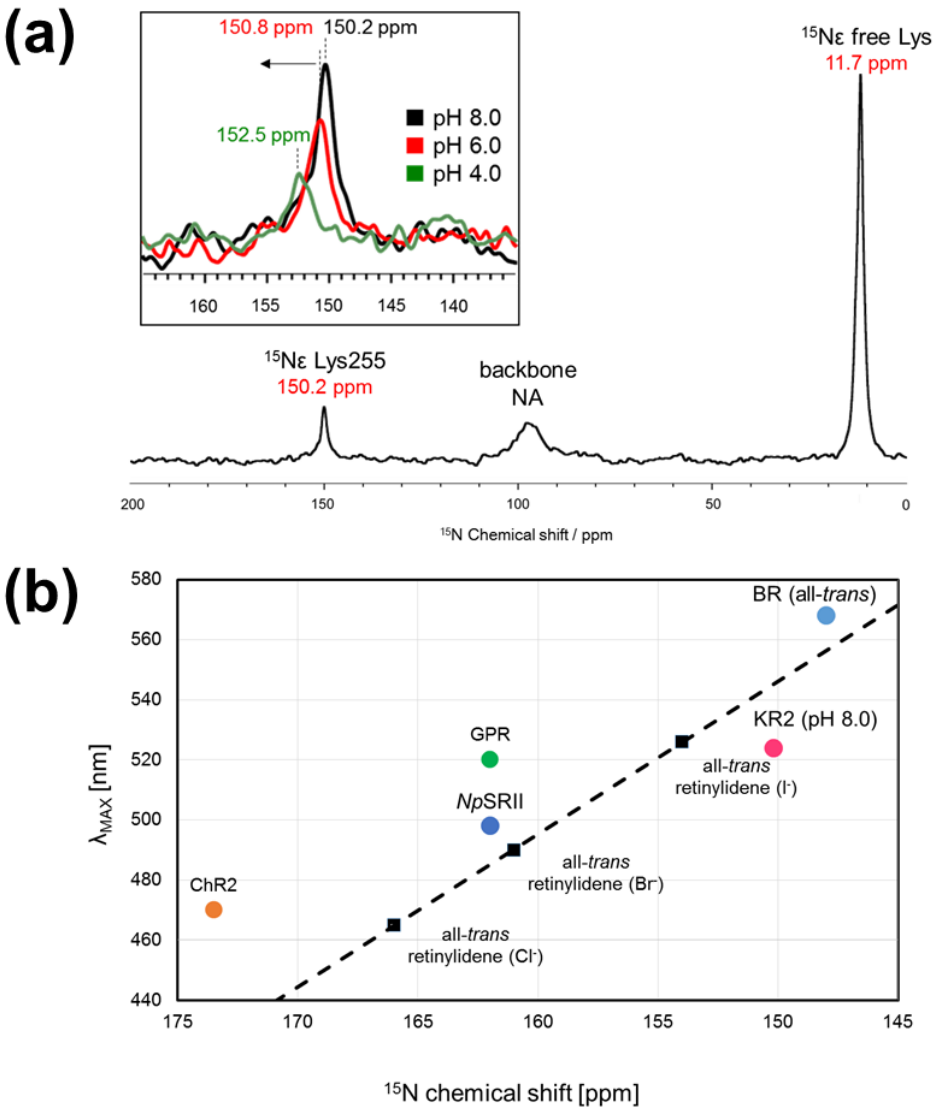

Figure 21. Schiff base signal in ^{15}N CP-MAS spectra.
(a) ^{15}N CP-MAS spectra. Peaks from left are free Lys, natural abundance backbone and Schiff base. In-set spectra are comparison of Schiff base peaks at pH 8.0 (black, 150.2 ppm), pH 6.0 (red, 150.8 ppm) and pH 4.0 (green, 152.5 ppm). (b) Correlation between ^{15}N chemical shift of Schiff base and maximum absorbance wavelength. Broken line is linear correlation of model compounds.

---

mutant (Figure 23). The chemical shift did not change. Thus, the change observed in WT-KR2 is caused by the protonation of D116. Since peaks of retinal C20, C14 and Lys255Cε did not shift upon pH-change (Figure 18(b)), retinal structure remains unchanged even at pH 4.0 except for protonated Schiff base.

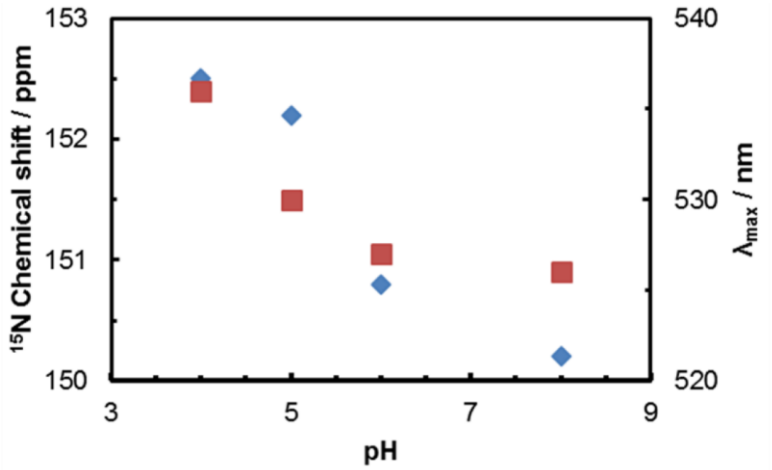

Figure 22. Changes in ^{15}N chemical shifts and maximum absorption wavelength of protonated Schiff base in WT KR2

pH dependence of ^{15}N chemical shift of Schiff base (blue) and maximum absorption wavelength (red).

Structure of the retinal-binding pocket and Schiff base interactions with Asp116.

^{13}C-^{13}C PDSD spectrum did not show change in chemical shift of Retinal C20, C14, Lys255 and Tyr218 in Tris/CsCl buffer compared to those in Tris/NaCl. This suggests that retinal-binding pocket is sodium ion-independent structure at ground state.

Correlation plot of ^{15}N Schiff base signal and maximum absorption wavelength showed unique plot of KR2. BR (all-*trans*) and *Np*SRII are on the upper side of linear trend of model compounds and KR2 plot below the line at pH 8.0 which represent the tilt around C15=N and N-Cε, respectively according to Eilers et al.[226] The blue-shift is caused by twist around single bond thus it can be caused by torsion around any single bond in retinal. However, lambda max change of D116N to about 565 nm and of D116A to about 578 nm suggest the importance of negative charge for color change. Therefore, blue-shift of KR2 is induced by torsion around N-Cε. This is induced by the unique location of Asp116 residue. KR2-Asp116 is located one helical pitch towards cytoplasmic side than BR-Asp85 (

Figure 14) or *Np*SRII-Asp75, therefore, close and strong interaction with counterion induced tilt of protonated Schiff base. In fact, it was reported that there is very strong hydrogen bond from sharp N-D stretching vibration at 2095 cm^{-1} by FTIR.[228] Crystallography showed two conformations of Asp116, thus, indicating two types of interactions with Schiff base; however, Schiff base signal seems to show one homogeneous structure. Still possibility remains that interaction of two conformations are similar

and showing only one signal or that one of two interactions was not detected because of low population or inhomogeneity.

Schiff base peak shifted most widely between pH 6.0 and 5.0 despite the small change between pH 6.0 and pH 8.0 (Figure 21(a) and Figure 22). Since peaks of retinal C20, C14 and Lys255Cε did not shift upon pH-change (Figure 18(b)), retinal structure remains unchanged even at pH 4.0 except for protonated Schiff base. This is probably caused by the protonation of Asp116, suggesting change in interaction with counterion. As KR2 in lipid membrane has multiple pK_a, (pK_{a1}=3.47, pK_{a2}=5.48, pK_{a3}=7.52)[12], the peak shift of Schiff base at lower pH may represent the pK_a of Asp116. All the crystal data provided by Gushchin et al. indicates that Asp116 orients away from Schiff base at a pH as high as 4.9.[205] These data support our NMR results in a sense that Asp116 changes its interaction and reorients at lower pH.

Chemical shift difference of protonated Schiff base was about 2 ppm between neutral and acidic condition. The small change in chemical shift indicates that protonated Schiff base has still interaction, probably with anonymous oxygen. This downfield shift is contradictory to the case of BR which showed upfield shift upon acidification ($BR_{all\text{-}trans}$ at neutral pH: 148 ppm, at acidic pH: 139, 132 ppm[229]) (estimated as NH_4NO_3 reference). In addition, report on Schiff base model compounds pointed out that the strong hydrogen bond of Schiff base proton with interacting oxygen induces downfield shift.[230] Considering this, Schiff base of KR2 seems to strengthen the interaction slightly with Asp116 at low pH by approaching Asp116 oxygen. However, the chemical shift change was small with 2 ppm, thus, indicating a slight increase in strength. Crystal structure at acidic condition showed Asp116 side chain at slightly distant from Schiff base which is contradictory to our result.

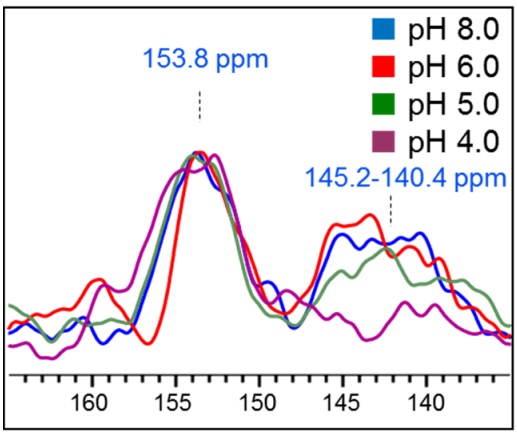

Figure 23. pH-induced ^{15}N chemical shift changes of the protonated Schiff base in D116N mutant.
^{15}N CP-MAS spectra of protonated Schiff base of D116N-KR2 at various pH at 268K.

The peak intensity at neutral pH was quite strong in contrast to BR which indicates that the protonated Schiff base has homogeneity with high cross-polarization efficiency from ^{1}H to ^{15}N nuclei. With lowering pH, the intensity decreased significantly. The reason cannot be easily described, but there are possibilities of inhomogeneity in structure of Schiff base, inefficiency of CP due to alteration of ^{1}H networks in the vicinity of Schiff base and/or increase in overall mobility of KR2 molecule.

Assessment of the Tyr218 chemical shift assigned by Dipolar Assisted Rotational Resonance.

Other residues we focused on are Tyr218 and Asp251. Tyr and Asp residues are conserved in some rhodopsins.[231] In order to understand hydrogen bonding status of Tyr218 with Asp251, we analyzed TyrCζ.

In CP-MAS spectrum, region between 150 and 160 ppm shows discrete four peaks of TyrCζ which includes all 15 Tyr in KR2 (Figure 24(a)). ^{13}Cζ of Tyr is a good probe for understanding its hydrogen bond strength.[211–213,232] It is known that Cζ Tyr signal appears depending on its electron density affected by hydrogen bond formation of adjacent OH. Basically, signals at lower magnetic field indicates stronger bond (Cζ-O-H･･･X). Thus, Tyr in KR2 has roughly four different hydrogen bonding strength at pH 8.0. We additionally obtained DARR spectrum at the same pH and it showed correlation peak of retinal C20 and one Tyr residue at 155.8 ppm. As the closest Tyr to retinal is Tyr218 based on the crystal structure, we assigned this peak as Tyr218 (Figure 24(b)).

This chemical shift value is lower than expected comparing with other microbial rhodopsin such as BR and *Np*SRII which both shows chemical shifts of 158.0 ppm[233] and 157.7 ppm[234], respectively. In BR and *Np*SRII, corresponding Tyr residue (Tyr185 for BR, Tyr174 for *Np*SRII) interacts with nearby Asp residue (Asp212 for BR and Asp201 for *Np*SRII). On the contrary, Tyr without hydrogen bond shows its chemical shift at around 154.4 ppm (estimated as TMS reference), as is the case of ASR which has no corresponding Asp residue and instead has Pro206 which makes it impossible to form hydrogen bond.[148,149] Chemical shift value of KR2-Tyr218 was 155.8 ppm which is in the middle of the chemical shifts mentioned above, showing that Tyr218 forms weak hydrogen bond with Asp251. This result is reasonable as distance between oxygen atoms of Tyr and Asp is 2.74 Å in KR2 (PDB: 3X3C) whereas 2.57 Å in BR (PDB: 1C3W). Corresponding Asp residue in BR, Asp212, interacts with Tyr185 and Tyr57 whereas Tyr57 in BR is substituted to Leu75 in KR2 resulting in the loss of hydrogen bond with Asp251. Instead, Asp251 interacts with Arg109 (Arg82 in BR) which is locating in close distance. This interaction caused weakened interaction between Asp251 and Tyr218 compared to BR.

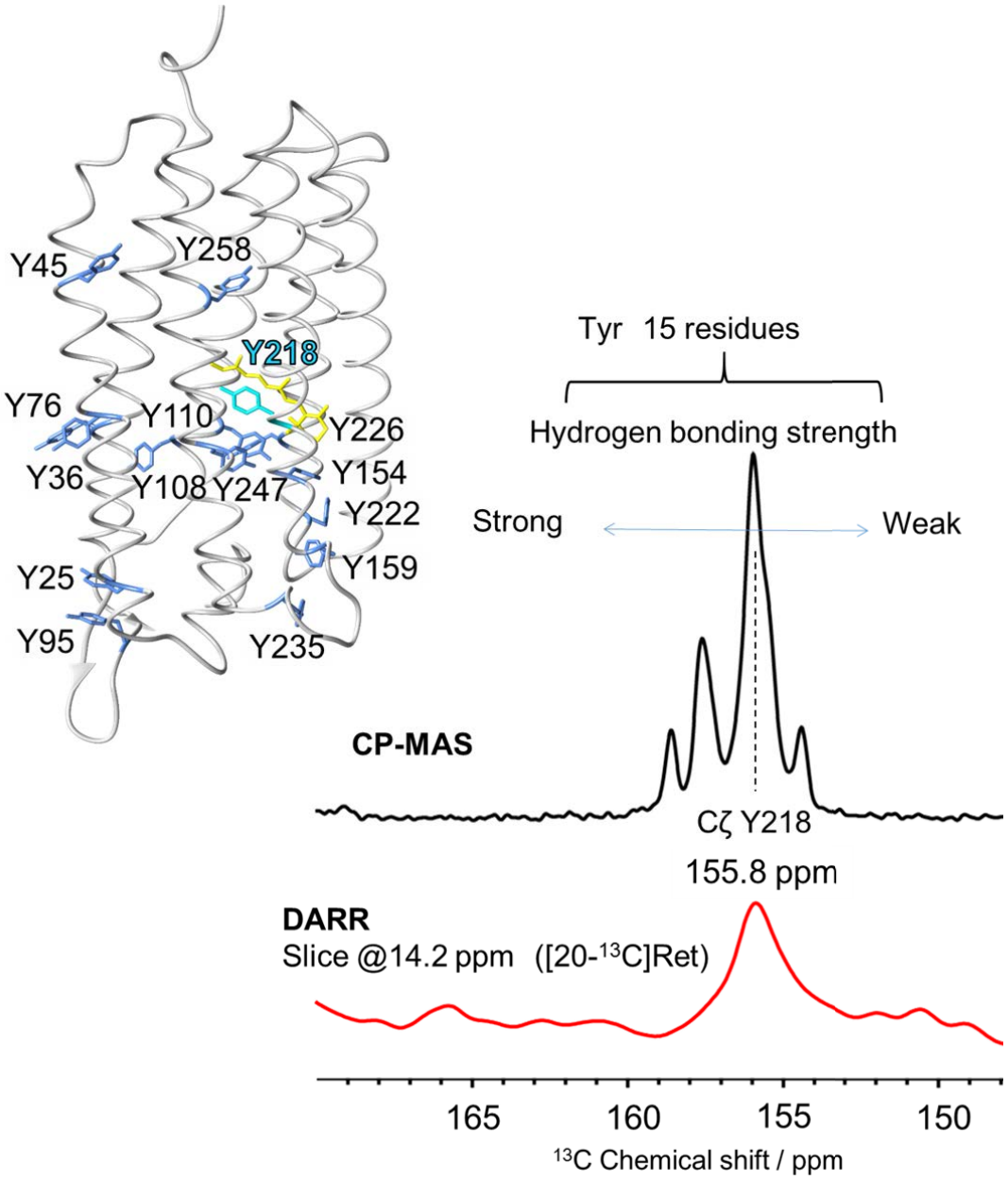

Figure 24. TyrCζ region in ^{13}C CP-MAS and ^{13}C-^{13}C DARR spectra.
^{13}C CP-MAS spectrum (top) and DARR slice spectrum (b) in TyrCζ region. CP-MAS spectrum shows all 15 Tyr signal in four peaks. TyrCζ is sensitive to strength of hydrogen bond. Peak at upper field indicates weaker interaction. DARR spectrum is slice spectrum at 14.2 ppm, showing only Tyr in the vicinity of retinal C20 which is Tyr218. Y-scale of spectrum is expanded.

Characteristic hydrogen bonding strength of Tyr218.

The weak interaction between Asp251 and Tyr218 suggests the flexibility of Asp251 that possibly enables to bind Na^+ ion to Asp251 at O-intermediate.[196] Chemical shift of Tyr218 did not change at neutral and acidic pH, shown in Figure 18(b). This means that Asp251 does not change the protonation state between pH 8.0 and 4.0. This is corresponding to the results of crystallography which showed similar structure of Tyr218 and Asp251 at neutral and acidic pH. Mutational study showed the loss of pumping activity in D251N, thus, importance of negative charge at Asp251. Taking into account of this, Asp251 may be deprotonated at neutral pH and thus at pH 4.0 as well. However, the protonation state is not yet observed directly and needs to be confirmed.

Characteristic feature of sodium ion pump from comparison with other rhodopsins

We showed unique correlation of chemical shift value of Schiff base and maximum absorption wavelength (Figure 21(b)). In addition to BR and *Np*SRII written above, GPR and Channelrhodopsin 2 showed similar plots at the upper side of model compound (520 nm/161.3 ppm for GPR[102,235] and 470 nm/172.8 ppm for ChR2[169]) (estimated as NH_4NO_3 reference). None of them showed plot at the same side as KR2 at ground state. In BR, ground state with acidic condition and K-intermediate showed similar trend in torsion around Schiff base (600 nm/139 ppm and 132 ppm for acid-blue BR[229] and 590nm/145 ppm for K-intermediate[236]), however, we have to emphasize that KR2 showed this torsion with all-*trans* configuration at neutral pH where Schiff base is protonated.

Asp251 residue forms hydrogen bond with Tyr218 which is conserved in many rhodopsins (BR-Tyr185, *Np*SRII-Tyr174, ASR-Tyr179).[88,237,238] Some of these hydrogen bonds are important for the function. In BR, one oxygen atom of Asp212 forms hydrogen bond with Tyr185 whereas another oxygen interacts with Tyr57 and water molecules to form pentagon cluster.[88] The presence of hydrogen bond between Tyr185 and Asp212 stabilizes the formation of pentagon cluster which is important for proton pump. Disruption of this hydrogen bond by replacing Tyr185 to Phe results in decay in proton transfer from Asp85 to proton release group at O-intermediate.[239] For *Np*SRII, Tyr174 has important contribution for the function. Interaction between Tyr174 and Thr204 is essential for the structural change in helices and signal transfer to its cognate transducer *Np*HtrII.[240] There is a possibility that this weak bond is induced by the relatively strong interaction of Asp251 with Arg109 at ground state which plays an important role for sodium ion pumping function.

Conclusion

We investigated the structure of retinal-binding pocket and the pH effect of wild-type KR2 in POPE/POPG lipid membrane by solid-state NMR. DARR experiments allowed to determine chemical shifts of following positions: Retinal C20, Retinal C14, Lys255Cε, Lys255Nζ and Tyr218Cζ. Configuration of retinal was determined as all-*trans*, 15-*anti* at ground state. Schiff base shows tight torsion around N-Cε which is caused by the irregular location of counterion, Asp116. Interaction with Asp116 changed upon pH-change. Tyr218 was revealed to have weak interaction with Asp251 compared to Tyr185-Asp212 in BR. pH change revealed that Asp251 is deprotonated even at pH 4.0. Structure of retinal-binding pocket is unchanged at neutral and acidic pH except for Schiff base and Asp116.

Chemical shifts of retinal C20, C14 and Lys255Cε did not change by acidification. This is corresponding to the case of bacteriorhodopsin showing change in chemical shift of smaller than 1 ppm. Hence, configuration of retinal remains the same as all-*trans*, 15-*anti* at low pH. Retinal chemical shift showed slight change with sample suspended in Tris/CsCl solution, but it was very small. This suggests sodium ion-independent structure of retinal-binding pocket in KR2 at ground state.

Effect of His30 and Na^+-binding site at extracellular side to retinal-binding site of KR2

Introduction

Ion transportation in KR2

Light-driven sodium ion pump, KR2, from marine bacteria, *Krokinobacter eikastus* has been studied to understand its pumping mechanism because of its unmatched model of positively-charged non-proton ion transportation to the previously established models of well-studied archaeal proton-pumping bacteriorhodopsin or chloride-pumping halorhodopsin.[12,183] In addition to being a Na^+ pump, KR2 has additional function of outward light-driven proton pump in the presence of KCl or salts of larger alkali metal ions,[12] thus, KR2 is referred to a dual functional protein.

The selectivity in ion transportation is determined by the ion contained in buffer. Pump activity assay revealed that KR2 pumps sodium ion in NaCl, proton in KCl, RbCl or CsCl, and lithium ion in LiCl.[12] This selectivity is controlled at the ion uptaking pore at cytoplasmic side, which eliminates the entrance of ion larger than Na^+. Mutation at this site to enlarge the pore, N61L/G263F double mutant, allowed to transport cesium ion.[197] Mutation only at uptake site enabled to transport larger ion suggesting that KR2 has transporting ability of any alkali metal ion at retinal-binding site and extracellular side.

Na^+ pump and proton pump in KR2

In the previous chapter, the dual-functionality of KR2 was mentioned. Although the mechanism of Na^+ pump has been studied and that of proton can be supposed from previous studies on proton pumping rhodopsins, the expression mechanism of two distinctive ion transportatios is not understood. Mutational studies revealed the essential residues for Na^+ and proton pump as shown in Figure 25 and Figure 26, respectively. pH increase showing Na^+ pump decreased in some mutants: D116N, D116A, D116E, N112A, D251N, D251A, D251E, and R109A.[12] Most of these mutants lost proton pumping ability which well indicates the importance to the both pumping activities. Some mutants remained proton pumping function, such as D116E and N112A. Na^+ pump requires more complicated mechanism compared to proton pump, thus, this phenomenon of lacking Na^+ pump but existing proton pump can be easily understood.[113] However, in some mutants, such as H30A and

E191Q/E194Q, lost proton pumping activity, but Na^+ pumping activity. For latter mutant, two modified residues are known to be crucial for proton pumping function as a proton release group at extracellular side of the protein, similarly to Glu194 and Glu204 in bacteriorhodopsin.[88] Nevertheless, the reason of lacking proton pump in H30A remains unclear as His30 locates at the molecular interface.

The mutation of H30A induces the loss of its proton pump function although the replacement of His30 by Ala, Lys or Leu also induces the decrease in its sodium ion pumping efficiency.[12,241] His30 forms hydrogen bond with Tyr154 with nearby protomer as revealed by crystallography and functions as one of the factor forming pentamer although the conformation of these residues and creation of interaction depend on the methodological condition (Figure 27).[195,241]

The selectivity of Na^+ and proton pump depends on the concentration of both ions, however, the distinction of two mechanisms remains unclear. The kinetics of both pump activity from the time

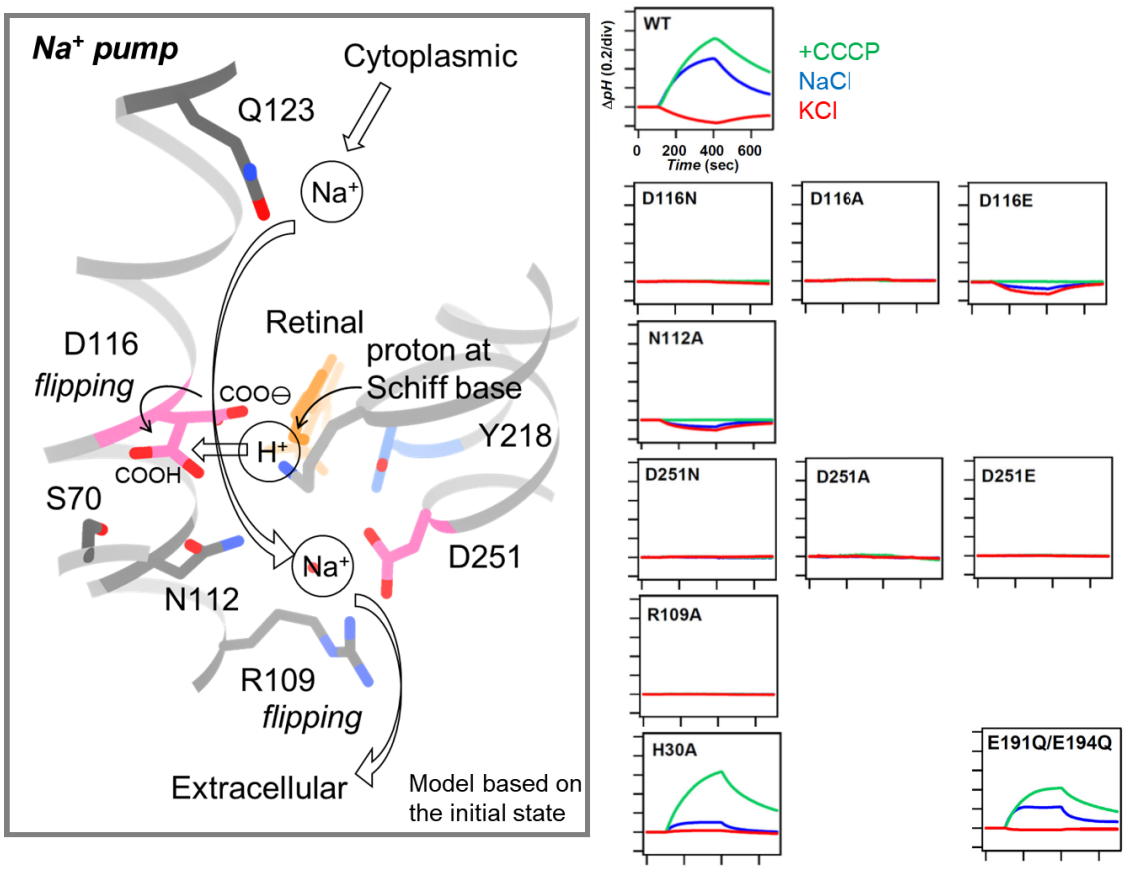

Figure 25. Na^+ translocation pathway around retinal-binding pocket and essential residues.
(Left) Na^+ translocation pathway. Structure is based on the initial structure (PDB code: 3X3C). Oxygen and nitrogen are shown in red and blue, respectively. Red circle represents water molecule. (Right) Pump assay of mutants [12].

constant of the M decay indicated the competitive pump activity at M-intermediate.[193] The photoreaction pathway until M-intermediate seems to be shared based on the flash-photolysis data. This corresponds to the light-induced differences of FTIR results at 77 K which revealed the were identical between the two states of KR2 functioning as light-driven Na^+ and proton pump.[201] The knowledge on the selectivity of transported ion in dual-functional protein is limited because of the small number of rhodopsin proteins with various functions. Channelrhodopsin transport Na^+, K^+, Ca^{2+} and proton and proton permeation is much higher than other ions with same concentration; however, under the physiological environment that of Na^+ and proton becomes similar because of those concentrations.[8,242] Recently found *Synechocystis* halorhodopsin (*Sy*HR) is known to pump SO_4^{2-} and Cl^- as well as Br^- depending on its concentration but its ion selectivity mechanism needs more verification.[243] The selective alkali metal ion transportation has been demonstrated previously; nevertheless, the mechanistic understanding of the selectivity of Na^+ and proton in KR2 remains unclarified.

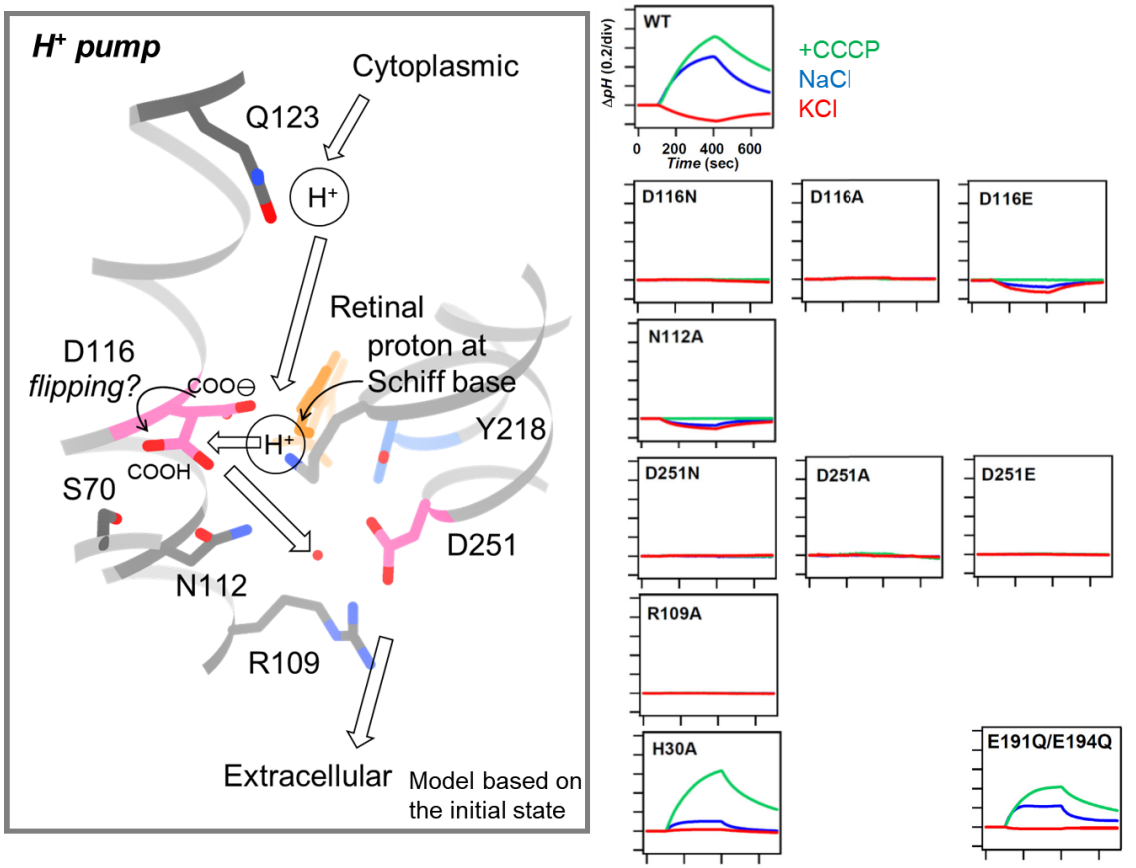

Figure 26. H^+ translocation pathway around retinal-binding pocket and essential residues.
(Left) H^+ translocation pathway. Structure is based on the initial structure (PDB code: 3X3C). Oxygen and nitrogen are shown in red and blue, respectively. Red circle represents water molecule. (Right) Pump assay of mutants [12].

Na^+-binding site and its importance

The ion in buffer affects the selectivity of the ion transported as well as the alteration of bound ion at extracellular Na^+ binding site. A Na^+ binding site at extracellular side is one of the characteristic features of KR2 which is characterized by the crystal structure reported by Gushchin et al. revealing the structure of sodium ion binding site at extracellular side of KR2.[195] Two of three crystal structures shown by Gushchin et al. were pentarmeric precipitated under the condition of pH 5.6, 0.525 M sodium malonate and 3% (w/v) polyethylene glycol (PEG) 6000 (Qiagen) (PDB entry code: 4XTO), and pH 4.9, 0.525 M sodium malonate (Qiagen) (PDB entry code: 4XTN) whereas one structure under pH 4.3, 0.525 M sodium malonate was monomeric (PDB entry code: 4XTL).

Pentameric structure revealed that sodium ion locating between two monomers connects monomers to form homo pentamer. Sodium ion is stabilized by Asp102 side chain from one protomer (bond distance ~2.5 Å) and Tyr25 side chain, Thr87, backbone oxygen of Phe86 and Thr83 from the other protomer (bond distances 2.3–2.4 Å) and a water molecule (bond distance ~2.3 Å) and forms six-coordinated structure. From these bond lengths, the bound ion was determined as a sodium ion. In the monomeric structure shown by Kato et al. did not show any Na^+-binding site,[183] however, monomeric structure Gushchin et al. reported revealed the case of sodium ion forming an octahedrally coordinated structure occupied with water molecules instead of Asp102 side chain. Attenuated Total Reflection (ATR)-FTIR data allowed the signal assignment of Tyr25 and showed that direct interaction between Tyr25 and Asp102 is essential for the protein's stability.[244]

Although the pathway of translocating ion is in line according to the mutational experiments,[12] sodium ion binding to the extracellular side at ground state is thought to be not prerequisite for sodium ion pumping. This is because both KR2 and GLR, another light-driven sodium ion pump, uptake ion during photocycle.[12,185] Therefore, sodium ion bound in the ground-state structure is not being transported.

Dissociation constant was calculated from the signal intensity of ATR-FTIR at various ion concentration.[12] Under 0.5 mM NaCl/KCl absorbance difference is almost zero, but increases the intensity upon exchange to higher concentration indicating the structural difference is increasing in the region of 1800-1000 cm^{-1}. Salt concentration dependence was plotted by taking the peak height at 1553 cm^{-1} and 1567 cm^{-1} to show that association constant of Na^+ binding to the extracellular site is 11.4 ± 0.8 mM at pH 8.0. At pH 3.6, signal intensity change was small suggesting the Na^+-interacting Asp102 is protonated and thus does not bind Na^+.

ATR-FTIR difference spectra upon exchange of 50 mM NaCl/KCl resembles to the change upon exchange of NaCl/RbCl and CsCl, although the signal intensity increased under latter two conditions. However, these data does not clearly prove that potassium ion or larger ions are not bound to the binding site.[12]

Ions contained in buffer and some residues close to the Na^+ binding site at extracellular side

avoid the denaturation of protein.[183] Thermostability assays of detergent-solubilized WT-KR2 showed protein endure longer under Na^+ buffer than in Rb^+ containing buffer. D102N mutant eliminating the Na^+ binding to the binding site at extracellular side, exhibited similar denaturation speed as in Rb^+ buffer. Additionally, N-helix, characteristic feature among NaR and only in some rare rhodopsins, builds interactions between one of the residues in N-helix, Glu11, and Glu160 at DE-loop and Arg243 in G helix and when mutations introduced to each residues showed fast decay of absorbance. These data revealed key residues to stabilize the protein structure are hidden at extracellular side and so is the ions bound to binding site. Pumping assay of these mutants showed the reduced but still functional activity, except for the mutant without complete N-helix, $KR2_{\Delta 1\text{-}18}$, showing no pumping activity, therefore, these residues are essential for structure stability and the solid structure keeps pumping efficiency to the highest level as WT.

Ion effect on pumping function

As KR2 pumps both Na^+ and H^+, ions in buffer and photocycle are closely related. Exchange of buffer changes the ions bound to Na^+ binding site at extracellular side. Thus, photocycle of ion transportation and selectivity of transporting ion may influenced not only by the ions in buffer but also by the structural difference affected by ion bound to the binding site.

Photocycle of reconstituted KR2 in 100 mM NaCl at pH 8.0 is as described in previous chapter 2. In contrast to Na^+ pumping photocycle consisting of K-, L⇄M-, O-intermediates with their time constants of 26 ± 3 μs, 1.0 ± 0.1 ms, and 7.9 ± 0.3 ms and 112 ± 13 ms, respectively, H^+ pumping photocycle in 100 mM KCl at pH 8.0 is completely different showing only K-, L-, and L⇄M⇄O-intermediates based on the calculation from transient absorbance change at 525, 420, 472 and 605 nm. Calculated time constant was 1.07 ± 0.05 ms for L-intermediate, 107 ± 4 ms, 580 ± 80 ms, 70 ± 1.0 s for L⇄M⇄O-intermediate.[12] Contradictory, Li^+, smaller ion than Na^+, is transported by KR2 via similar photocycle as sodium ion transportation. Transient absorbance showed three types of intermediates, K-, L⇄M-, O-intermediates with their time constants of 16.0 ± 1.7 μs, 1.20 ± 0.03 ms, 11.1 ± 0.7 ms, and 140 ± 70 ms, respectively.[12] In contrast, transient stimulated Raman spectroscopy showed that photocycle of WT in CsCl-containing buffer shifts the equilibrium to L in the L/M intermediate, like D102N mutant in NaCl.[245] D102N mutant prevents the Na^+ binding at the extracellular binding site, thus, suggesting that Cs^+ is unbound. The ion transportation activity of KR2 was assumed to depend on the alkali metal ion because of the uptake pore size; however, exchanging the buffer ion also induces alteration of the bound ion at the extracellular binding site.

Aim

Extracellular side of KR2 has several unique structure, such as Na^+ binding site and N-helix.

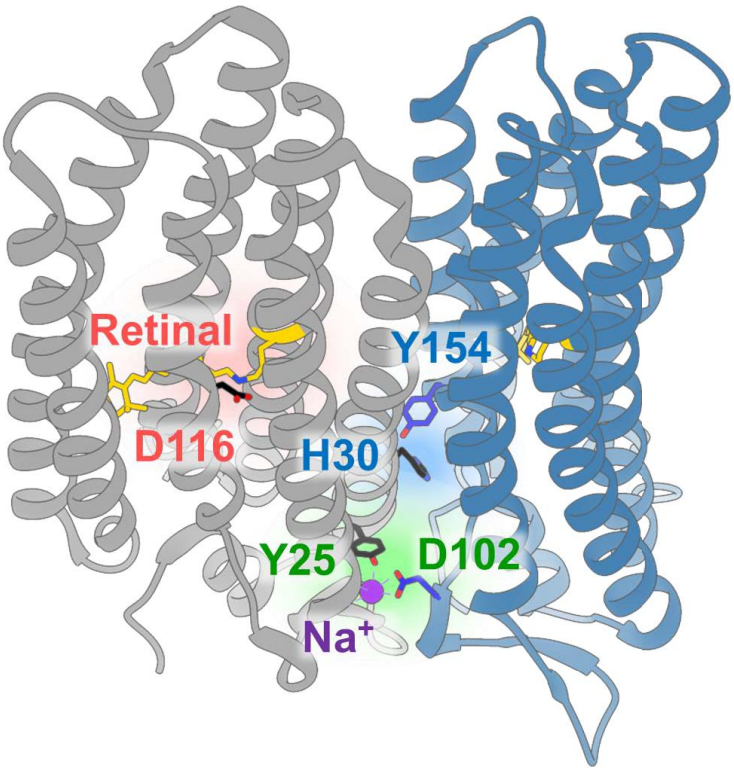

Figure 27. Crystallographic structure of two KR2 protomers.
Two protomers out of five are shown (Protomer 1 in gray and protomer 2 in blue). Retinal-binding pocket region is shown in pink with retinal and Lys255 (yellow) and Asp116 (black). Na^+-binding site is shown in green with Tyr25 (black) from protomer 1 and Asp102 (dark-blue) from protomer 2. His30 of protomer 1 and Tyr154 of protomer 2 is shown in black and dark blue, respectively, in blue region. (PDB code: 4XTO)

These parts build interactions with nearby residues and increases endurance to higher temperature i.e. thermal stability. However, structure of protein outside membrane is rather flexible and may form interactions with nearby but other residues inducing structural change of protein and change interactions near retinal. In order to observe the relationship of structural change at extracellular side, especially Na^+-binding site, and effect on retinal-binding site, we measured the change in retinal-binding site by changing buffer ion (Figure 27).

Materials and Methods

Sample preparation

KR2 with six histidines at the C terminus were expressed in *E. coli* C41(DE3) strain. Expression was done with three steps of culture: 7 hours of start-up culture with 20 mL LB medium

and 1 mL freeze stock of E. coli cells in screw-top test tube with lids, 14 hours of pre-culture with 100 mL M9 medium (Components are shown in Chapter 2) and 21 mL bacterial solution from start-up culture in 500 mL flask with baffles, 20.5 hours of main culture with 2 L M9 medium and 121 mL of bacterial solution from pre-culture in 3 L flask without baffles. Induction was done when O.D. value was at 0.99, which was 5 hours from the start. To obtain [U-^{15}N]WT-KR2, 2.7 mg of [U-^{15}N]NH_4Cl was mixed into M9 media before starting main culture and at the induction point 0.25 g of IPTG, 500 μL of [14, 20-^{13}C]labeled retinal was added. Shaker was set to 170 rpm, 37°C for start-up culture and pre-culture. Main culture was conducted in a water bath with babbling ball (pore size No. 2) and first 7 hours at 37°C and latter 13.5 hours at room temperature. M9 medium for main culture was pre-warmed to 37°C before the start in order to increase the speed of cell proliferation.

The protein was solubilized in 1.7% n-dodecyl-b-D-maltoside (DDM) and purified with Ni-NTA agarose (TALON, Qiagen). Buffer used for washing and elution were followings: For washing, 300 mM NaCl, 25 mM Imidazole, 50 mM MES, 0.05% DDM, pH 6.5 buffer was used. For elution, 300 mM NaCl, 300 mM Imidazole, 50 mM Tris, 0.05% DDM, pH 7.0 buffer was used. Buffer was changed to 50 mM NaCl, 5 mM HEPES, 0.05% DDM, pH 7.0 using Amicon and kept in refrigerator before reconstitution into lipid membrane.

Samples were separately reconstituted into widely used POPE/POPG membranes (3:1 POPE:POPG ratio, 1:20 protein:lipid ratio) for the study of the bacterial membrane proteins as previous work characterizing KR2.[193,217,218] Liposome was prepared with buffer of 200 mM NaCl, 20 mM Tris-H_3PO_4, pH 8.0. Subsequently, each samples were suspended in 10 mM Tris-H_3PO_4 buffer at pH 8.0 with 100 mM LiCl, 100 mM NaCl, 100 mM KCl, 100 mM RbCl, 100 mM CsCl or 0 mM NaCl.

Sample was diluted 10 times with buffer when obtain UV-Vis spectrum for yield calculation. Molecular extinction coefficient of KR2-H30A mutant is 30000 [mol^{-1} · L · cm^{-1}].[12]

Solid-state NMR measurements

Sample suspended with each buffer was packed in a 4.0 mm zirconium sample tube. ^{15}N NMR experiments were then performed at 278 K, and the MAS speed was adjusted to 10.0 kHz on a Bruker Avance III spectrometer operated at 14.1 T (600 MHz as the ^{1}H Larmor frequency) with an E-free probe. ^{1}H-^{15}N cross-polarization contact time was 2.0 ms and Spinal 64 proton decoupling of 80 kHz was employed during acquisition. ^{15}N chemical shifts were referenced to glycine powder at 11.59 ppm (NH_4NO_3 at 0.0 ppm[20]).

UV-Vis measurements

Lipid reconstituted KR2 WT and H30A samples were suspended in 10 mM Tris-H_3PO_4 buffer at pH 8.0 with 100 mM LiCl, 100 mM NaCl, 100 mM KCl, 100 mM RbCl, 100 mM CsCl or 0 mM NaCl. Absorption spectra of each sample were recorded with UV-Vis spectrometer (V650,

JASCO) equipped with an integrating sphere at room temperature.

FTIR measurements

Light-induced FTIR difference spectra at 77 K was performed as described previously.[21] The lipid reconstituted KR2 WT and H30A samples were suspended in 1 mM NaCl or CsCl and 2 mM Tris buffer at pH 8.5. The dried films of 0.1 mg sample were prepared and hydrated with D_2O. Hydrated samples were replaced on a cryostat (Optistat DN, Oxford) coupled to a FTIR spectrometer (FTS-40; Bio-Rad). Samples stabilized at 77 K were illuminated 2 min using 500 ± 10 nm band-pass filter for the formation of $KR2_K$ and also illuminated 1 min using > 600 nm light for photo-reversed to KR2. 128 interferograms were accumulated and 40 repeated recording were averaged.

Flash-photolysis measurements

Transient absorption change of KR2 H30A was measured by nanosecond laser flash photolysis method as previously described.[1] The absorption of POPE/POPG reconstituted sample with a 1:50 protein-to-lipid molar ratio in 100 mM NaCl or CsCl, 20 mM Tris-HCl (pH 8.0) were adjusted to be 0.8-0.9 with 1-cm optical path-length. The sample was photo-excited by a nanosecond pulse of second harmonics (SHG) of Nd^{3+}: YAG laser (λ = 532 nm, INDI40, Spectra-Physics) with an excitation laser power was 3 mJ/(cm^2·pulse). The intensities of the transmitted probe light from a Xe arc lamp (L8004, Hamamatsu Photonics, Shizuoka, Japan) were measured using a multichannel detector (C9125, Hamamatsu Photonics, Shizuoka, Japan) before and after laser excitation, and transient absorption spectra were obtained by calculating the ratio between them. Ninety identical spectra were averaged to obtain higher signal-to-noise ratio.

Results and Discussions

Assignment of ^{15}N signals

Schiff base region of ^{15}N CP-MAS spectra of [U-^{15}N]labeled KR2-WT and [U-^{15}N]KR2-H30A are shown in Figure 29(a) and (b). The peak of Schiff base was previously assigned with [$^{15}N\zeta$]Lys-WT-KR2 (Figure 28).[246] At higher field of Schiff base signal, HisNε signals[247,248] were observed showing two peaks of 140.6 ppm and 144.0 ppm which corresponds to two residues in KR2, His30 and His180. As the signal at 140.6 ppm disappeared in the spectrum of H30A, thus, the other remained peak was assigned as His180. His-tag peaks are broad and hidden in this region as reported in the case of ASR.[148]

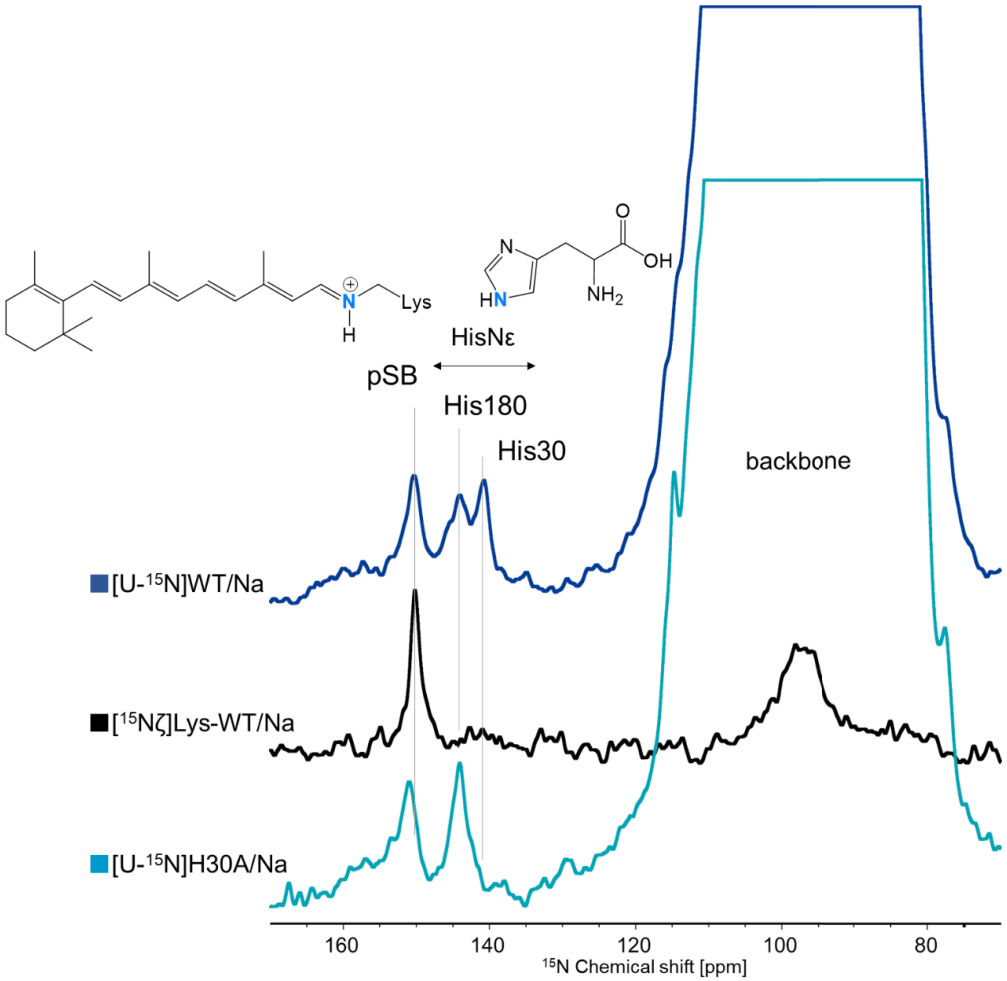

Figure 28. Assignment of Schiff base and His signals.
The peak of Schiff base was previously assigned with [^{15}Nζ]Lys-WT-KR2. At higher field of Schiff base signal, HisNε signals were observed showing two peaks of 140.7 ppm and 144.0 ppm which corresponds to two residues in KR2, His30 and His180. As the signal at 140.7 ppm disappeared in the spectrum of H30A, thus, the other remained peak was assigned as His180.

Ion exchange effect on retinal Schiff base in wild type and H30A mutant

^{15}N chemical shift of protonated Schiff base changed ion-dependently as shown in Figure 29(a) and (b). In NaCl buffer, Schiff base signal appeared at 150.2 ppm as previously reported.[246] As this data was taken under 100 mM NaCl, 10 mM Tris-H_3PO_4 buffer, Na^+ concentration is enough to keep Na^+ bound to the binding-site at extracellular side revealed by concentration-dependent measurement (data not shown). Sharp signal revealed the structure of retinal Schiff base is homogeneous. Under LiCl buffer, Schiff base became twice broader with small shift to 151.3 ppm. By exchanging sample with K^+ containing buffer, peak showed similar chemical shift of 151.7 ppm and broadening as in Li^+. Under RbCl and CsCl buffer condition, signal shifted to 151.7 ppm and 152.4

ppm, respectively, with sharp peak as in NaCl. In the absence of alkali metal ion, similar chemical shift of 152.0 ppm was observed as in RbCl. From these results, chemical shift shows ion-bound state under NaCl and ion-unbound state under RbCl and CsCl and bound/unbound mixture state under KCl. Peak under LiCl was similar to the state under KCl, which indicates the mixed state, however, possibility remains that Li^+ is bound to the binding site and protein packing is fluctuating because

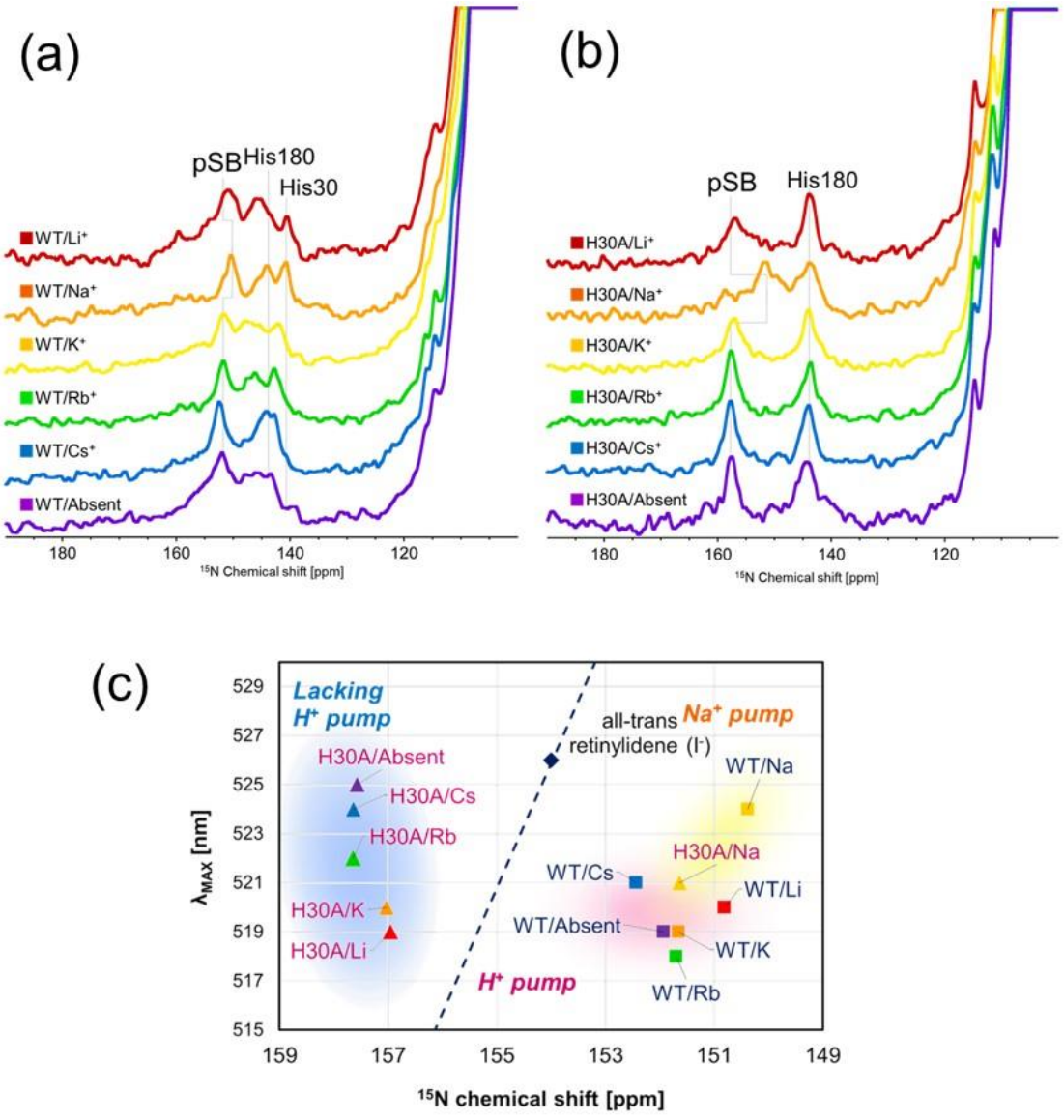

Figure 29. ^{15}N CP-MAS spectra of WT and H30A and correlation with λ_{MAX}.
(a, b) Schiff base and HisNε region is shown. Spectra obtained in 100 mM LiCl (red), NaCl (orange), KCl (yellow), RbCl (green), CsCl (blue), and 0 mM NaCl (purple). (c) Correlation between ^{15}N chemical shift of Schiff base and maximum absorption wavelength.

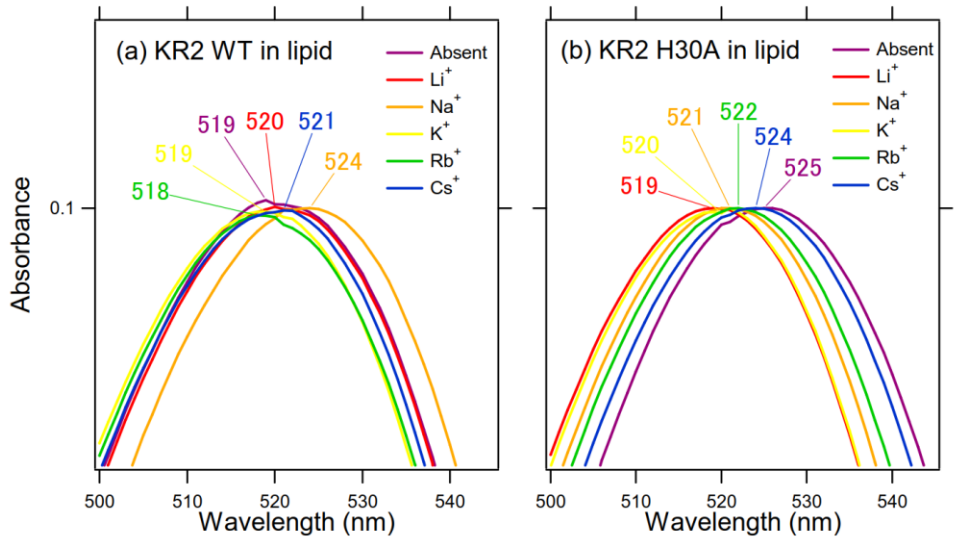

Figure 30. Maximum absorption wavelengths of WT-KR2 and H30A-KR2 in lipid membrane. UV-Vis absorption spectra of lipid reconstituted WT-KR2 and H30A-KR2 in 100 mM each cations or no salt conditions.

---

binding site is forced to fit to smaller ion.

Same conditions were applied to H30A mutant and obtained chemical shifts as following: 157.0 ppm (Li^+), 151.2 ppm (Na^+), 156.8 ppm (K^+), 157.7 ppm (Rb^+), 157.7 ppm (Cs^+), 157.6 ppm (Absent). Although signal of Na^+-bound state showed similar chemical shift, however, the peaks under other conditions shifted widely to lower field. The signal of H30A under Li^+ and K^+ is close to the chemical shift of unbound state than WT indicating the difference in ratio of bound and unbound states suggesting the His30 also functions as a structure holder of binding site at extracellular side.

His signals showed some change under ion exchanged conditions. Signal of His30 in WT changed from high field to lower field by buffer change to larger alkali metal ion showing different pattern as Schiff base change. Although changes in His30 seems to be dependent to ion size or bound/unbound state, however, changes in His180, the residue at outside of the pentamer circle, is not systematic.

Functional effect of ion exchange to wild type and H30A mutant

The ^{15}N chemical shift of protonated Schiff base is determined mainly by two factors: Electrostatic interaction of protonated Schiff base-counterion and torsion around C15=N or N-Cε.[46,104,235,249,250] Figure 31 shows the electrostatic interaction of positively-charged protonated Schiff base and negatively-charged counterion. Chemical shift of Schiff base and counter anion size have linear correlation obtained from all-*trans* retinylidene model compounds.[46] From the obtained

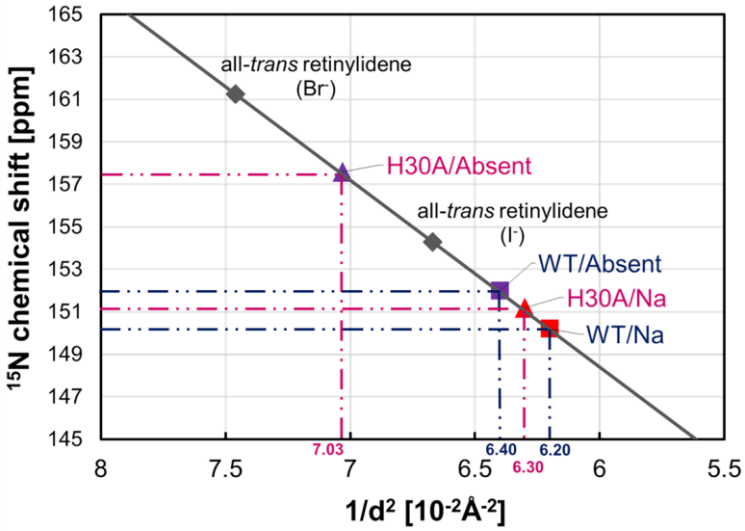

Figure 31. Correlation of the ^{15}N chemical shifts of the protonated all-*trans* retinylidene-butyl-^{15}N-imides (Br^-, I^-) versus the inverse of the center-to-center distance squared ($1/d^2$) of the crystallographic radii of N^{3-} and the halide counterion.
From the obtained chemical shift of Schiff base, distance between positive charge at Schiff base and negative charge counterion was estimated.[46,278]

---

chemical shift of Schiff base we calculated the N-O distance of Schiff base and counterion and obtained the following results: 4.03 Å in WT/Na^+, 3.95 Å in WT/Absent, 3.98 Å in H30A/Na^+ and 3.77 Å in H30A/Absent. This result clearly shows the particular strongering electrostatic interaction of Schiff base and counterion in H30A/Absent. Crystallographic data showed the N-O distance between Schiff base and Asp116 rotormer 2 is 2.5 Å and this difference should be caused by the definition of N-O distance where in crystallography, direct distance of N-O is shown whereas NMR results shows the distance of N and center of negative charge at carboxyl group of Asp116.

Second factor of determining chemical shift, torsion around Schiff base, is shown in Figure 29(c) based on the maximum absorption wavelength (Figure 30). Schiff base chemical shift has correlation with maximum absorption wavelength. Bottom side of linear correlation of all-*trans* retinylidene model compounds, which takes a planar conformation, shows the torsion around N-Cε and upper side of that shows torsion around C15=N according to Hu et al. In spite of small change in torsion around N-Cε in WT/Na^+ and WT/Absent or other ions, H30A showed drastic change from N-Cε torsion in H30A/Na^+ to C15=N torsion in H30A/Absent or other ions.

Schiff base signal change observed by FTIR

Fourier-transform infrared (FTIR) spectra obtained in the conditions of WT/Na^+, WT/Cs^+, H30A/Na^+ and H30A/Cs^+ showed similar frequency value in N-D stretching vibration. Figure 32

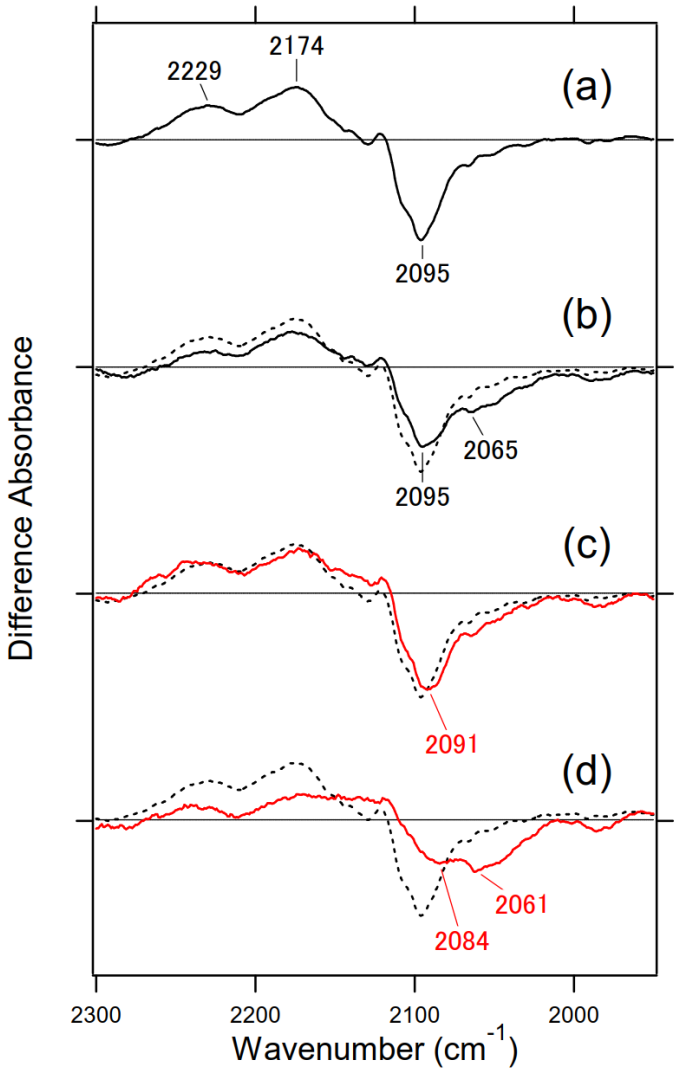

Figure 32. Light-induced FTIR difference spectra of KR2$_K$ minus KR2 of WT and H30A at 77 K. The black solid lines in (a) and (b) represent WT/Na^+ and WT/Cs^+, respectively. The red solid lines in (c) and (d) represent H30A/Na^+ and H30A/Cs^+, respectively. The black dotted lines in (b) – (d) represent WT/Na^+. One division of the y-axis corresponds to 0.0015 absorbance unit.

---

shows negative peak at 2095 cm^{-1} in WT/Na^+ which was assigned to be N-D stretching vibration of Schiff base.[201] This signal resembles those in WT/Cs^+, H30A/Na^+, H30A/Cs^+ and D102N/Na^+ with 2095 cm^{-1}, 2091 cm^{-1}, 2088 cm^{-1} and 2089 cm^{-1}, respectively. In addition to those peaks, peaks with low-frequency was observed in WT/Cs^+. H30A/Cs^+ and D102N/Na^+ with 2065 cm^{-1}, 2061 cm^{-1} and 2062 cm^{-1}, respectively, indicating the existence of second component of N-D stretch with stronger electrostatic interaction.

Ion exchange effect on photocycle of H30A mutant

The structure at ground state with and without sodium ion influenced on the photocycle of H30A mutant as well. Flash-photolysis data revealed similar photocycle in H30A/Na^+ with K-, L/M- and O-intermediates (Figure 33). Buffer exchange to CsCl prevented the circulation of photocycle by forming only small amount of K-intermediate and no M-intermediate (Figure 34).

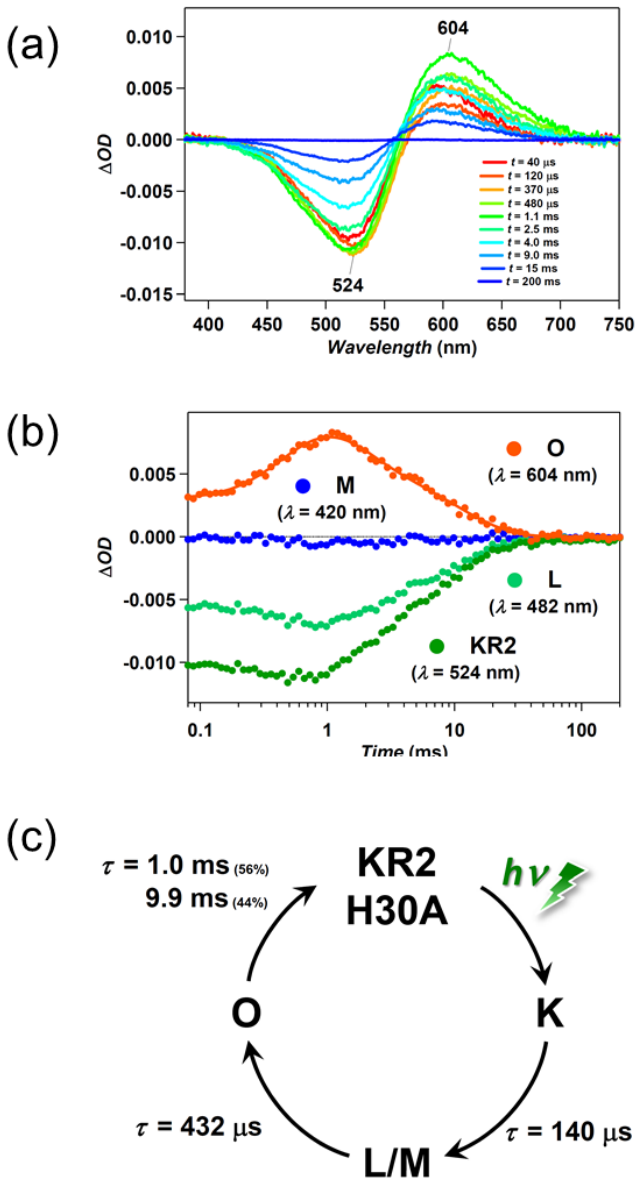

Figure 33. Photocycle of KR2 H30A reconstituted in POPE/POPG and 100 mM NaCl.
Transient absorption spectra of KR2 H30A reconstituted in POPE/POPG liposome (1:50 protein-to-lipid molar ratio) in solution containing 100 mM NaCl and 20 mM Tris-HCl (pH 8.0) (a) and time traces of absorption change (b) at specific probe wavelengths. (c) Photocycle scheme of KR2 H30A in the presence of Na^+ determined from the analysis of the results shown in a, b.

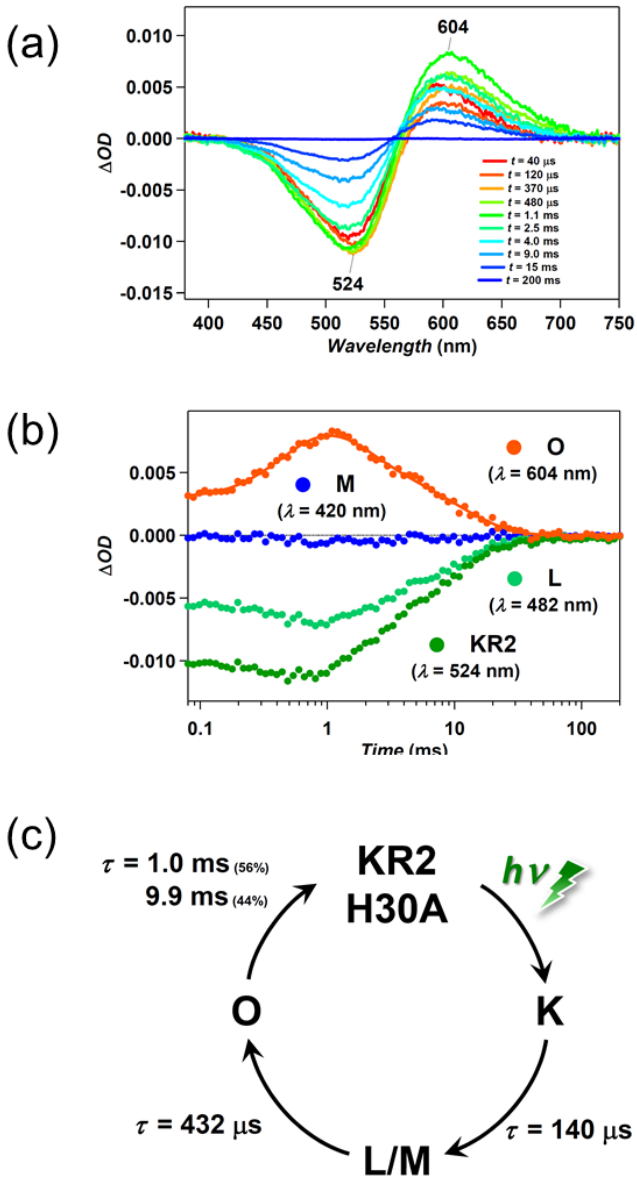

Figure 34. Photocycle of KR2 H30A reconstituted in POPE/POPG and 100 mM CsCl.
Transient absorption spectra of KR2 H30A reconstituted in POPE/POPG liposome (1:50 protein-to-lipid molar ratio) in solution containing 100 mM CsCl and 20 mM Tris-HCl (pH 8.0) (a) and time traces of absorption change (b) at specific probe wavelengths. (c) Photocycle scheme of KR2 H30A in the presence of Cs^+ determined from the analysis of the results shown in a, b.

Discussion

Considering both electrostatic interaction and torsion around Schiff base, reorientation of Schiff base-counterion interaction is occurred in H30A/Absent. In WT/Na^+, protonated Schiff base

holds H-bond with one of oxygen of Asp116COO$^-$ based on the crystallographic data. Relaxation of torsion around Schiff base occurs in the direction that Schiff base proton points out towards extracellular side. In spite of this movement of proton, distance between Schiff base and Asp116 got shortened in H30A/Absent as calculated from ^{15}N chemical shift. N-D stretch from FTIR did not show shift except the appearance of second band with low frequency suggesting second spices with strong electrostatic interaction. To implement these conditions, slight movement of Asp116 to extracellular side should be occurred to follow the torsion of Schiff base proton to form stronger electrostatic interaction. Therefore, we concluded that both oxygen of Asp116COO$^-$ interacts with Schiff base proton electrostatically in H30A/Absent as shown in Fig. 4 instead of hydrogen bonding with one of oxygen of Asp116 in WT/Na$^+$. Here, Schiff base proton interacting with Asp116 is in equilibrium of two states, interacting with one of oxygen of Asp116COO$^-$ and the other which corresponds to the

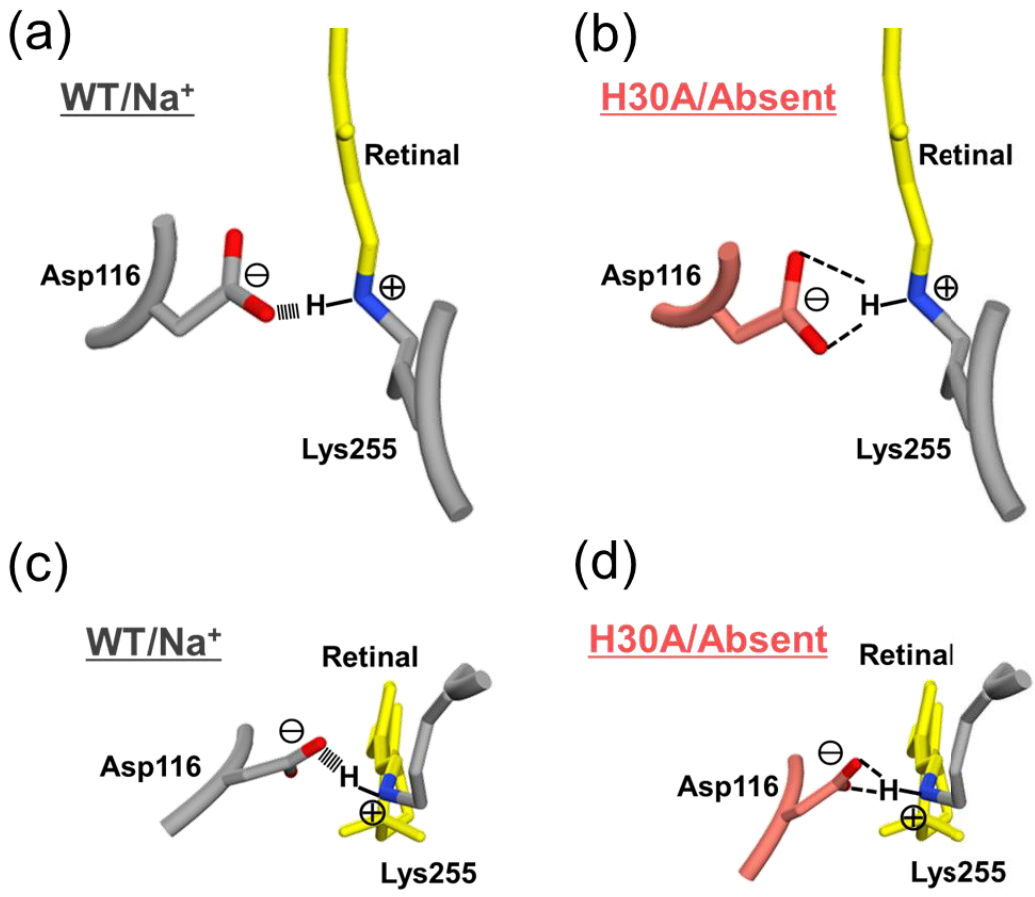

Figure 35. Schematic model of interaction between Schiff base and counterion. (a, c) Interaction revealed by crystallography in WT/Na$^+$. (b, d) Model of interaction in H30A/Absent based on the NMR and FTIR results.

existence of two bands of N-D stretch. Closing of counter-anion to Schiff base induces strong electrostatic interaction as is observed in NMR which well corresponds to the appearance of low-frequency band in FTIR. The distance of Schiff base-counterion in WT/Absent and H30A/Na^+ is rather close to that in WT/Na^+, thus, conformation of these should be similar to WT/Na^+-like but slightly close to H30A/Absent. Non-cyclic photocycle of H30A/Absent also supports that the re-isomerization of retinal and proton pass from Schiff base to counterion does not occur in H30A/Cs^+ because strong interaction locks retinal isomerization and protonation.

The side chain movement of Asp116 should be induced by the absence of ion binding at extracellular and His30 resulting in the sliding of helix C to the extracellular side (or tilt). Therefore, existence of His30 and sodium ion binding to extracellular side is essential for proton pumping function.

In addition to retinal Schiff base, residues locating at extracellular half of the protein showed conformational change in KR2 as was observed in NMR data which supports the displacement of helix C. Signal changes in ArgNδ and ArgNε in R109K mutant compared to WT and H30A (data not shown) suggests the disruption of hydrogen bonds of Arg109 formed with Asp251 and water molecules. Structural differences between monomeric and pentameric states were reported to show the extracellular region of helix C, possibly caused by the ion bound state.[195,245] Indeed, long-distance perturbation was reported in proteorhodopsin where the pK_a increase of Schiff base was induced by the mutation at intracellular side, A178R, probably caused by the alteration of hydrogen-bonding network.[251] Therefore, existence of His30 and Na^+ binding to extracellular side hold protein structure to appropriate form for proton pumping function.

Conclusion

In this study, lack of proton pump ability in H30A mutant was discussed from the observation of Schiff base-counterion by solid-state NMR, FTIR and flash-photolysis measurements. By NMR, larger shift in ^{15}N chemical shift of protonated Schiff base in H30A was observed under K^+ or larger alkali metal ion than in WT indicating the stronging interaction between Schiff base and counterion and torsion around Schiff base. FTIR observation revealed that Schiff base-counterion interaction has similar N-D stretching vibration at any conditions but appearance of second peak under Cs^+ indicates stronger interaction. Strong electrostatic interaction with counterion and torsion around Schiff base induced by absence of His30 and bound ion at extracellular binding site precluded the re-isomerization of retinal and proton transfer to counterion which corresponds to the result from flash-photolysis showing less formation of K-intermediate. The long distance perturbation of existence of His30 and bound ion to binding site to Schiff base revealed the crucial structure for pumping function.

Observation of photo-intermediates of *Hs*BR by photo-irradiation solid-state NMR

Introduction

Bacteriorhodopsin

Bacteriorhodopsin is a H^+ pumping rhodopsin protein found in the purple membrane in an archaea, *Halobacterium salinarum*, where it generates a proton gradient across the cytoplasmic membrane for ATP synthesis.[16,252] Among seven transmembrane helices, retinal chromophore is covalently bound to the Lys216 in helix G. An extensive three-dimensional hydrogen-bonded network of residues and seven water molecules at extracellular side connects the buried retinal Schiff base and its counterion Asp85 to the membrane surface for its proton pump function.[21] The light energy induces the isomerization of the retinal, which structural change propagates the conformational changes in the protein, including a change in the tilt of helix E and F. Protonation of Asp85 initiates a cascade of atomic displacements in the extracellular region that causes the release of a proton to the surface.[24] Structural change in the protein allows the proton transfer by the stepwise changes in pK_a of charged residues, including Asp85, Asp96, Glu194, and Glu204.[40]

Photocycle starting from 13-*cis*, 15-*syn* retinal

Photocycle of Bacteriorhodosin for proton pump consists of several photo-intermediates with retinal isomerization. Retinal conformation changes from 13-*cis*, 15-*syn* (CS; BR_{548}) to all-*trans* (13-*trans*,15-*anti*) (AT; BR_{568}) with light irradiation followed by changes to several intermediates, K, L, M, N and O and then back to all-*trans*, ground state.[40,84,253] These pathways starting from all-*trans* called all-*trans* photocycle (AT photocycle) which is a main photocycle for proton pump. The detailed information on the BR photocycle was mentioned in Chapter 1.

In contrast, the photocycle of the CS state (CS photocycle) has not been extensively studied. In previous studies,[94,95,254,255] pulsed Nd laser experiment conducted to find out the existence of intermediate which has maximum absorbance at 610 nm with the half-life of ~40 ms. As the same intermediate was not detected in the AT photocycle, it was determined to be an intermediate of the CS state and assigned as *batho*-13-*cis*-BR^9 or "610"-intermediate.[94] However, information on this photocycle is limited and needs to be clarified. Photocycle in *Anabaena* Sensory Rhodopsin is also

known to have 13-*cis* photocycle.[158]

Y185F mutant

Y185F mutant in known to have two conformations of retinal at CS : AT molar ratio of 3 : 1 in the dark-adapted state.[256,257] Light-adaptation to Y185F mutant produces O-like intermediate.[258,259] Photo-irradiation at 170 and 250 K to O-intermediate in Y185F mutant produces N-intermediate, while no M-intermediate was detected.[260,261] As Tyr185 is hydrogen bonded to the hydrogen bond network relating to the proton transfer from Asp85 to a PRG through Asp212.[262] Breakdown of the hydrogen bond network prevents H^+ transport, it is, therefore, predicted that the half-life of the O-intermediate would be significantly increased.[263]

Observation of photo-intermediates by NMR

Photo-intermediates are normally detected using flash photolysis with pulsed laser light and by dividing the continuous structural change based on the wavelength of the absorbance maximum i.e. retinal structure. Solid-state NMR spectroscopy represents a powerful alternative tool for detecting intermediates during the photocycle. In previous report, the L-, M-, and N-intermediates have been detected by measuring ^{13}C NMR signals of [^{13}C]retinals as well as ^{15}N NMR signals of [ζ-^{15}N]Lys-BR.[46,264] The 13-*cis* and 13-*trans* forms of [20-^{13}C]retinal and the 15-*syn* and 15-*anti* form of [14-^{13}C]retinal can be distinguished based on the γ-position effects.[68,163,265,266]

In situ photo-irradiation NMR spectroscopy recently characterized the photo-intermediates of sensory rhodopsin I and sensory rhodopsin II (or phoborhodopsin). Multiple M-intermediates were identified in the SRII system using this approach.[179] In addition, identification of the photo-intermediates such as the M- and P-intermediates of *Sr*SRI were successful at which intermediates demonstrate negative and positive phototaxis, respectively.[178] Thus, this technique should be well suited for the investigation of common archaebacterial photocycle systems, such as BR.

Aim

In this study, we focused on the detection of BR photo-intermediates in the photocycle starting from 13-*cis* retinal as well as the all-*trans* photocycle, and the retinal conformation at each intermediates. The photo-cycle of the 13-*cis* was first investigated with wild type BR and then with Y185F mutant as a large proportion of 13-*cis* state exists in dark-adapted state than in WT. Additionally, the photo-trapped intermediates of all-*trans* photocycle allowed the N-intermediate in WT and M, N- and O-intermediates in Y185F from the comparison of temperature controlled dark and light-irradiating condition. Understandings on 13-*cis* photocycle and other photo-intermediates in all-*trans* photocyle allows to gain insights into the characteristics and structure of proton pumping bacteriorhodopsin.

Materials and Methods

Sample preparation

Culture, harvest and purification

In order to culture *H. salinarum*, three steps of culture are applied. First of all, 10 mL of natural peptone medium is poured into 30 mL conical flask and covered the neck with aluminum foil and autoclaved. All operation was done under sterilization as followed. After autoclaved, put 0.5 mL freeze stock of *H. salinarum* S-9 strain and incubated for three days with condition of 170 rpm and 37°C (Start-up culture). Transfer 10 mL of fungus liquid to larger scale of 50 mL flask with 20 mL natural peptone medium and incubated for four days (Pre-culture). Afterwards, half of this medium with bacteria was inoculated into 200 mL synthetic media in 500 mL flask at 110 rpm, 37°C under light-irradiation for seven to ten days until its absorbance reaches to 1.1 (Main culture). In the case of labeling, labled amino acids were used for synthetic media. E1001 mutant was used to label retinal since this does not produce retinal and labeling place can be controlled by adding specific labeled retinal when OD value is 0.5, 0.7 and 0.9 which usually are third, fifth and sixth days. It has some sequence as wild type. Although start-up culture and pre-culture were done under dark condition and main culture with light. This difference is because of increasing in the amount of bacteria under dark condition and increasing the production of purple membrane under light.

To harvest, fungus liquid was pelleted by centrifuge at 4500 rpm for 40 mins at 4°C. Pour out the supernatant, pour about 80 mL of basal salt and suspended with glass rods. Centrifuge was applied again with same condition and put the supernatant out. In order to shatter bacterium body, cold diluted water was added and mixed. Poured this solution to beaker, put two spoonfuls of Deoxiribonuclease I with spatula and stirred for about two hours at 4°C. When it got homogeneous, transferred to dialysis tube and dialyzed overnight in a MilliQ water. Then centrifuge was applied at 1800 rpm for 90 mins. Put the supernatant out and resuspended with 15 mL of HEPES buffer. At this point, resuspend only purple membrane and not the other gray pellet which is heavier and can be seen on the bottom of pellet of purple membrane. Applied centrifuge several times to get rid of gray pellet thoroughly and resuspended with HEPES buffer and stored in a fridge.

Freeze stock was made at the stage of pre-culture. Filter the 50% of Glycerol solution to sterilize and mix 500 μL of fungus liquid from pre-culture with the same volume of Glycerol solution. Mix thoroughly with pipetting and store in a freezer at -80°C.

NMR sample was prepared by changing buffer from HEPES to buffer for NMR measurement. Centrifuge was applied with condition of 18000×g, 90 mins several times to change buffer fully.

Media protocols

Here are media and buffer protocols used for any BR-mutants culture and purification. These

protocols are based on Oesterhelt et al. report.[20]

Table 5. Buffer solutions

Basal Salt (pH 7.4, 500 mL scale)	
NaCl	125 g
KCl	1 g
$MgSO_4 \cdot 7H_2O$	10 g
$CaCl_2 \cdot 2H_2O$	0.1 g
Trisodium Citrate $\cdot 2H_2O$	1.5 g
HEPES buffer(pH 7.0, 500 mL scale)	
NaN_3	0.125 g
HEPES	1.2 g
Buffer for NMR measurement (pH 7.0, 500 mL scale)	
NaN_3	0.125 g
HEPES	0.6 g
NaCl	0.3 g

Table 6. Natural peptone medium (pH 7.4, 1 L scale)

NaCl	250 g
KCl	2 g
$MgSO_4 \cdot 7H_2O$	20 g
$CaCl_2 \cdot 2H_2O$	200 mg
Trisodium Citrate $\cdot 2H_2O$	3 g
OXOID Bacteriological Peptone (Code L37)	10 g
Metal solution stock for peptone medium	1 mL
Metal solution stock for peptone medium 100 mL (0.1 N HCl)	
$ZnSO_4 \cdot 7H_2O$	65 mg
$MnSO_4 \cdot H_2O$	20 mg
$FeCl_2 \cdot 4H_2O$	27 mg
$CuSO_4 \cdot 5H_2O$	7.5 mg

Table 7. Synthetic medium (pH 6.6, 2 L scale)

NaCl	500 g
$MgSO_4 \cdot 7H_2O$	40 g
KCl	2 g
KNO_3	200 mg
KH_2PO_4	300 mg
K_2HPO_4	300 mg
Trisodium Citrate $\cdot 2H_2O$	1 g
Glycerol	1 g
Metal solution stock for synthetic medium	2 mL
L-Ala	430 mg
L-Cys	100 mg
L-His	300 mg
L-Lys	1700 mg
L-Pro	**100 mg**
L-Tyr	**400 mg**
L-Arg	800 mg
L-Glu	2600 mg
L-Ile	440 mg
L-Met	370 mg
L-Ser	610 mg
L-Trp	50 mg
L-Asp	450 mg
Gly	120 mg
L-Leu	1600 mg
L-Phe	260 mg
L-Thr	500 mg
L-Val	1000 mg
<u>Metal solution stock for synthetic medium 100 mL (0.1 N HCl)</u>	
$CaCl_2 \cdot 2H_2O$	700 mg
$CuSO_4 \cdot 5H_2O$	5 mg
$FeCl_2 \cdot 4H_2O$	230 mg
$ZnSO_4 \cdot 7H_2O$	44 mg
$MnSO_4 \cdot H_2O$	30 mg

Sample preparation for NMR measurements

Halobacterium salinarum S9 (E1001) was grown in a temporary medium containing [20,15-^{13}C]retinal, [1-^{13}C]Tyr, [^{15}N]Pro and [ζ-^{15}N]Lys to yield selectively labeled [20,15-^{13}C]retinal-, [1-^{13}C]Tyr-, [^{15}N]Pro-, and [ζ-^{15}N]Lys-WT-BR in the PM. The PM was then isolated according to a previously reported method.[267] *Halobacterium salinarum* S9 (Y185F-BR) was grown in a temporary medium containing [1-^{13}C]Tyr, [^{15}N]Trp and [ζ-^{15}N]Lys to yield selectively labeled [1-^{13}C]Tyr-, [^{15}N]Trp-, and [ζ-^{15}N]Lys-Y185F-BR in the PM. The PM was then isolated according to a previously reported method.[267] Isotopically labeled bacterioopsins (Y185F-BOs) were prepared by photo-bleaching of the corresponding Y185F-BR in 500 mM hydroxylamine solution (pH adjusted to pH 7.0) at 4°C. Isotopically labeled regenerated Y185F-BR was obtained by the addition of [20,14-^{13}C] retinal or [20,15-^{13}C]retinal to Y185F-BOs obtained from bleached Y185F-BR in a process termed *in vitro* retinal reconstitution.[268] Retinal bleaching and reconstitution were confirmed by measuring the absorbance of BR. Samples were then suspended in a 5 mM N-(2-hydroxyethyl)piperazine-N'-2-ethane sulfonic acid (HEPES) buffer with 10 mM NaCl at pH 7.0. For NMR measurements, 5 mM Tris buffer with 300 mM NaCl at pH 9.0 was used.

Sample was diluted 10 times with buffer when obtain UV-Vis spectrum for yield calculation. Maximum absorbance of BR appears at around 568 nm. Molecular weight of bacteriorhodopsin is about 26000 [-][219] and molecular extinction coefficient is 63000 [mol^{-1} · L · cm^{-1}][269].

Solid-state NMR measurements

Pellet was put into NMR sample tube which is 5 mmφ made of ZrO_2, capped with glass cap and then enclosed with Araldite. CMX infinity-400 FT-NMR spectroscopy by Chemagnetics is used for *in-situ* photoirradiation solid-state NMR measurement. For external reference, [1-^{13}C]Gly is used as standard material and set as 176.03 ppm. In order to measure change in both retinal and protein side, CP-MAS measurement were conducted with [1-^{13}C]Tyr-, [^{15}N]Pro-, [15,20-^{13}C]Retinal-labeled WT-BR sample. Light irradiation condition for observing change in trapped intermediates was as follows: Dark(D1)→Light(L1)→Dark(D2)→Light(L2). The MAS speed was set at 4 kHz.

These experiments are done at 20°C and -20°C for WT and 20°C, 0°C, -20°C and -40°C for Y185F mutant. For trapping N intermediate, light condition was started from D1 to L2 and then temperature was changed with light on to make sure that intermediates stay inside the AT cycle and do not change back to CS. Measurements were continued in dark and then light as is supposed to be same condition as D2 and L2, repeatedly.

In-situ photoirradiating solid-state NMR is a way to trap intermediates by controlling on/off of LED light from outside of probe. As shown in Figure 9, optical fiber connected to LED source is lead into probe and light goes directly into sample tube through glass cap. Since switch for LED is outside of the probe, light irradiation control can be done without taking sample tube which means

measurements can be done continuously without changing conditions. Light wavelength is changeable among 520 nm, 595 nm and 365 nm by switching light source one to another. Sample was irradiated with 50 mW 520 nm green LED light for WT and 520, 595 or 365 nm LED lights for Y185F.[178] In the NMR measurements, CP pulse sequence was used with a 1 ms contact time, followed by acquisition with a 50 kHz TPPM proton decoupling pulse.[270] Typically 20,000 transients were accumulated for each experiment. To elucidate the stepwise reaction pathways, difference spectra are shown to provide information on reactant and product species as negative and positive peaks, respectively.

Results and Discussions

Results of WT observation

[20-^{13}C]retinal signal observation of photo-trapped intermediates

NMR measurements on retinal C20 and C14 as well as latter shown Tyr carbonyl signal were observed under following conditions: (1) in the dark (D1), which provided a dark-adapted state at both 20°C and −20°C; (2) under illumination with 520 nm LED light (L1), which provided a light-adapted state at 20°C and photo-excited state from D1 at −20°C; (3) in the dark (D2), which provided a relaxation to dark-adapted state at 20°C and a light-adapted state from L1 at −20°C; (4) and then under illumination with 520 nm LED light (L2), which provided a photo-excited state from D2 at both 20°C and −20°C; and (5) in the dark (D3), which provided a light-adapted state from L2 which result is only shown for Y185F mutant. CP-MAS spectra of [20-^{13}C]retinal under 20°C and −20°C is shown in Figure 36 and Figure 37, Figure 38 and Figure 39, respectively. Figure 37 shows the comparison between D1 and L1 at 20°C. D1 was measured after NMR tube was kept in a dark place for > 4 hours. Two peaks were observed at 13.1 ppm and 22.0 ppm which were assigned as all-*trans* and 13-*cis*, 15-*syn* retinal, respectively, based on the previous research. Integrated ratio of both peaks were almost the same which showed two contents exists as 1:1 as reported formerly. Other peaks and backgrounds are mainly the signals of lipids. The broad and several sharp lipid peaks were overlapped each other and that makes integrated ratio of peaks of the retinal peak unprecise. By irradiating light to this dark-adapted state (L1 condition), peak of 13-*cis*, 15-*syn* at 22.0 ppm decreased and peak at 13.1 ppm increased compared to the D1 spectrum. This result indicates that the conformation change from 13-*cis*, 15-*syn* to all-*trans* was occurred at L1. When the light was turned off after L1 condition, shown as D2, peak changed back to the dark-adapted state at 20°C. Half of all-*trans* retinal changed to 13-*cis*, 15-*syn* to the same composition as the initial dark-adapted state at D1.

Result at −20°C was considered to be the same change at 20°C; however, it changed differently (Figure 38 and Figure 39). D1 was recorded as dark-adapted state which turned from 13-*cis*, 15-*syn* to another peak at 19.7 ppm at L1 and all-*trans* peak remained the same. Since chemical

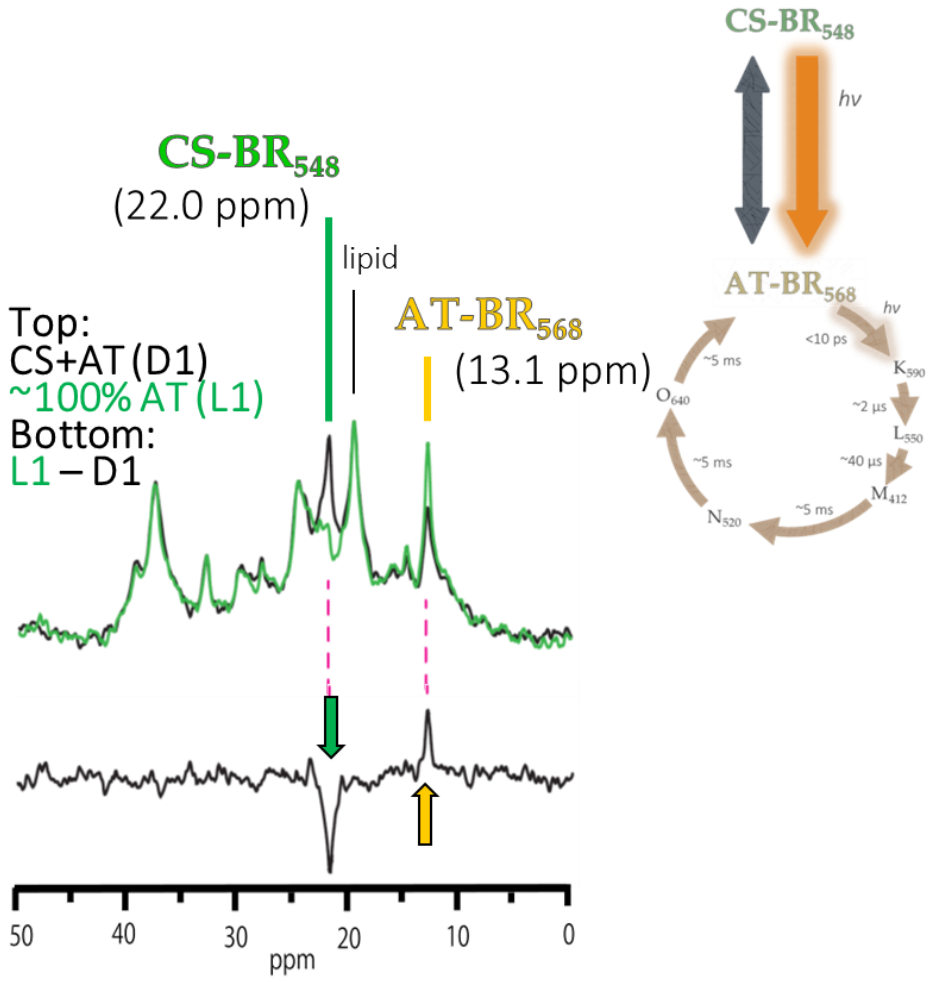

Figure 36. Comparison between CP-MAS spectra of [20-^{13}C]Ret-BR at D1 and L1 at 20°C.
(Left top) Overlapped spectra of D1 and L1. (Left bottom) Difference spectrum of two spectra above. (Right) Pathway highlighted in orange represents the change from D1 to L1.

---

shift of newly appeared peak is close to 13-*cis* conformation, we defined this as a CS*-intermediate. During the measurement of L1, the peak at 19.7 ppm showed slight decrease in its intensity and in contrast the small increase was observed in all-*trans* peak. While L1 measurement, light was continuously irradiated, thus, CS*-intermediate was stationaliry trapped, however, few amount of this intermediate leaked to all-*trans* state. Changing the condition back to dark, D2, CS*-intermediate was transferred to all-*trans* to show the ~100% all-*trans* state, light-adapted state, although light was turned off.

After D2 measurement trapping ~100% all-*trans*, green light was again irradiated to trap photo-intermediates in all-*trans* photocycle. As is shown in Figure 40 , all-*trans* peak decreased and peak at 19.7 ppm increased. This indicates the change from all-*trans* to intermediate in the all-*trans*

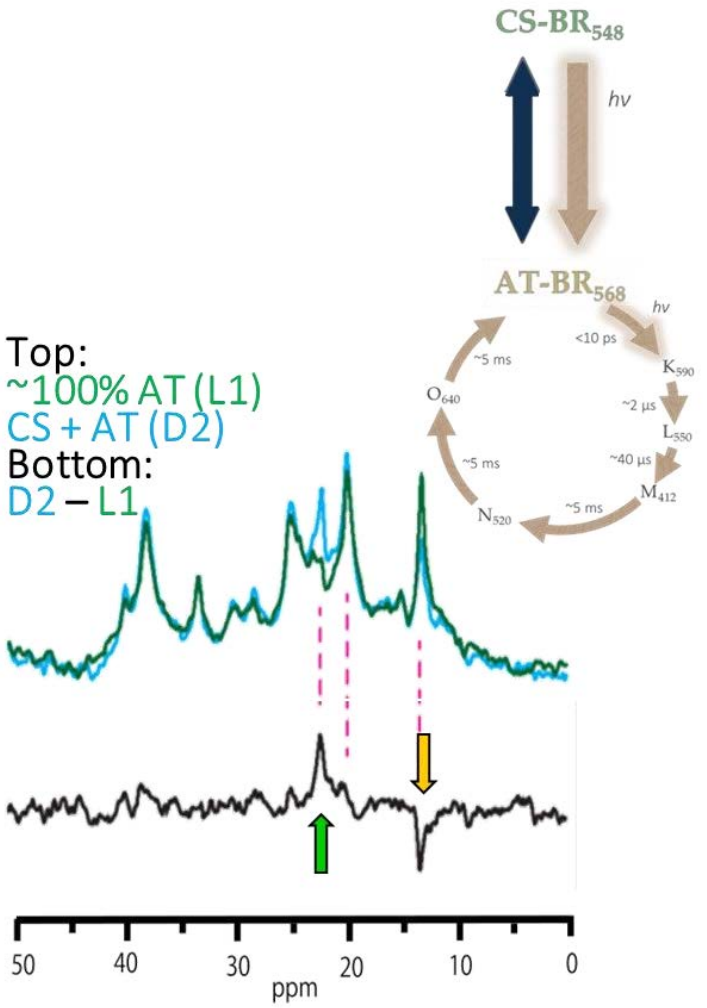

Figure 37. Comparison between CP-MAS spectra of [20-^{13}C]Ret-BR at L1 and D2 at 20°C.
(Left top) Overlapped spectra of D1 and L1. (Left bottom) Difference spectrum of two spectra above. (Right) Pathway highlighted in orange represents the change from L1 to D2.

---

photocycle. According to the report by Hu et al.[271], N-intermediate was easily trapped around -20˚C, therefore, this peak at 19.7 ppm at L2 was determined as N-intermediate. This peak has the same chemical shift as CS*-intermediate, therefore, retinal takes similar conformation as CS*-intermediate probably. The ratio of N intermediate changed depending on temperature. At 20˚C, N intermediate was not trapped, but from −15˚C, it increased the amount of trapped N and it reached almost 85% of whole BR at −35˚C (

Figure 41). The population of N-intermediate increased as the temperature was set lower. Percentage of trapped intermediate is rough estimation from the integration of the peak.

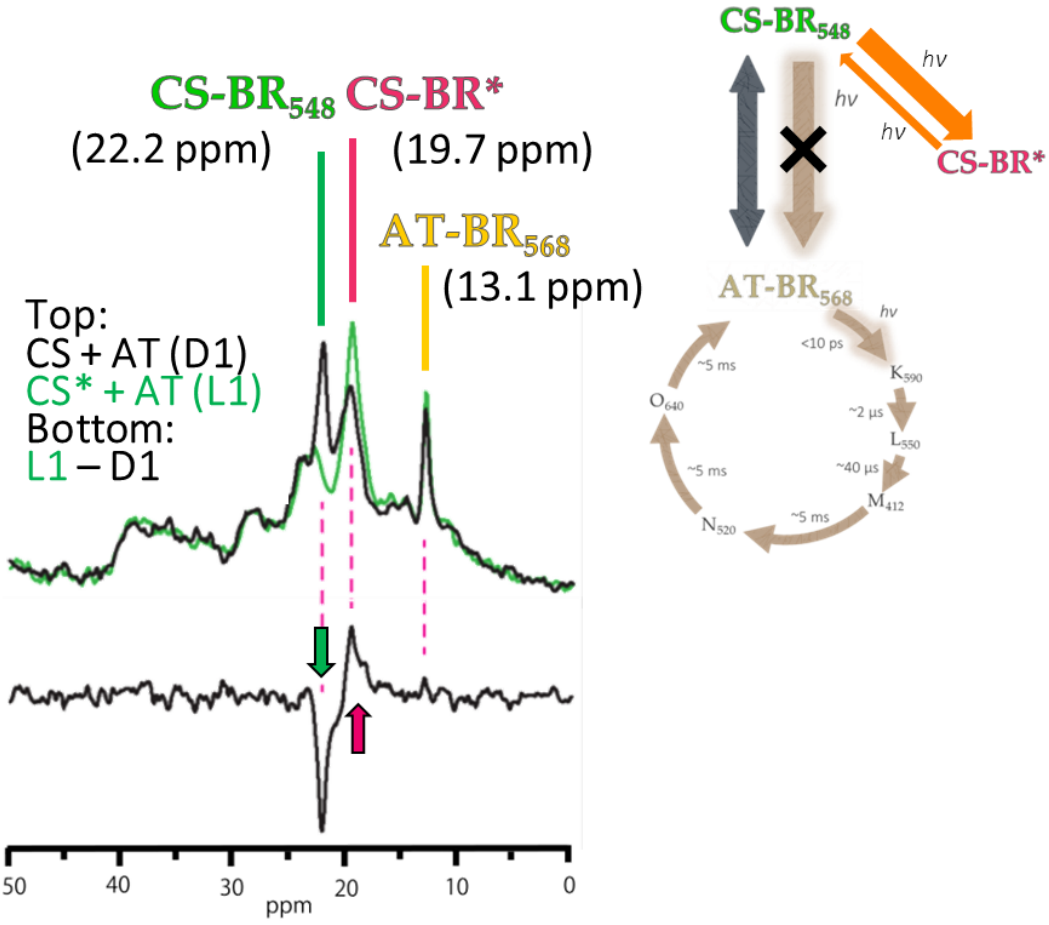

Figure 38. Comparison between CP-MAS spectra of [20-^{13}C]Ret-BR at D1 and L1 at -20°C.
(Left top) Overlapped spectra of D1 and L1. (Left bottom) Difference spectrum of two spectra above. (Right) Pathway highlighted in orange represents the change from D1 to L1.

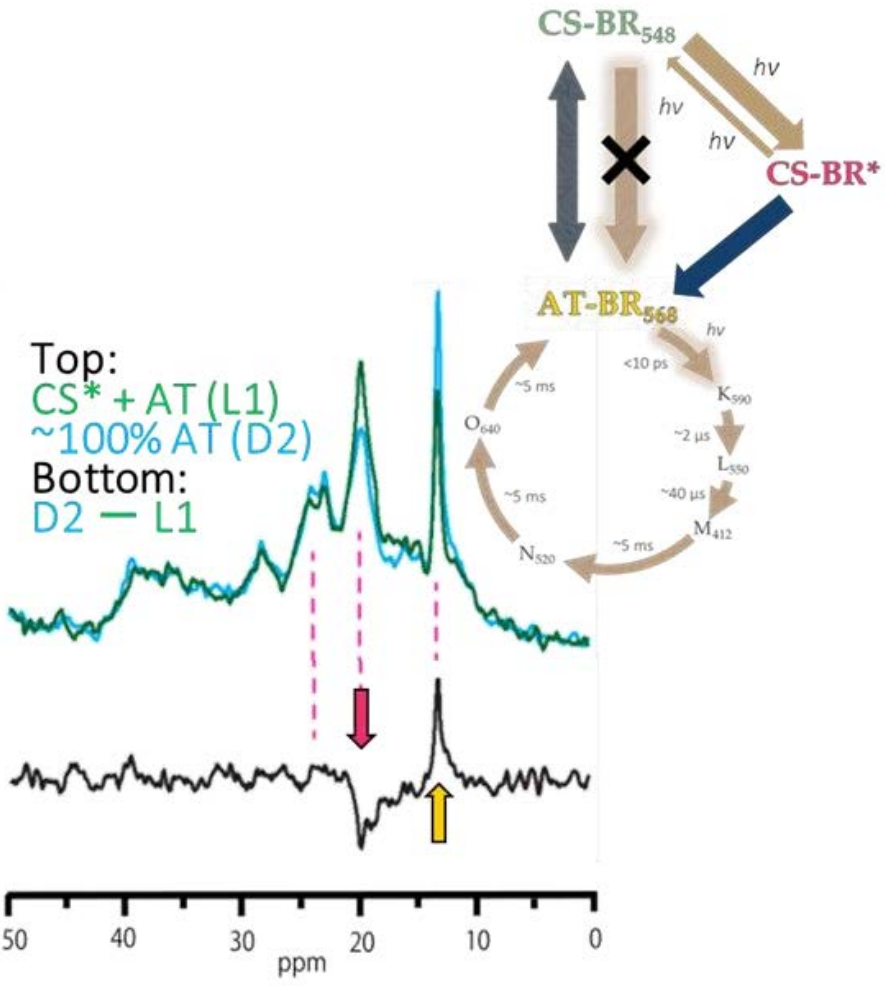

Figure 39. Comparison between CP-MAS spectra of [20-^{13}C]Ret-BR at L1 and D2 at -20°C. (Left top) Overlapped spectra of D1 and L1. (Left bottom) Difference spectrum of two spectra above. (Right) Pathway highlighted in orange represents the change from L1 to D2.

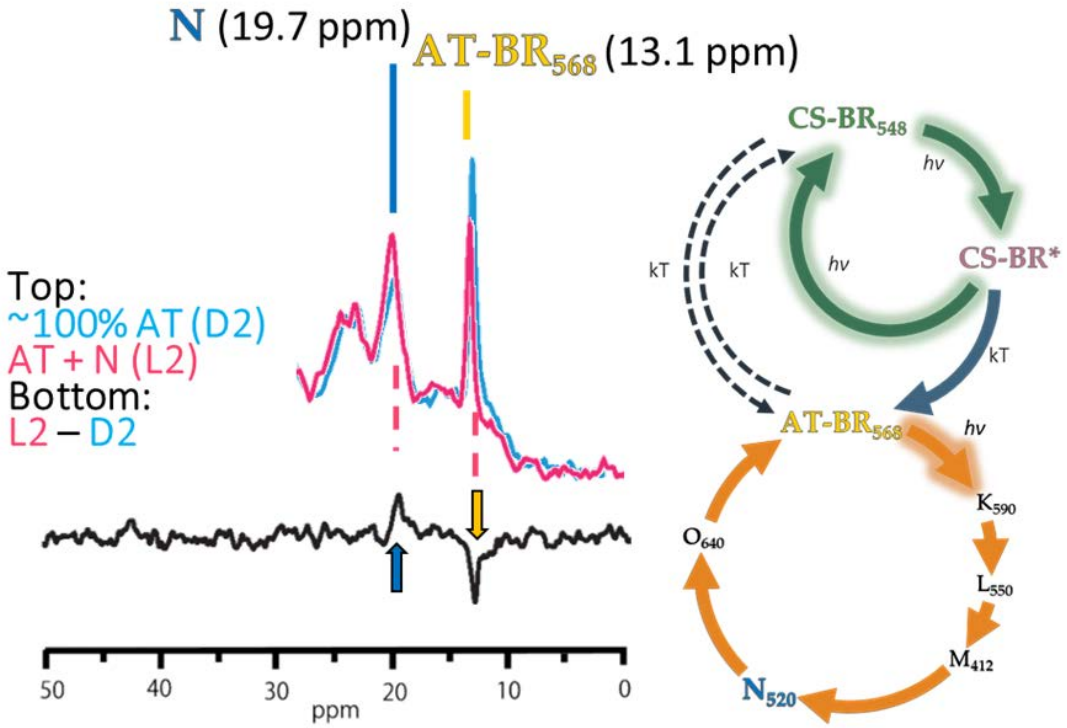

Figure 40. Comparison between CP-MAS spectra of [20-^{13}C]Ret-BR at D2 and L2 at -20°C. (Left top) Overlapped spectra of D1 and L1. (Left bottom) Difference spectrum of two spectra above. (Right) Pathway highlighted in orange represents the change from D2 to L2.

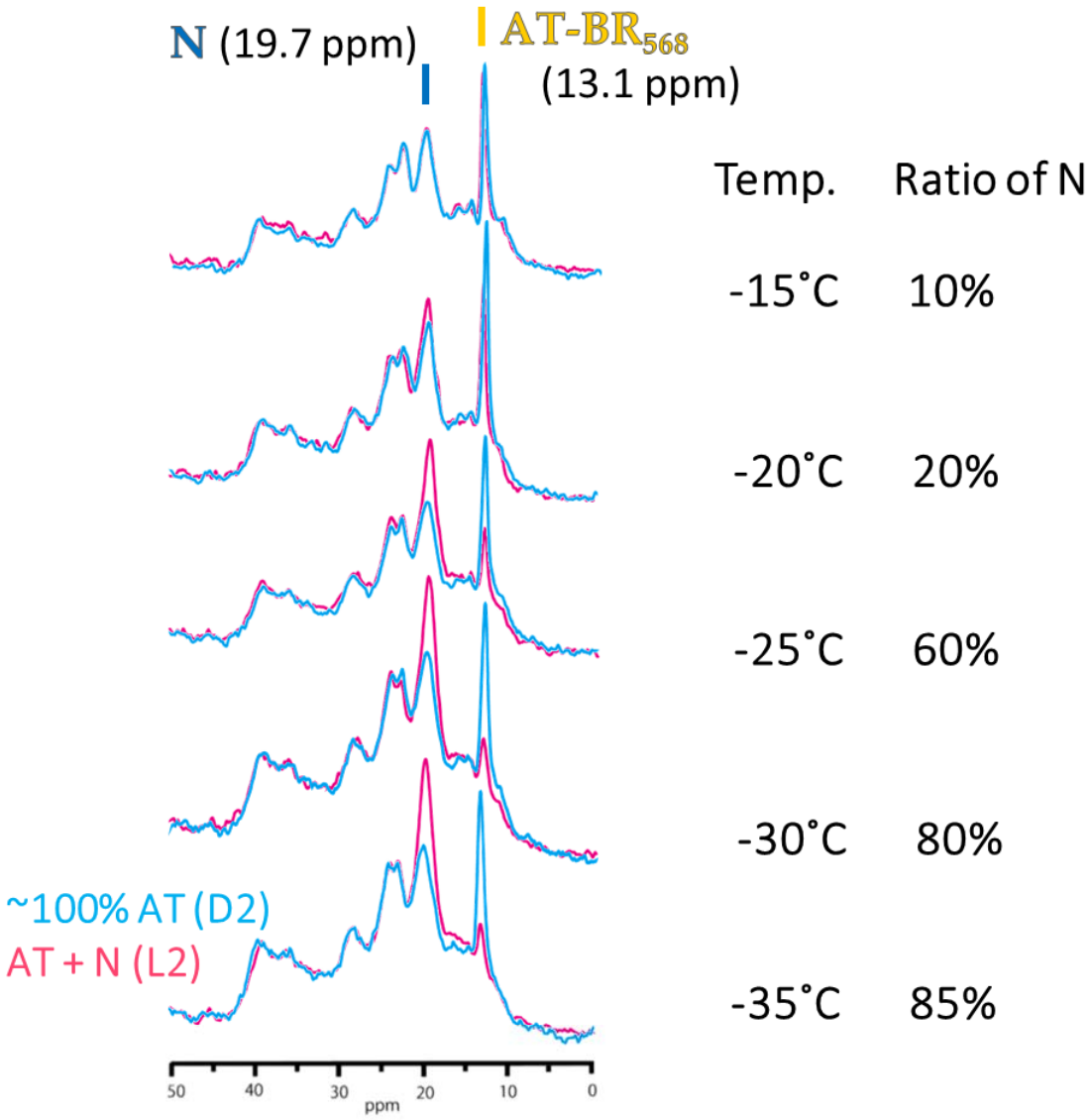

Figure 41. Comparison of CP-MAS spectra of [20-^{13}C]Ret-BR at different temperatures.

[1-^{13}C]Tyr signal observation at each photo-intermediate

Simultaneously observed Tyr backbone signal showed corresponding signal change as retinal C20. At D1 at 20˚C, overlapping two peaks at 175.8 ppm and 174.2 ppm were observed which were assigned to be α-helix and loop based on the previous assignments (Figure 42).[272,273] Loop peak was slightly higher than α-helix peak at D1 when retinal composition of all-*trans* and 13-*cis*, 15-*syn* was 1:1. With the light irradiation (L1), spectrum did not change although retinal composition changed to ~100% all-*trans*. Change of retinal conformation from 13-*cis*, 15-*syn* to all-*trans* is thought to affect tyrosine vicinal of retinal;[273] however, no change was observed. Putting back to dark state, D2, it did not change as it can be expected.

No change was observed at 20˚C, but there was a change at CS*-intermediate at lower temperature. The spectrum at D1 at -20˚C was almost the same as at 20˚C. At L1, α-helix peak increased and instead, loop peak decreased in its intensity (Figure 43). This change may be caused by the conformational change in CS*-intermediate. At light-adapted state at D2, it went back to the previous spectra pattern with higher intensity in loop as D1 (Figure 44). Still there are some peaks in difference spectrum.

Tyr spectra showed similar change as CS* intermediate when N-intermediate was trapped at L2. As it gets to lower temperature, the loop peak decreased and the α-helix peak increased (Figure 45). Ratio of trapped intermediate was decided from retinal spectra.

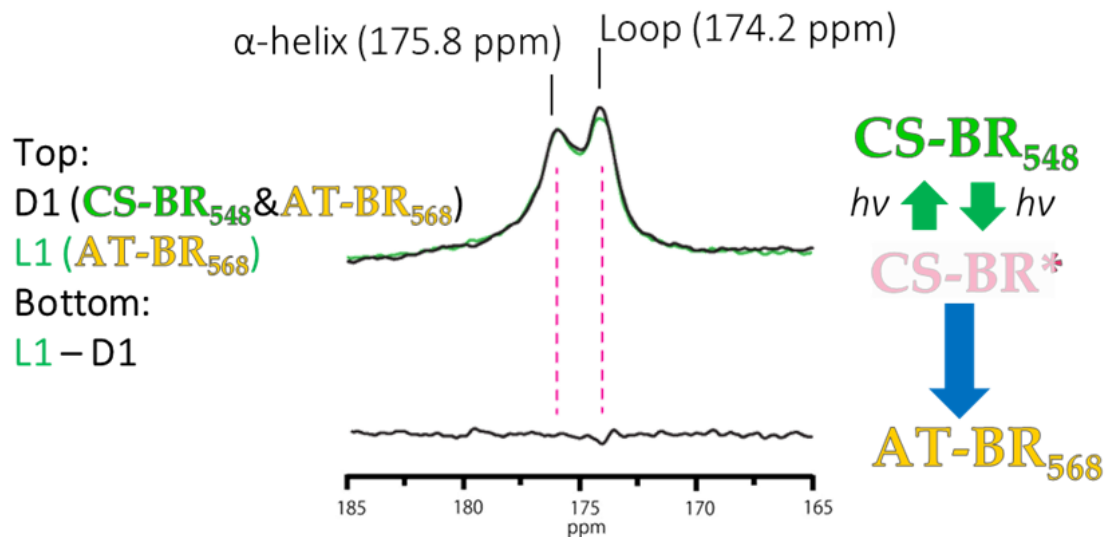

Figure 42. Comparison between CP-MAS spectra of [1-^{13}C]Tyr-BR at D1 and L1 at 20°C and observing pathways.

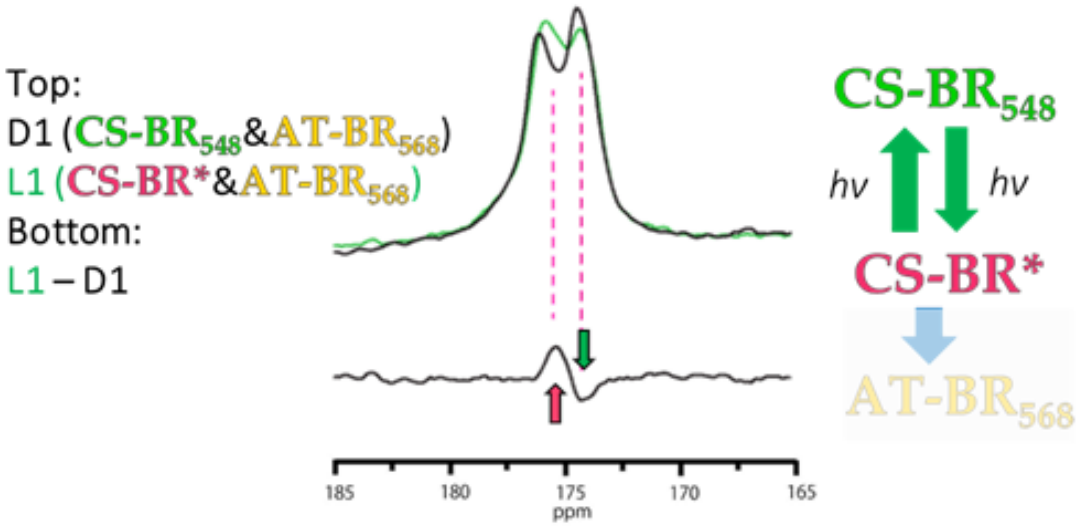

Figure 43. Comparison between CP-MAS spectra of [1-^{13}C]Tyr-BR at D1 and L1 at -20°C and observing pathways.

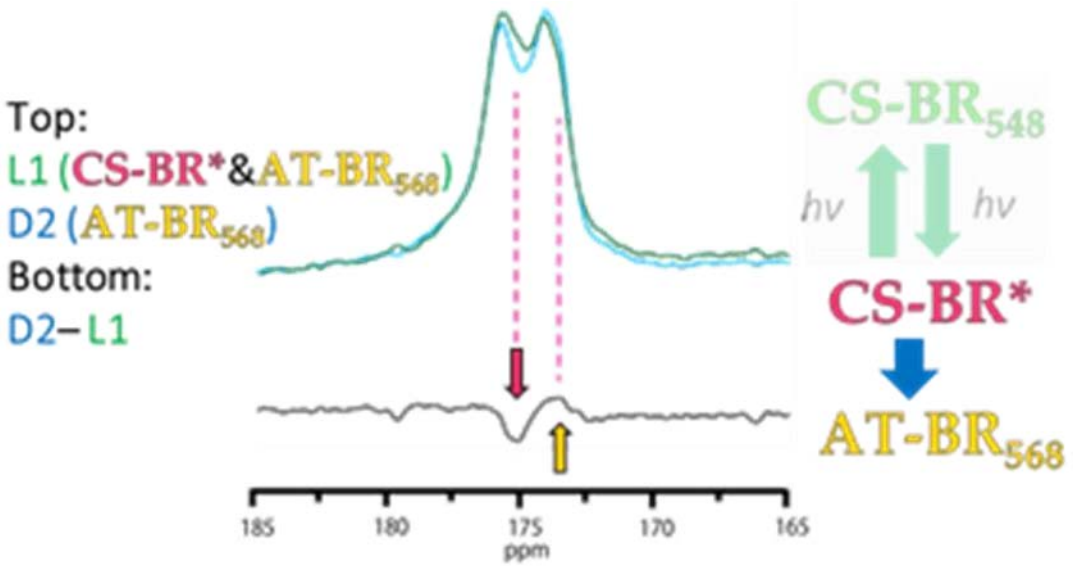

Figure 44. Comparison between CP-MAS spectra of [1-^{13}C]Tyr-BR at L1 and D2 at -20°C and observing pathway.

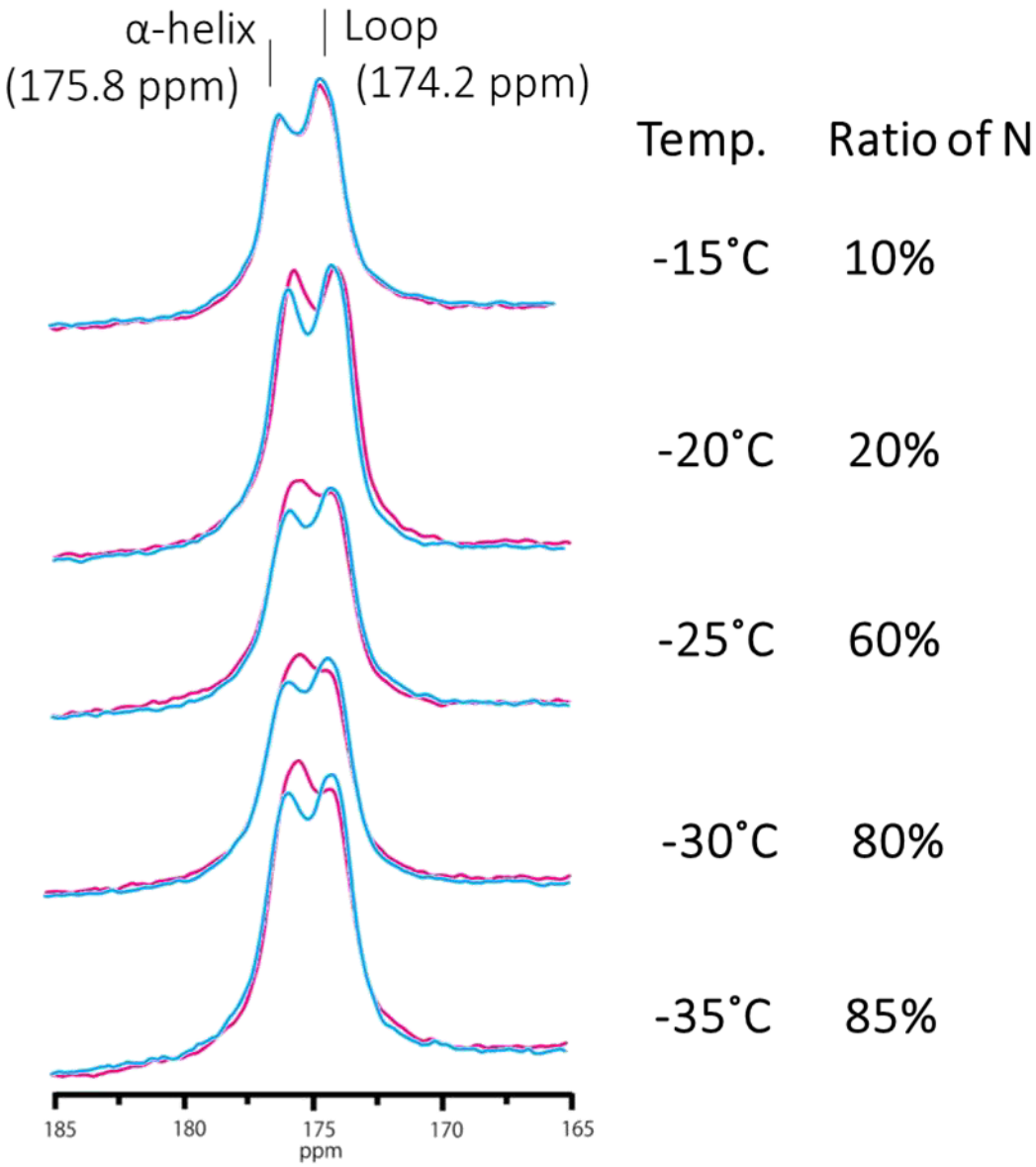

Figure 45. Comparison of CP-MAS spectra of [1-^{13}C]Tyr-BR at different temperatures.

Discussion on the photocycle observed in WT

Existence of CS* intermediate

Temperature-dependent retinal conformation change revealed the existence of photo-intermediate in 13-*cis* photocycle. The change observed at 20˚C is a typical retinal change seen in many papers. The retinal change at -20˚C showed the photo-intermediate existence during the pathway from 13-*cis*, 15-*syn* to all-*trans*. This should be a photo-intermediate as the light illumination is of necessity to avoid leak to all-*trans* state as well as the temperature of -20˚C or lower to keep CS*-intermediate trapped for more than one day as it quickly changes to all-*trans* state without light and with higher temperature. Stational trap of this state was, therefore, enabled by the equilibrium between ground state of 13-*cis* photocycle and CS*-intermediate which both pathways from 13-*cis*, 15-*syn* to CS* state and from CS* to 13-*cis*, 15-*syn* state require the photon absorption.

The pathway from CS* to all-*trans* state occurs in dark indicating that this pathway is thermal relaxation. This explains the reason of not trapping CS*-intermediate at 20˚C where speed of relaxation pathway from CS* to all-*trans* increases with temperature that exceeds the speed of CS* changing back to the ground state of 13-*cis* photocycle. Therefore, the photocyclic pathway from CS to AT through CS* is suggested to exist at 20°C as well, but was not detectable because of the kinetic balance of the two branched pathways at CS*-intermediate.

At L2, the observation of pure N-intermediate was successful by illuminating light-adapted state. The trapped ratio of AT and N-intermediate changes depending on the temperature as the relaxation from N occurs thermally. The chemical shift of N- and CS*-intermediate was similar at L1, however the rough population of N-intermediate can be estimated based on the signal integration of

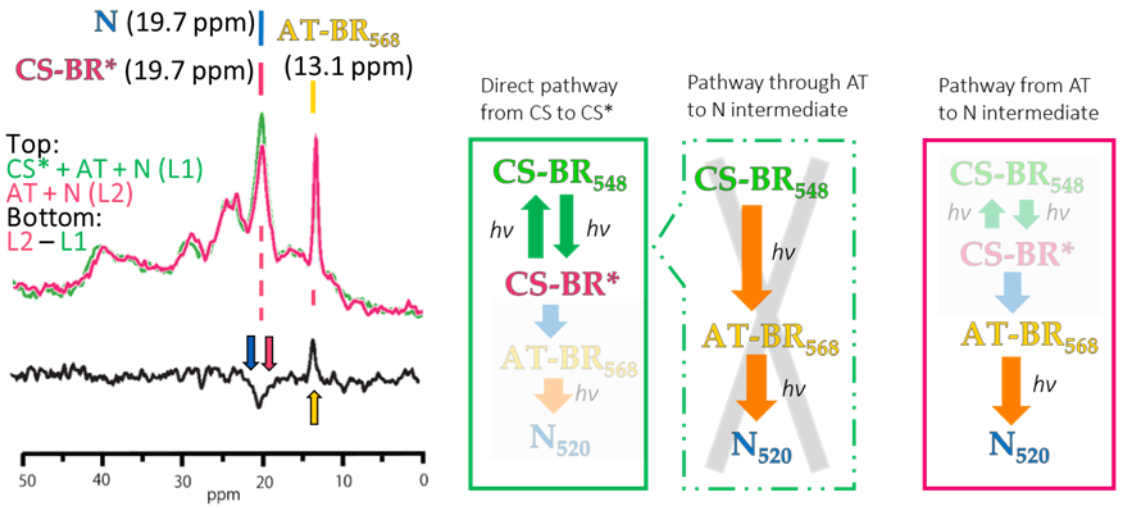

Figure 46. Comparison between CP-MAS spectra of [20-^{13}C]Ret-BR at L1 and L2 at -20°C and verification of 13-*cis intermediate existence.**

AT at D1. The peaks of CS*- and/or N*-intermediate at L1 and L2 arise from the CS*-intermediate changed from CS (~100% conversion of ~50% existing species) and N-intermediate from AT (~20% conversion of ~50% existing species), and N-intermediate from AT (~20% conversion of ~100% existing species), respectively. Indeed, the signal intensity difference was observed in L1 and L2 spectra neglecting the hypothesis that species observed at L1 is an intermediate in all-*trans* photocycle i.e. detecting only N-intermediate. Therefore, from these comparisons, the existence of CS*-intermediate was clearly revealed (Figure 46). The photocycle including CS*-intermediate was revealed as is shown in Figure 47.

Tyr structural change upon retinal isomerization

Tyr spectra showed similar spectra pattern for dark-adapted and light-adapted states. The overlapping signal of 11 Tyr residues in BR indicate the backbone structural similarity of AT and CS as well as CS*- and N-intermediate, but the difference between ground states and photo-intermediates. These data indicate that the CS photocyclic pathway is sort of similar to AT photocycle and the importance of CS*-intermediate during the photocyclic activity. Previous studies on Tyr in BR, especially Tyr185 in the vicinity of retinal, discussed the correlation of retinal and Tyr185 conformation. Single Tyr185 signal was observed by 2D ^{13}C–^{13}C PDSD correlation spectra of the dark-adapted BR.[233] The solution NMR structures of AT and CS showed no displacements of Tyr185 during dark-light adaptation as well as crystallographic data.[33,34,274] However, Tyr assignment by REDOR filter NMR method, two peaks appeared as Tyr185 carbonyl signal with splitting of 4.3 ppm indicating the two conditions exists in dark-adapted state[272,273] which is contradictory to the previous report.

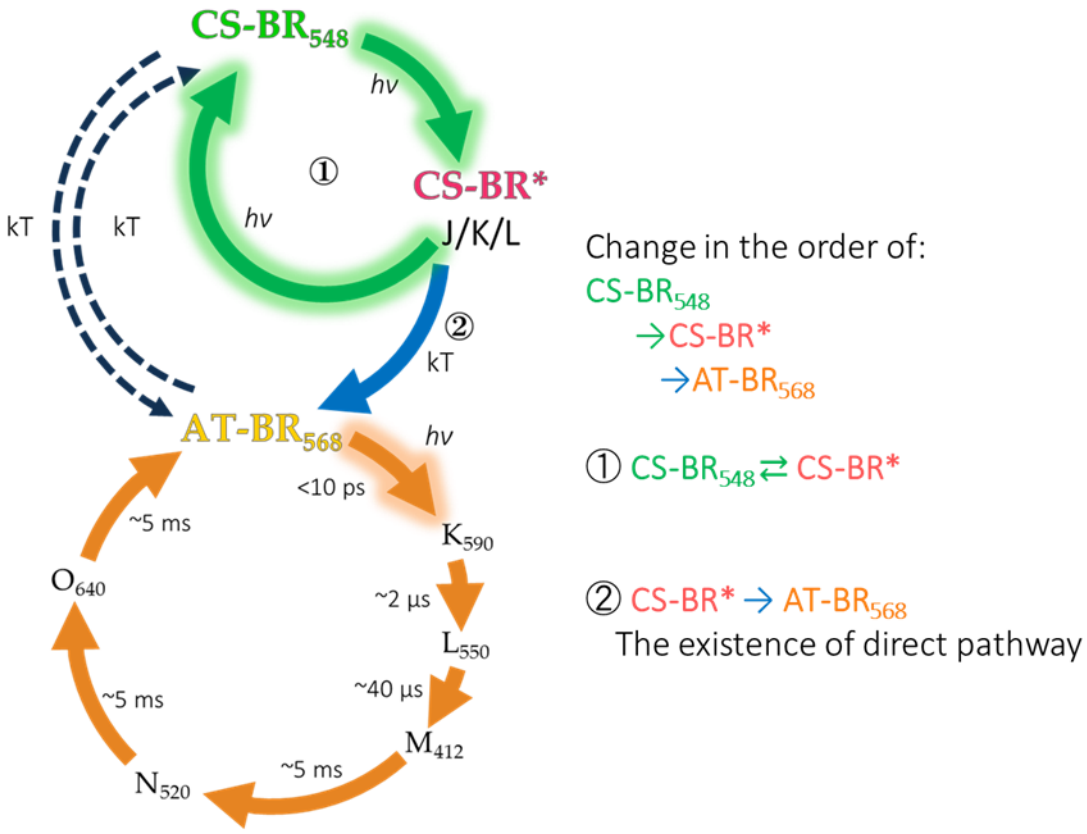

Figure 47. Photocycle obtained from these experiments and key feature of this new photocycle.

Results of Y185F observation

Photo-reaction pathways as revealed with [20-^{13}C]retinal(Ret)-Y185F-BR

Figure 48 shows the temperature variation of [20-^{13}C]Ret-Y185F-BR over the range from 20°C to −40°C. The BR signals were not pronounced at 20°C, 0°C and −20°C, but the signals were markedly increased at −40°C. This phenomenon is explained as follows: the motion of retinal becomes rigid in the low temperature range and consequently the cross-polarization efficiency increases and hence the signal intensity becomes pronounced. ^{13}C NMR signals of [20-^{13}C]retinal also increased markedly and the signals at 21.7 and 13.2 ppm were assigned to the 13-*cis*, 15-*syn* (CS) and all-*trans* (AT) states of Y185F-BR, and were consistent with the signals at 22.0 and 13.3 ppm for the CS and AT states of WT as shown in Table 1. The ratio of CS : AT was approximately 4 : 1; hence, in the dark, the CS state of the Y185F-BR mutant is more stable than the AT state.

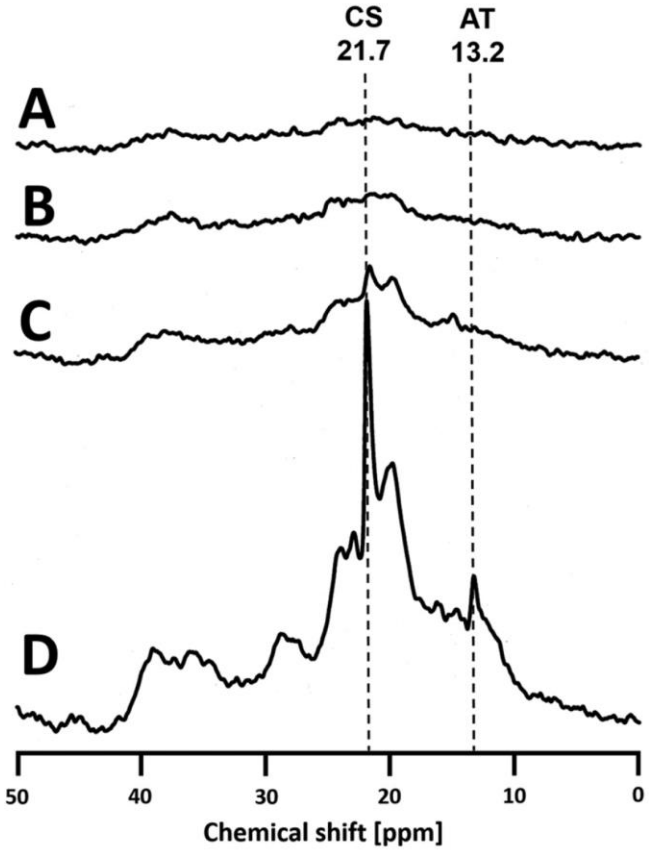

Figure 48. ^{13}C CP-MAS NMR spectra of [20-^{13}C]Ret-Y185F-BR at various temperatures.
(A) 20 °C, (B) 0 °C, (C) −20 °C, and (D) −40 °C.

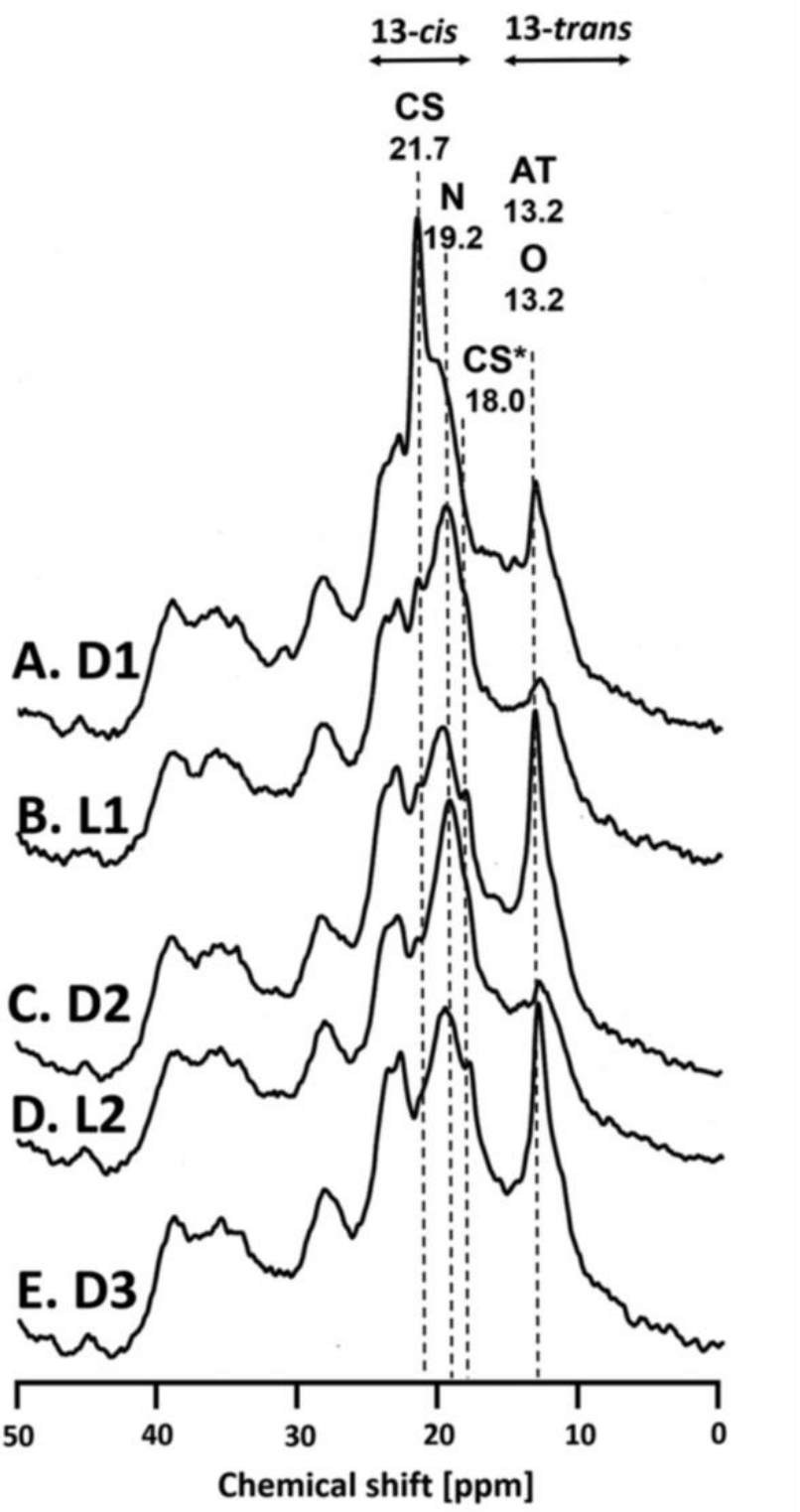

Figure 49. ^{13}C CP-MAS NMR spectra of [20-^{13}C]Ret-Y185F-BR at −40 °C under various conditions. NMR spectra were recorded (A. D1) in the dark, (B. L1) under irradiation with 520 nm light, (C. D2) in the dark, (D. L2) under irradiation with 520 nm light, and (E. D3) in the dark.

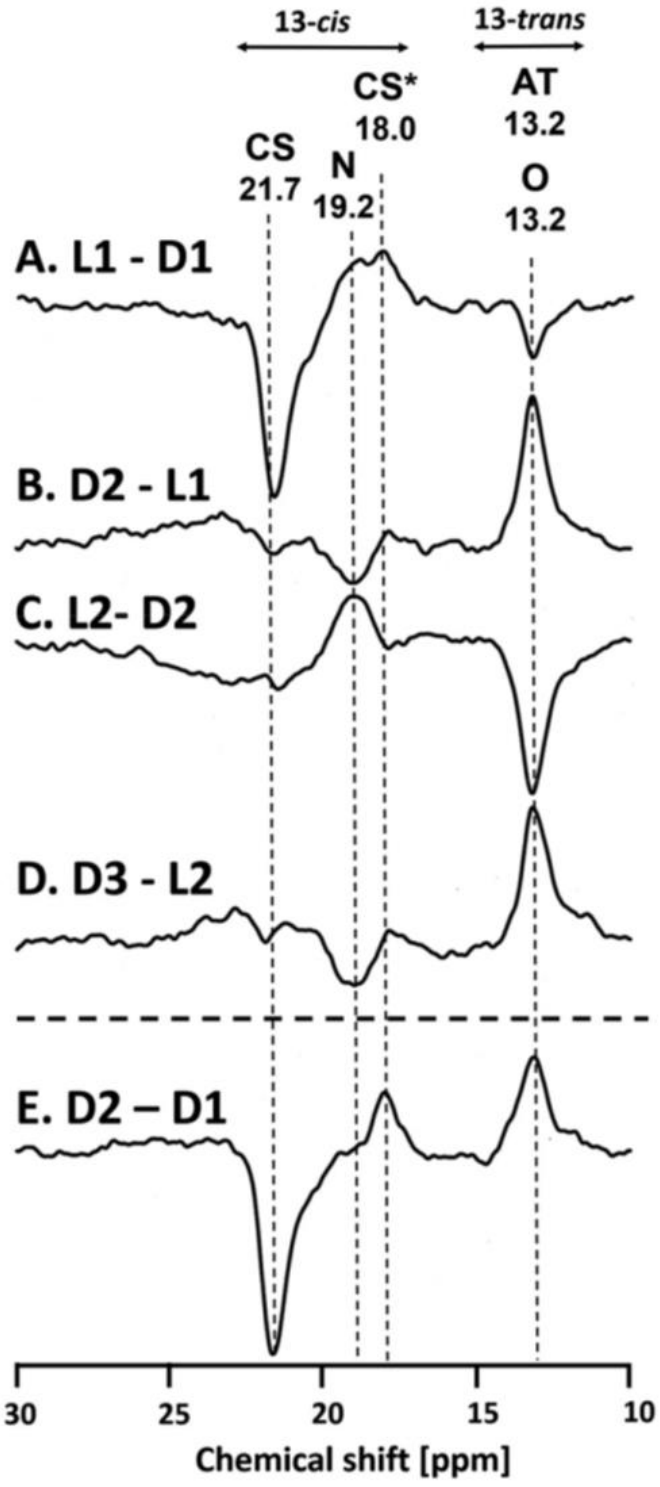

Figure 50. Difference spectra of [20-^{13}C]Ret-Y185F-BR at −40 °C.
The pathways are from (A. L1-D1) D1 to L1, (B. D2-L1) L1 to D2, (C. L2-D2) D2 to L2, (D. D3-L2) L2 to D3, and (E. D2-D1) D1 to D2.

As shown in Figure 49, the photo-reaction pathways were investigated by acquiring ^{13}C CP-MAS NMR spectra at −40°C under the following conditions: (1) in the dark (D1), which provided a dark-adapted state; (2) under illumination with 520 nm LED light (L1), which provided a photo-excited state from D1; (3) in the dark (D2), which provided a light-adapted state from L1; (4) and then under illumination with 520 nm LED light (L2), which provided a photo-excited state from D2; and (5) in the dark (D3), which provided a light-adapted state from L2. The ^{13}C CP-MAS NMR spectra recorded during D1, L1, D2, L2 and D3 at −40°C are shown in Figure 50. In the first process (D1 to L1), the signals at 21.7 and 13.2 ppm (which were assigned to the CS and AT states, respectively) decreased, and the signals at 19.2 ppm (which were assigned to the N- and CS*-intermediates) increased (Figure 49A and B).

The signals associated with the transformation processes were further analyzed by examining the L1 minus D1 (the light-adapted state minus the dark-adapted state) difference spectrum (Figure 50A), in which negative peaks indicate reactant species and positive peaks indicate product species. Figure 51A indicates that the CS (21.7 ppm) and AT (13.2 ppm) states decreased and the N- (19.2 ppm) and CS*- (18.0 ppm) intermediates increased under irradiation with 520 nm light. The changes in the signal intensity indicate that the CS*-intermediate was transformed from the CS state and the N-intermediate was transformed from the AT state. In addition to these two pathways, the CS state was converted to the AT state through the CS photocycle and subsequently transformed to the N-intermediate because the NMR signal intensity of the N-intermediate is the same as that of the CS* intermediate although the NMR signal intensity of the AT state is much smaller than that of the CS state. As shown in Figure 50B, in the process leading from L1 to D2, the N-intermediate (19.2 ppm) decreased and the O-intermediate (13.2 ppm) increased, indicating that the N-intermediate transformed to the O-intermediate in the dark. This result is consistent with the report that a stable O-intermediate forms during light-adaptation for the Y185-BR mutant.[275] As shown in Figure 50C, in the process leading from D2 to L2, the O-intermediate transformed to the N-intermediate possibly through the AT state by considering that Y185F-BR takes a similar photocycle to that of AT of wild type BR under irradiation with 520 nm light. This result is also consistent with the report that photoexcitation of the O^{Y185F}-intermediate produced an N-intermediate and an M-intermediate was not found.[260] Figure 50D shows that in the process leading from L2 to D3, the N-intermediate transformed to the O-intermediate in the dark.

Figure 50E shows the process leading from the D1 to D2 state: the CS state transformed not only to the CS*-intermediate, but also to the O-intermediate, indicating that the end products derive from the CS state. The chemical shifts in the AT and CS states and in the CS*-, N- and O-intermediates indicate that the CS state and the CS*- and N-intermediates possess a 13-*cis* configuration and that the AT state and O-intermediate form a 13-*trans* configuration by comparing the chemical shifts corresponding to the configurations of retinal at individual intermediates (Table 8).

Table 8. ^{13}C chemical shift values (ppm) for the various states of [20-^{13}C]Ret-, [14-^{13}C]Ret-, and [15-^{13}C]Ret-labeled Y185F-BR as determined using photo-irradiation solid state NMR spectroscopy at −40 °C.

	[20-^{13}C]Ret	[14-^{13}C]Ret	[15-^{13}C]Ret	Configuration
AT	13.2 ± 0.1	123.1 ± 0.1	159.4 ± 0.1	13-*trans*, 15-*anti*
CS	21.7 ± 0.1	110.0 ± 0.1	165.4 ± 0.2	13-*cis*, 15-*syn*
CS*	18.0 ± 0.2	115.3 ± 0.2	162.2 ± 0.2	13-*cis*, 15-*syn*
N	19.2 ± 0.2	125.4 ± 0.2	163.8 ± 0.2	13-*cis*, 15-*anti*
O	13.2 ± 0.1	123.1 ± 0.2	159.4 ± 0.2	13-*trans*, 15-*anti*
AT (WT-bR$_{568}$)[a]	13.3	122.0	160.0	13-*trans*, 15-*anti*
CS (WT-bR$_{548}$)[a]	22.0	110.5	163.2	13-*cis*, 15-*syn*
N (WT-bR)[b]		115.0		13-*cis*, 15-*anti*

[a] Ref. 20. [b] Ref. 24.

Photo-reaction pathways as observed with [14-^{13}C]Ret-Y185F-BR

The retinal configuration of the individual photo-intermediates (AT and CS states, and CS*-, N-, and O-intermediates) were further examined by inspecting the chemical shifts of [14-^{13}C]-Ret-Y185F-BR signals. In the dark-adapted state, signals at 110.0 and 123.1 ppm were assigned to the CS and AT states as shown in Figure 51A. In the process leading from D1 to L1, signals of the CS and AT states decreased and those of the CS*-intermediate at 115.3 ppm and the N-intermediate at 125.4 ppm clearly increased in the difference spectrum (Figure 52A). This result indicates that the CS state is converted to the CS*-intermediate and the AT state is converted to the N-intermediate under irradiation with 520 nm light. At the same time, the CS state is also converted to the N-intermediate, probably through the leaking process from the CS-photocycle to the AT state because the NMR signal intensity of the N-intermediate appeared larger than that of the CS*-intermediate although the NMR intensity of the AT state was much smaller than that of the CS state. In the process leading from L1 to D2, signals of the N-intermediate decreased and those of the O-intermediate increased in the dark (Figure 52B). This result indicates that the N-intermediate was converted to the O-intermediate. It should be noted that the O-intermediate is highly stable in the dark at −40°C. In the process leading from D2 to L2, signals of the O-intermediate decreased and those of the N-intermediate increased, whereas signals of the CS*-intermediate did not change (Figure 52C). These data indicate that the O-intermediate excited to the N-intermediate possibly via the AT state by considering that Y185F-BR takes a similar photocycle to that of AT of wild type BR under irradiation with 520 nm light. It should also be noted that the CS*-intermediate is not excited under irradiation with 520 nm light. In the process leading from L2 to D3, the N-intermediate was converted to the O-intermediate in the dark (Figure 52D). In the process leading from D1 to D2, the CS state was converted not only to the CS*-intermediate as an end product, but also to the O-intermediate (or the AT state) (Figure 52E).

Analysis of the chemical shift data indicates that the AT and CS states and the CS*-, N- and O-intermediates form (13-*trans*, 15-*anti*), (13-*cis*, 15-*syn*), (13-*cis*, 15-*syn*), (13-*cis*, 15-*anti*) and (13-*trans*, 15-*anti*), respectively (Table 8). It is stressed that configurations of C13=C14 and C15=N bonds in retinal can be clearly assigned by ^{13}C chemical shifts of [20-^{13}C] and [14-^{13}C]retinals, respectively.

Because the CS*-intermediate is very stable at −40°C, the temperature was increased to −20°C in the dark for 1 day. After the temperature was decreased to −40°C, the signal was acquired as shown in Figure 53B. The signal of the CS*-intermediate decreased and that of the AT state (or O-intermediate) increased. Subsequently, the temperature was increased to 20°C for 1 day, and the signals were acquired at −40°C (Figure 53C). The signals of the AT state (or O-intermediate) decreased and those of the CS state increased to equilibrate to the dark-adapted state. The CS state again was converted to the CS*- and N-intermediates possibly through the AT state upon irradiation with 520 nm light at −40°C (Figure 53D). This result confirmed that the CS*-intermediate was transformed only from the CS state.

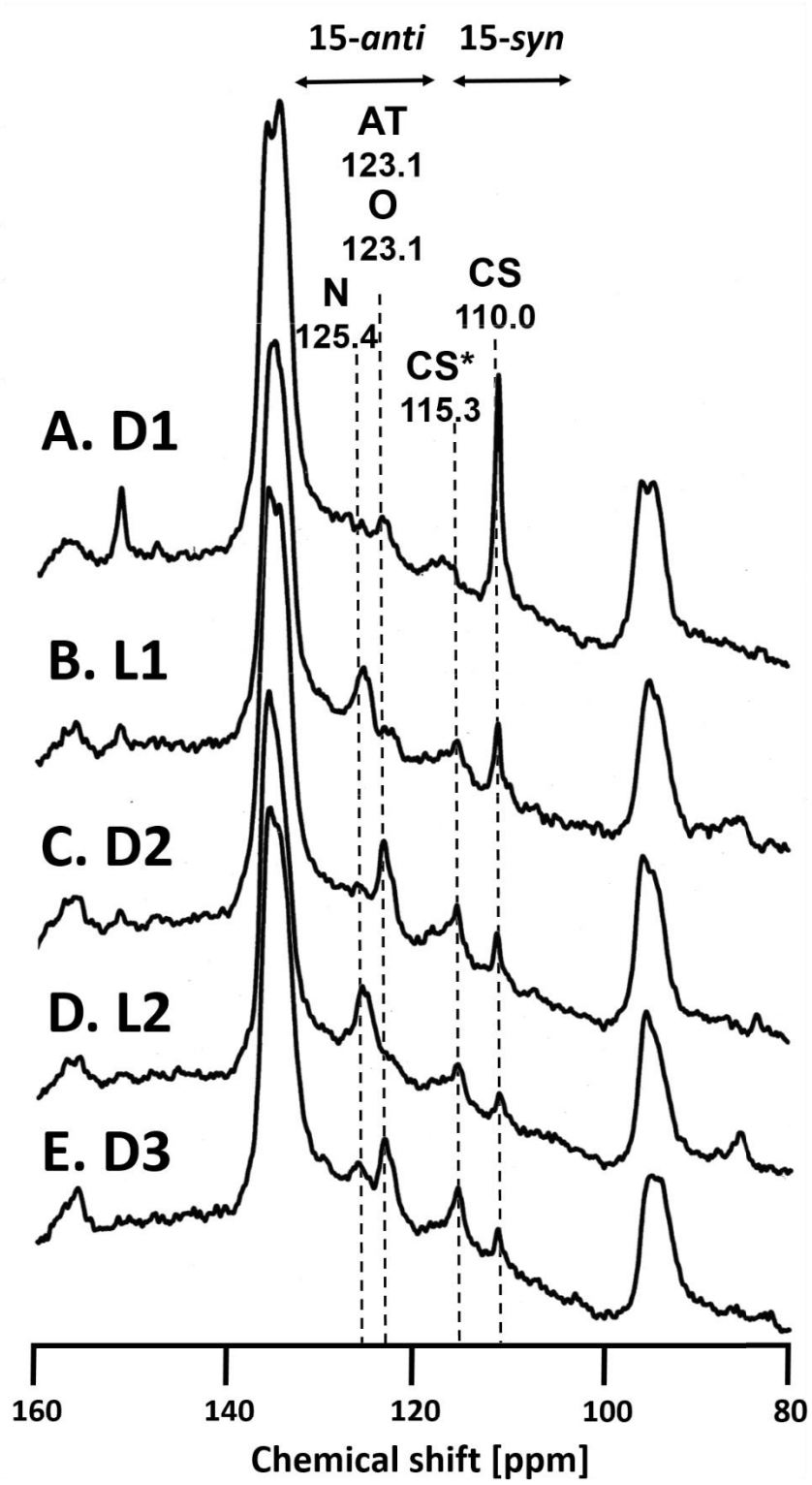

Figure 51. ^{13}C CP-MAS NMR spectra of [14-^{13}C]Ret-Y185F-BR at −40 °C under various conditions. NMR spectra were recorded (A. D1) in the dark, (B. L1) under irradiation with 520 nm light, (C. D2) in the dark, (D. L2) under irradiation with 520 nm light, and (E. D3) in the dark.

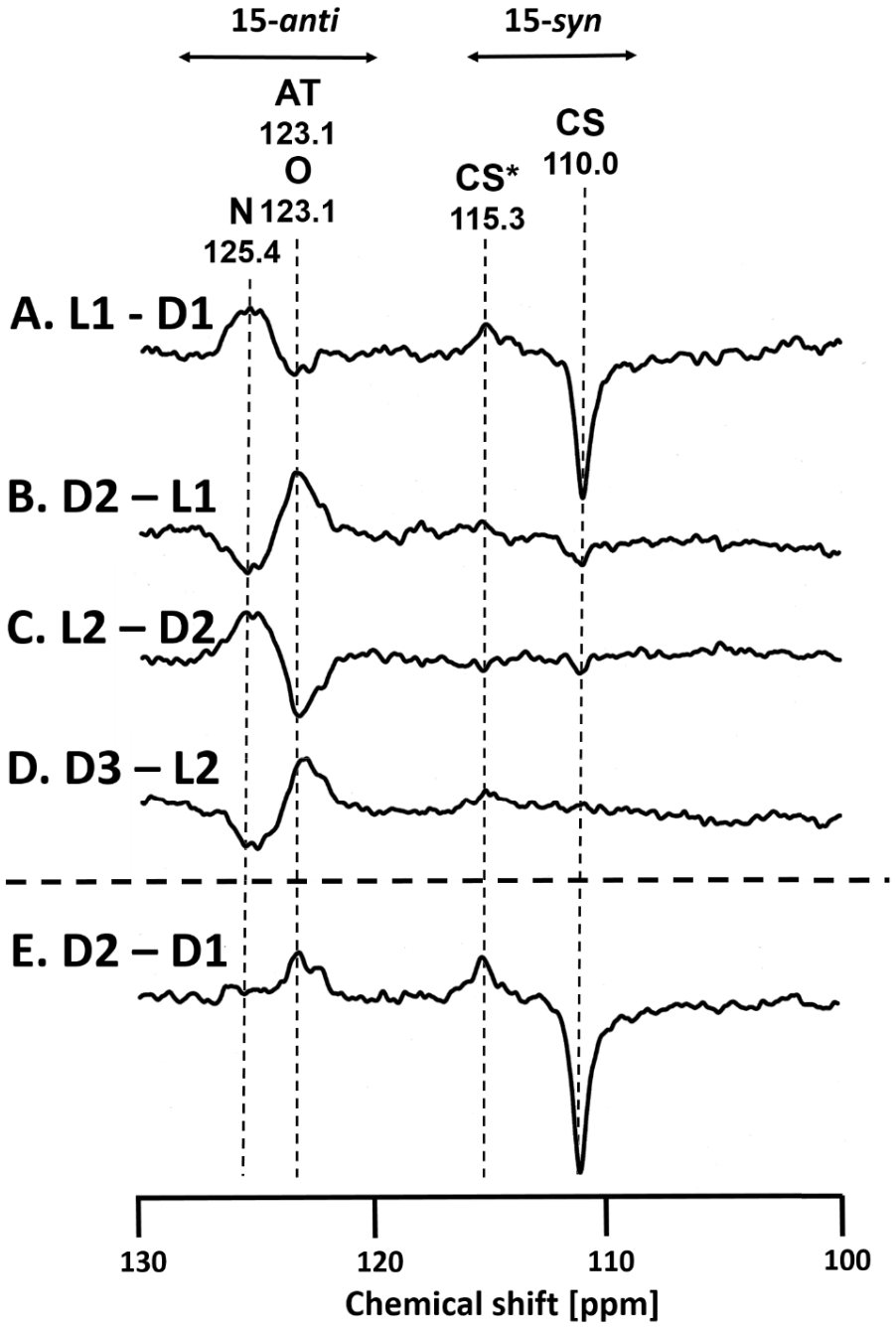

Figure 52. Difference spectra of [14-^{13}C]Ret-Y185F-BR at −40°C.
The pathway from (A. L1-D1) D1 to L1, (B.D2-L1) L1 to D2, (C. L2-D2) D2 to L2, (D. D3-L2) L2 to D3, and (E. D2-D1) D1 to D2 are shown.

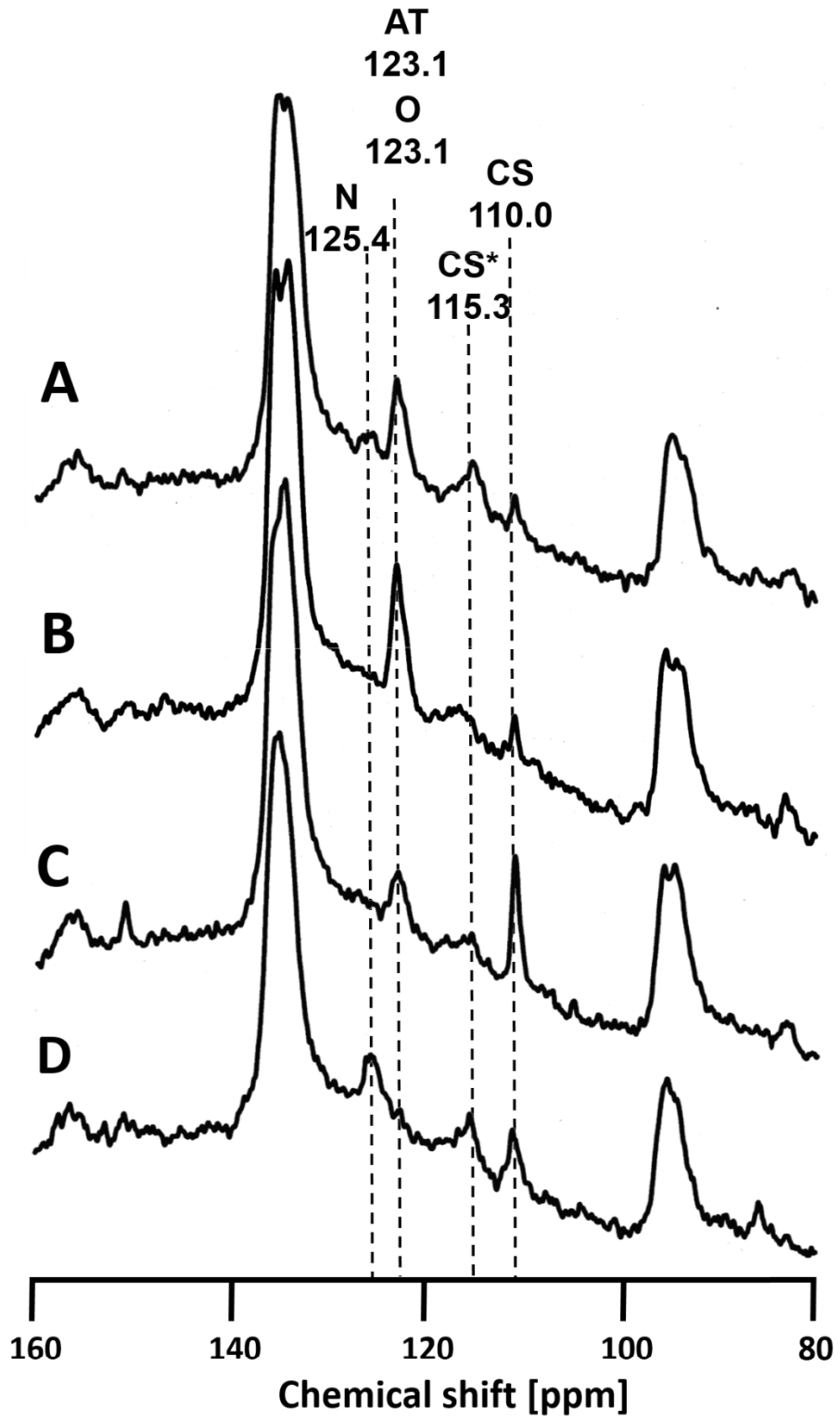

Figure 53. ^{13}C CP-MAS NMR spectra of [14-^{13}C]Ret-Y185F-BR under various conditions.
(A) Spectra recorded at −40°C in the dark after irradiation with 520 nm light. (B) After increasing the temperature to −20°C, recorded at −40°C. (C) After increasing the temperature to 20°C, recorded at −40°C. (D) The NMR spectrum recorded at −40°C under irradiation with 520 nm light.

Photo-reaction pathways as observed with [15-^{13}C]Ret-Y185F-BR

The retinal configuration of the individual photo-intermediates (the AT and CS states, and the CS*-, N-, and O-intermediates) was examined by inspecting the chemical shifts of [15-^{13}C]Ret-Y185F-BR signals at 40°C. In the dark-adapted state, signals at 165.4 and 159.4 ppm were assigned to the CS and AT states, as shown in Figure 54A and Figure 54. In the process leading from D1 (Figure 54A and Figure 54C) to L1 (Figure 54B and Figure 54D), signals of the CS and AT states decreased and those of the CS*-intermediate at 162.2 ppm and the N-intermediate at 163.8 ppm increased (Figure 55A). This result indicates that the CS state is converted to the CS*-intermediate and that the AT state is converted to the N-intermediate. At the same time, the CS state was also converted to the N-intermediate, probably through the leaking process from the CS photocycle to the AT state, because the NMR signal intensity of the N-intermediate appeared larger than that of the CS*-intermediates although the NMR signal intensity of the AT state was much smaller than that of the CS state (Figure 57C and D).

In the process leading from L1 to D2, signals of the N-intermediate decreased and those of the O-intermediate increased (Figure 55B). This result indicates that the N-intermediate was converted to the O-intermediate. It should be noted that the O-intermediate is stable in the dark at −40 °C. In the process leading from D2 to L2, signals of the O-intermediate decreased and those of the N-intermediate increased, whereas signals of the CS*-intermediate did not change (Figure 55C and Figure 56A). These data indicate that the O-intermediate was excited to the N-intermediate via the AT photocycle under irradiation with 520 nm light.

After the D2 process, the temperature was increased to −20 °C in the dark for 1 day, and the signal was acquired at −40 °C (Figure 57B). The signal of the CS*-intermediate decreased and that of the AT state (or O-intermediate) increased. After the temperature was increased to 20 °C for 1 day, the signal was subsequently acquired at −40 °C (Figure 57C). The signal of the AT state (or O-intermediate) decreased and that of the CS state increased until reaching equilibrium as the dark-adapted state (D1 process).

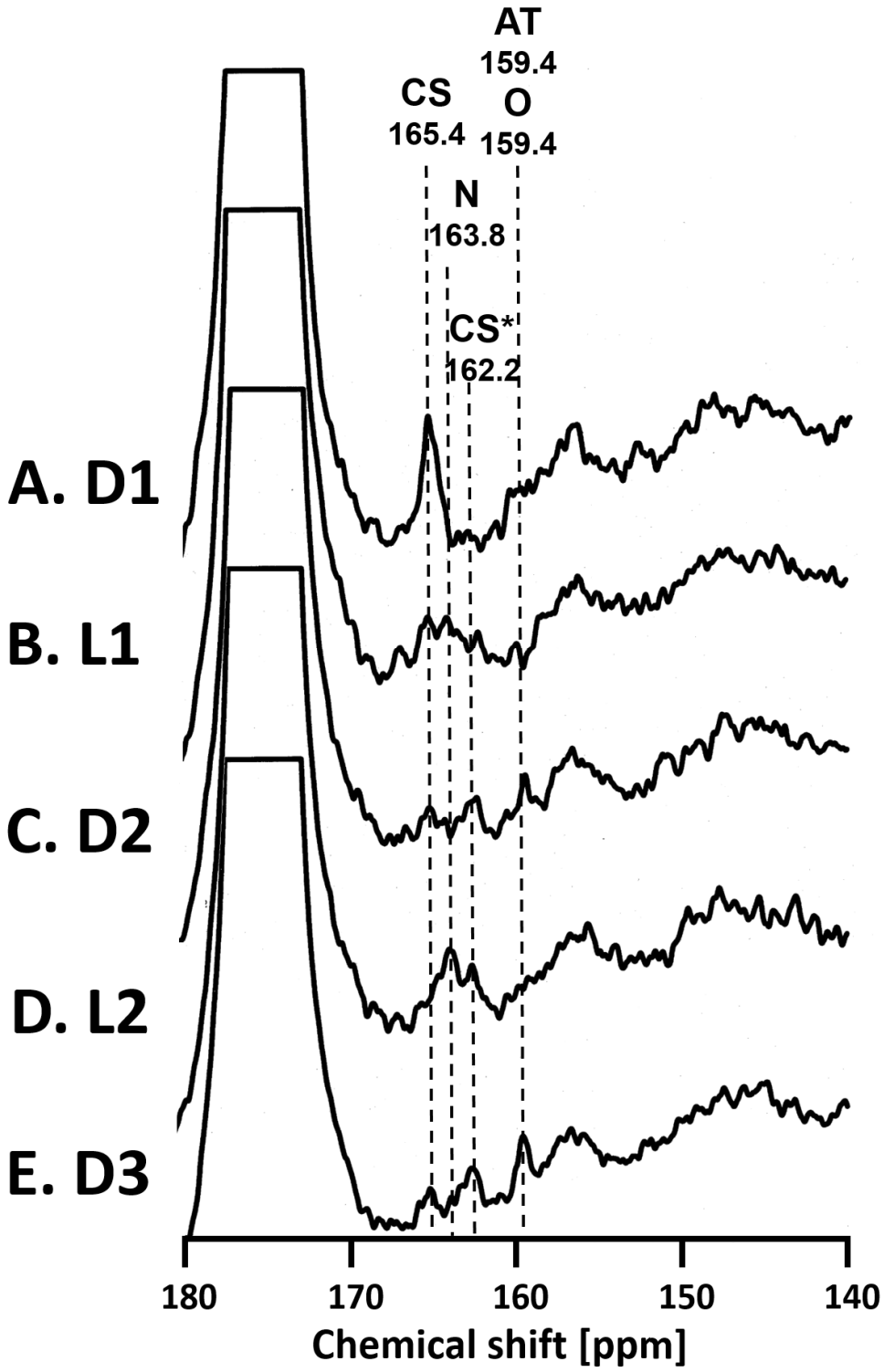

Figure 54. ^{13}C CP-MAS NMR spectra of [15-^{13}C]Ret-Y185F-BR at -40°C and 4 kHz spinning frequency under various conditions.
NMR spectra were collected (A. D1) in the dark, (B. L1) under irradiation with 520 nm light, (C. D2) in the dark, and (D. L2) under irradiation with 520 nm light.

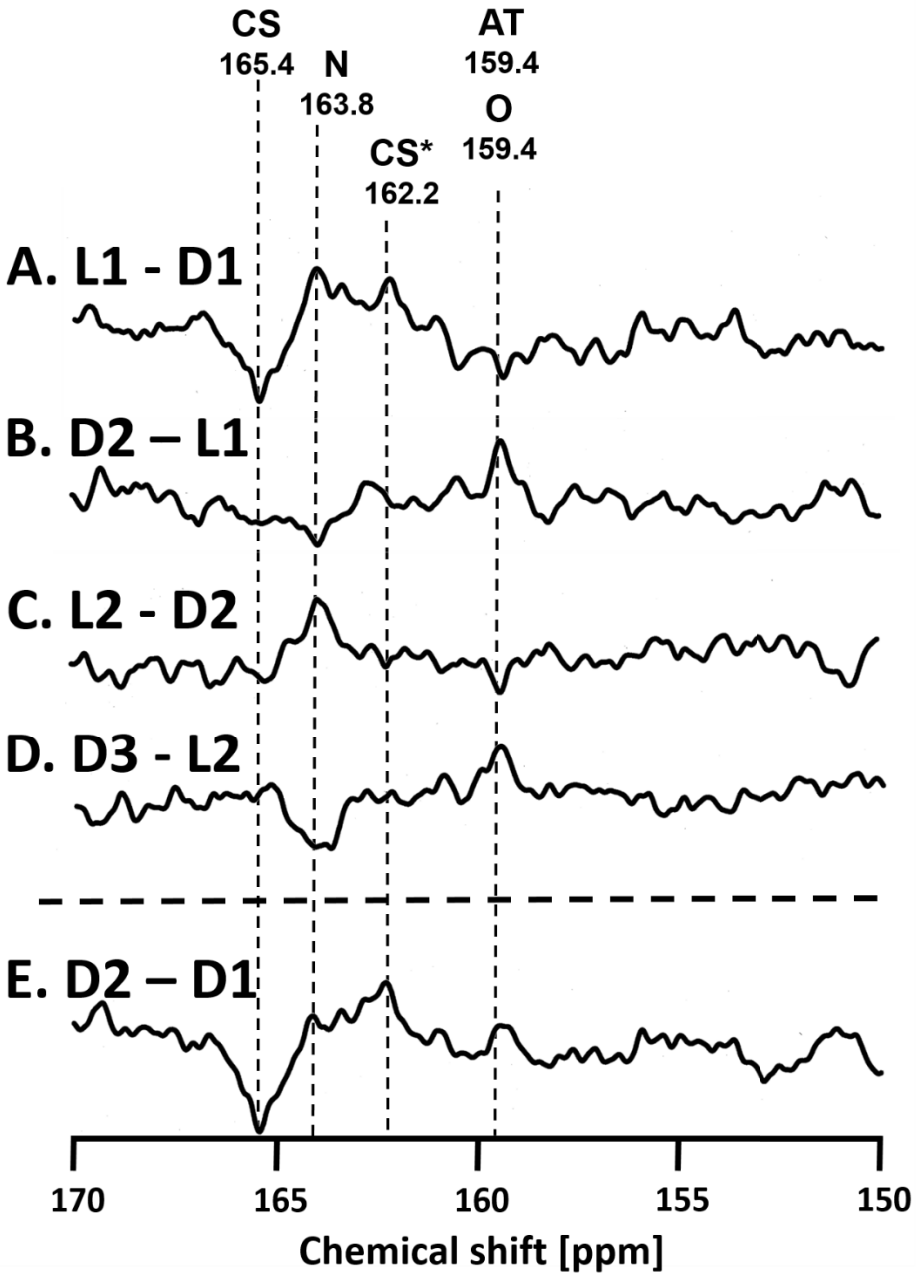

Figure 55. Difference spectra of [15-^{13}C]Ret-Y185F at -40°C and 4 kHz spinning frequency.
The pathway from (A. L1-D1) D1 to L1, (B. D2-L1) L1 to D2, (C. L2-D2) D2 to L2, (D. D3-L2) L2 to D3, and (E. D2-D1) D1 to D2 are shown.

Discussion on the photocycle observed in Y185F

The photo-cycle of the CS state in the dark-adapted state has not been studied extensively. In our photo-irradiation solid state NMR experiments, we clearly detected the conversion of the CS state to the CS*-intermediate (batho-13-*cis*-BR in Iwasa et al.). The CS* intermediate has (13-*cis*, 15-*syn*) retinal configuration which is the same as that of the CS state. However, chemical shift values of 20-^{13}C and 14-^{13}C of retinals are significantly different from each other (Table 1). This experimental evidence indicates that the retinal configuration of the CS* intermediate is twisted significantly from that of the CS state by interacting with the protein, and thus it is recognized that the CS state is converted to the CS*-intermediate with photo isomerization. The CS*-intermediate is highly stable at −40 °C and thus did not change in the dark, whereas it was converted to the AT state at −20 °C (Figure 53B and Figure 57B), which is designated as the light-adapted state in WT bacteriorhodopsin. The pathway from the CS*-intermediate to the AT state (or O-intermediate) is temporary, as evidenced by the inability to distinguish the AT state and the O-intermediate in these photo-irradiation NMR experiments. Further experiments will be necessary to accurately determine the pathway. The CS state was possibly converted to the AT state at −40 °C under irradiation with 520 nm light because the NMR signal of the N-intermediate was the same as or larger than that of the CS* (Figure 50A, Figure 52A and Figure 57D). This stoichiometric relationship suggests that there is a pathway from the CS state to the AT state as shown by the dotted green arrow in Figure 60. The AT state was converted to the N-intermediate through the K-, L- and M-intermediates as the AT photocycle and converted to the O-intermediate in the dark to form the light-adapted state.

This light-adapted state can be changed back to the dark-adapted state by raising the temperature to 20 °C, that is, the AT state is converted to the CS state and the AT : CS molar ratio equilibrates to 1 : 3 (Figure 53C and Figure 57C). It should be noted that the AT state is converted to the N-intermediate upon irradiation with 520 nm light, and this N-intermediate is changed to the O-intermediate in the dark, where it is highly stable in the dark. The O-intermediate is readily converted to the N-intermediate possibly via the AT state by considering that Y185F-BR takes a similar photocycle to that of AT of wild type BR upon irradiation with 520 nm light. In the case of Y185F-BR, it was reported that the O^{Y185F}-intermediate converted to the N-intermediate through the K_{660}-intermediate,[276]which was a different pathway from the AT photocycle. In these NMR experiments, this pathway could not be distinguished from the AT photocycle.

Thus, the photo-reaction pathway of the CS state in Y185F-BR can be summarized as shown in Figure 60. First, the CS state is converted to the CS*-intermediate and also to the AT state under photo-irradiation with 520 nm light. The AT state is converted to the N-intermediate under irradiation with the same wavelength of light through the AT photocycle. Consequently, the N-intermediate is excited directly to the AT state under irradiation with light at 520 nm. On the other hand, the N-intermediate relaxes to the O-intermediate in the dark, because the O-intermediate has a longer half-

life than the N-intermediate at −40 °C. Furthermore, the O-intermediate is converted directly to the AT state under irradiation with 520 nm light. These types of double photon processes can occur in the cases where the half-life is long and the quantum yield of light is optimal.

Similarly, when the D2 state was irradiated with 595 nm light (orange), the O-intermediate was excited to the N-intermediate (Figure 58I and L) through the AT photocycle. In contrast, when the D2 state was irradiated with 365 nm light, the O-intermediate was not excited to the N-intermediate (Figure 59I and L). These results indicate that the N-intermediate is not an M-intermediate, because the M-intermediate absorbs 365 nm light to change to the AT state: hence, the M-intermediate is not trapped under irradiation with 365 nm light at −40 °C. It is also evident that the N-intermediate is converted to the AT state and returns to the N-intermediate via the K and L-intermediates during irradiation with 520 nm light. These photo-reaction pathways were observed with efficient continuous illumination with 520, 595, and 365 nm light. The Y185F-BR mutant significantly increases the half-lives of CS*-, N- and O-intermediates and thus ^{13}C NMR signals of the intermediates were able to be observed by photoirradiation solid state NMR experiments. Particularly, NMR signals of the CS*- and O-intermediates in Y185F-BR were observed for the first time by this experiment. Tyr185 of the wild-type BR in helix F forms an inter-α-helical hydrogen bond with Asp212 in helix G. The replacement of Tyr185 with Phe may cause disruption of the hydrogen bond network, which in turn perturbs the dynamic structure of BR, generating elongation of the half-lives of CS*-, N- and O-intermediates. Indeed, perturbation of ^{13}C CP-MAS NMR signals of [1-^{13}C]Pro was observed by mutation of Y185F in bacteriorhodopsin.[277]

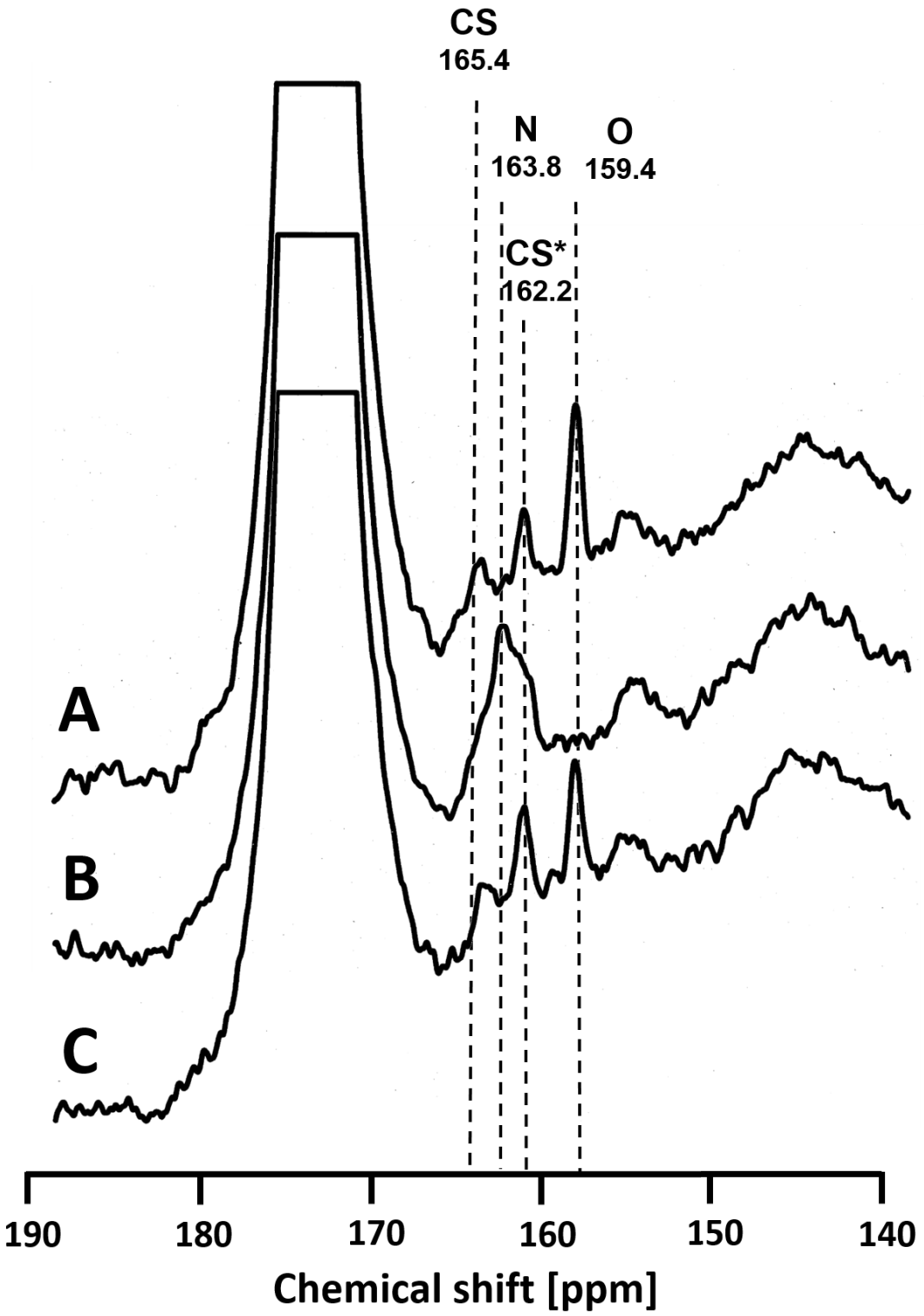

Figure 56. ^{13}C CP-MAS NMR spectra of [15-^{13}C]Ret-Y185F-BR at -40°C and 6 kHz spinning frequency under various conditions.
NMR spectra were measured (A. D2) in the dark after irradiation with 520 nm light, (B. L2) under irradiation with 520 nm light, and (C. D3) in the dark.

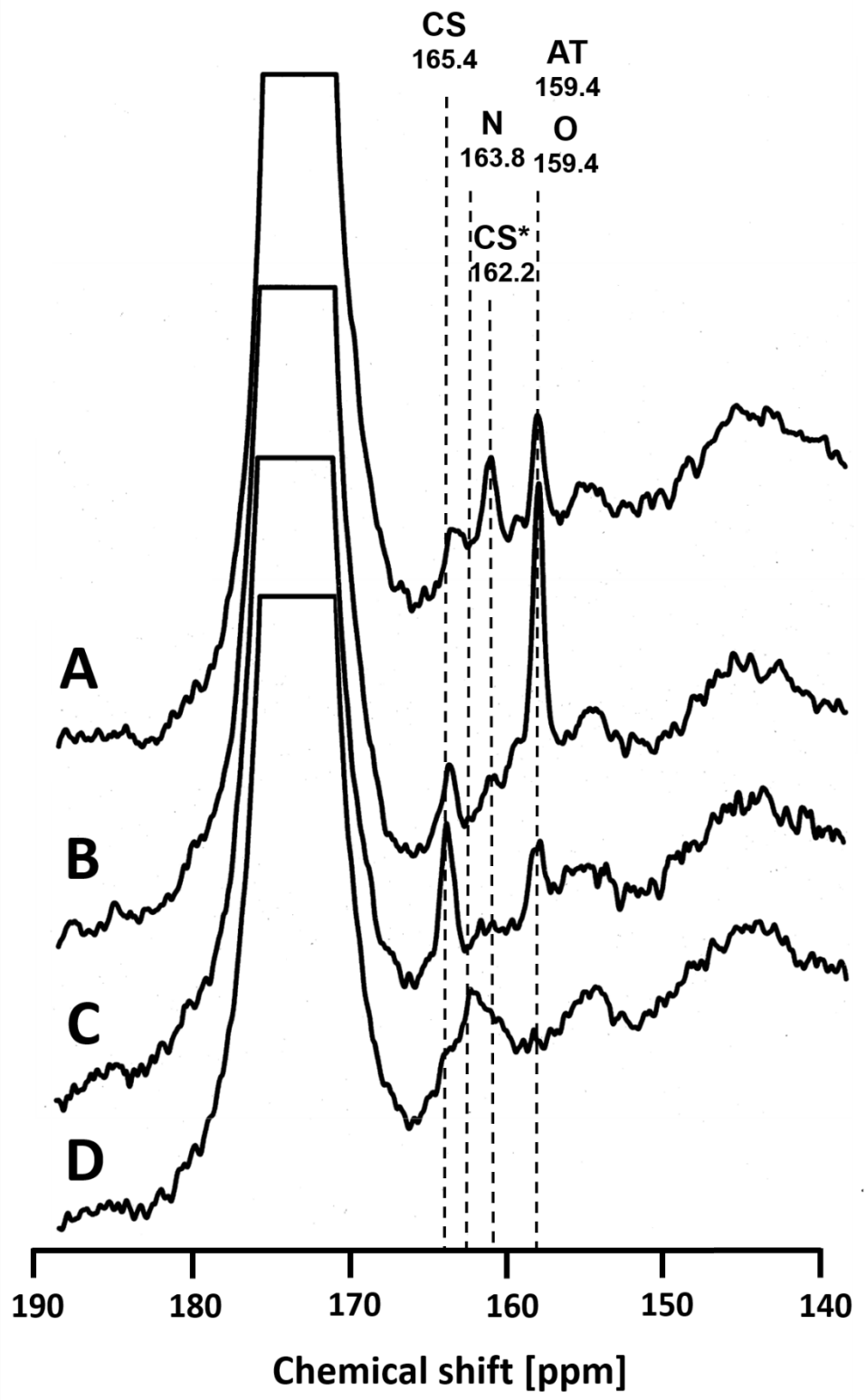

Figure 57. ^{13}C CP-MAS NMR spectra of [15-^{13}C]Ret-Y185F-BR at 6 kHz spinning frequency under various conditions.
(A) Collected at -40°C in the dark after irradiation with 520 nm light. (B) After increasing the temperature to -20°C, and collected at -40°C. (C) After increasing the temperature to 20°C, and collected at -40°C. (D) Measured the NMR spectrum at -40°C under irradiation with 520 nm light.

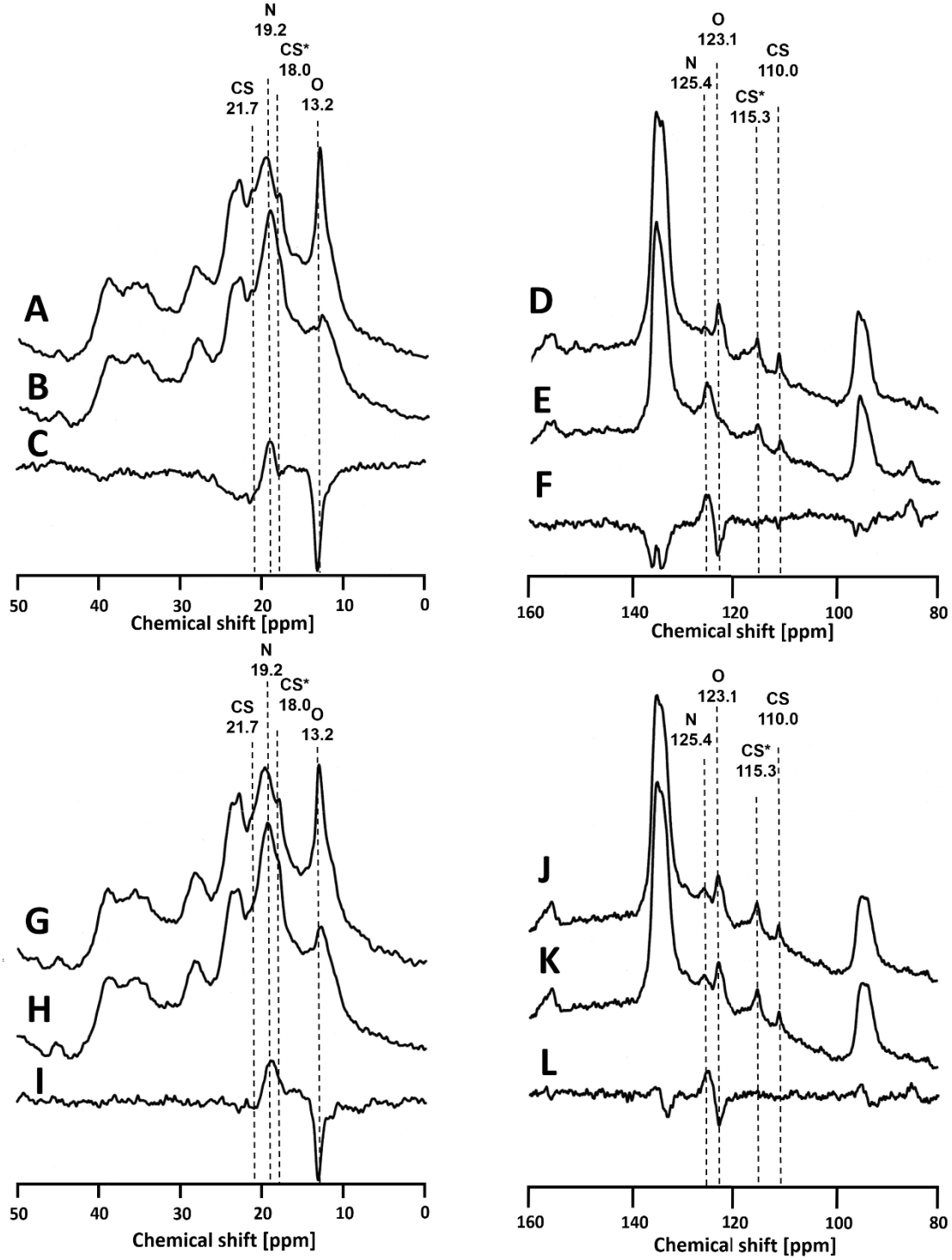

Figure 58. ^{13}C CP-MAS NMR spectra of [20-^{13}C]Ret-Y185F-BR at -40°C.
(A. D) In the dark after irradiation with 520 nm light, (B. E) under irradiation with 520 nm light, and (C, F) difference spectra (B - A) and (E - D), respectively. ^{13}C CP-MAS NMR spectra of [20-^{13}C]Ret-Y185F-BR at -40°C (G. J) in the dark after irradiation with 520 nm light, (H. K)under irradiation with 595 nm (orange) light, (I, L) difference spectra (H – G) and (K – J), respectively.

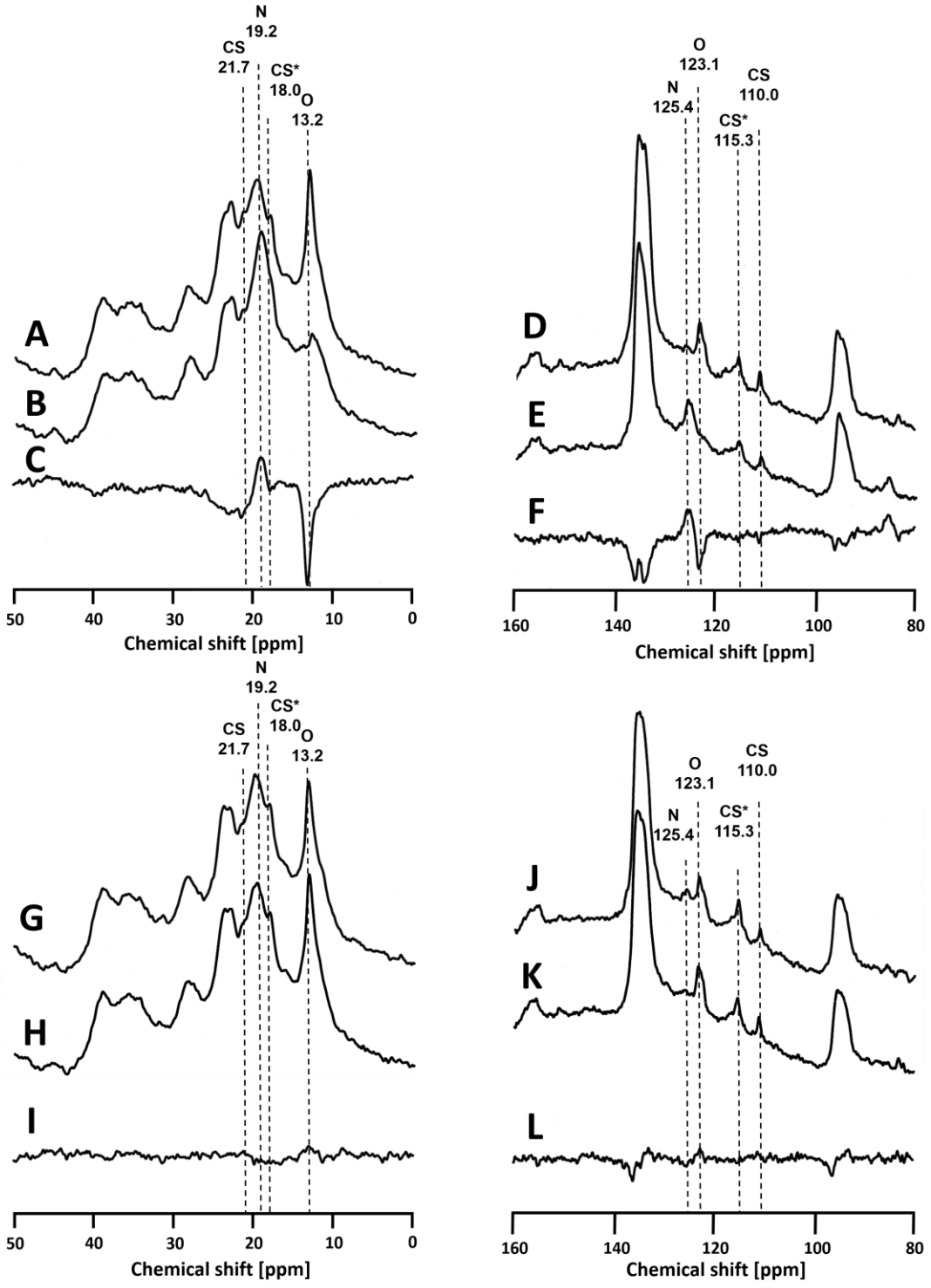

Figure 59. ^{13}C CP-MAS NMR spectra of [20-^{13}C]Ret-Y185F-BR at -40°C.
(A. D) In the dark after irradiation with 520 nm light, (B. E) under irradiation with 520 nm light, and (C, F) difference spectra (B - A) and (E - D), respectively. ^{13}C CP-MAS NMR spectra of [20-^{13}C]Ret-Y185F-BR at -40°C (G. J) in the dark after irradiation with 595 nm light, (H. K)under irradiation with 365 nm (blue) light, (I, L) difference spectra (H – G) and (K– J), respectively.

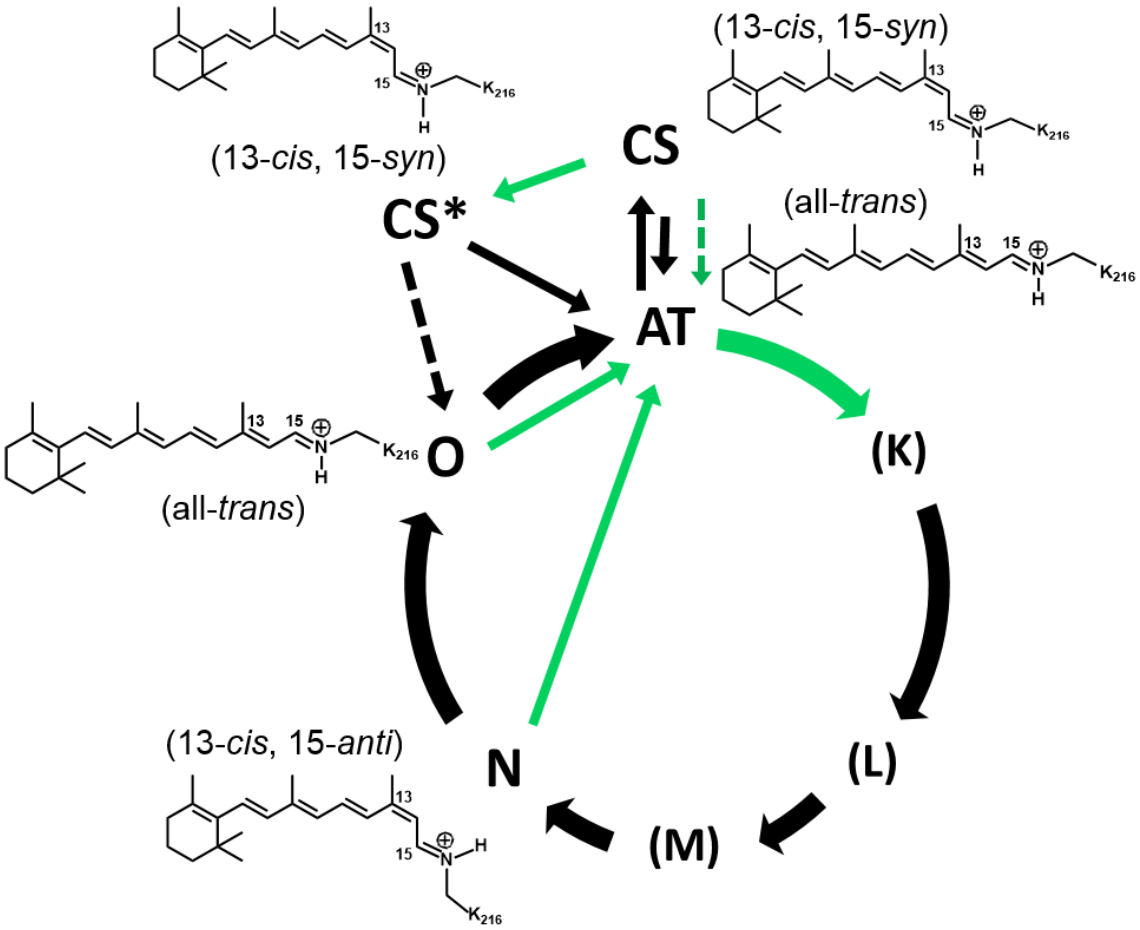

Figure 60. Photo reaction pathways of Y185F-BR.
Solid green arrows indicate photo reaction pathways under irradiation with 520 nm light. Solid black arrows indicate thermal relaxation pathways. Broken arrows indicate hypothetical pathways.

Conclusion

The photo reaction pathways of BR-WT and BR-Y185F mutant were investigated using *in situ* photo-irradiation solid-state NMR spectroscopy. In the dark-adapted state, the CS and AT states coexist at a CS : AT molar ratio of 1 : 1 in WT. The CS state is converted to the CS*-intermediate and AT state is converted to the N-intermediate under photo-irradiation with 520 nm light. Trapped CS*-intermediate is leaked to AT state in dark. Although it changed without light, this pathway was determined to be occurring by thermal relaxation. Continuous observation of CS*-intermediate also indicated the back flow to CS state which requires light irradiation. The balance of two pathways from CS*-intermediate decide the amount of leak to AT state which can be controlled by the temperature. The formation of N-intermediate was observed by irradiating the light-adapted state. The photocycle including CS*-intermediate was shown, although it differs in some part as that observed in Y185F mutant. In the dark-adapted state, the CS and AT states coexist at a CS : AT molar ratio of 3 : 1. The CS state is converted to the CS*-intermediate and the AT state is converted to the N-intermediate under photo-irradiation with 520 nm light. The CS state is also converted to the N-intermediate through the AT state under photo-irradiation with 520 nm light. In addition, the N-intermediate is converted directly to the AT state under irradiation with 520 nm light, and thus, the apparent AT photocycle appears as a double photon process: AT → N → AT, where the rate of N → AT transformation is slower than that of the AT → N-intermediate transformation. However, the N-intermediate is converted to the O-intermediate in the dark, because the half-life of the O-intermediate is longer than that of the N-intermediate at −40 °C. The O-intermediate is also directly converted to the AT state under irradiation with 520 nm light. In contrast, the O-intermediate is converted to the AT state in the thermal relaxation process at −20 °C. Furthermore, the CS* is converted to the AT state which is subsequently converted to the CS state until reaching equilibrium at 20 °C in the dark. We also examined [20-^{13}C]retinal and [14-^{13}C]retinal to determine the C13=C14 and C15=N configurations, respectively. The configurations of the AT and CS states and the CS*-, N- and O-intermediates were determined to be (13-*trans*, 15-*anti*), (13-*cis*, 15-*syn*), (13-*cis*, 15-*syn*), (13-*cis*, 15-*anti*), (13-*trans*, 15-*anti*), respectively.

Understandings about retinal-binding site

Summary

Retinal-binding site, the reaction center of rhodopsin, is an indispensable part in rhodopsin research for comprehensive understanding of mechanisms. Structures of retinal and surrounding residues at ground state and excited state provides essential interactions for ion transportation and protein structural change during photocycle.

Here, we focused on three main projects related to retinal-binding site of rhodopsins: essential conformation and interactions at retinal-binding site of *Krokinobacter* rhodopsin 2 (Chapter 2), long-distance perturbation of extracellular structure to Schiff base-counterion interaction in KR2 (Chapter 3), and track-observation of retinal conformation change from ground state to excited state observed in bacteriorhodopsin (Chapter 4).

In Chapter 2, essential interactions in retinal-binding site of KR2 were discussed since KR2 has Schiff base counterion at unique location compared to other known proton or chloride pumping rhodopsins and the mechanism of dislocating Schiff base proton and conformation of proton-accepted counterion should have been revealed. Retinal and nearby residues-labeled KR2 sample with various pH from neutral to acidic were applied to DARR experiment. From the assigned chemical shifts, torsion around Schiff base was induced because of the unique location of counterion and change of protonation state of counterion was observed. In addition, another Asp residue at the other side of retinal, Asp251, showed no change in the interaction with Tyr218 which hydrogen bond is weak compared to other rhodopsins probably because of the functionality of Asp251 which binds to sodium ion during photocycle. These information gave us new insights about unique mechanism of sodium pump.

In Chapter 3, influence of extracellular structure on selectivity in transporting ions was discussed. A light-driven Na^+ pump KR2 has additional proton pump ability in the absence of Na^+ when K^+ or larger alkali metal ions are present. Limited information is known about the proton pumping function of KR2 except that a specific mutation of H30A eliminates the proton pump ability while maintaining Na^+ pump. Alteration of bound Na^+ at the characteristic Na^+ binding site at extracellular side in KR2 to K^+ or larger ions induced the structural change of the protein. Observation at Schiff base WT and H30A mutant under alteration of the alkali metal ion revealed the bound and unbound states depending on ions in buffer. In the absence of His30 and bound ion at extracellular

binding site induced larger shift in the Schiff base peak indicating the strong electrostatic interaction and torsion around Schiff base. With the results of FTIR and flash-photolysis, we proposed a model why H30A mutant in K^+ or larger alkali metal ion lacks proton pumping function. These results suggested the hydrogen bonding network that connects between extracellular side and retinal-binding site.

In Chapter 4, retinal and protein conformation changes at photo-excited state were discussed. Bacteriorhodopsin (BR) is a rare rhodopsin of having two conformations of all-*trans*, 15-*anti* and 13-*cis*, 15-*syn* retinal at ground state with 1:1 ratio. Proton pump activity is expressed during all-*trans* photocycle where 13-*cis* retinal is converted to all-*trans* before excited to K-intermediate. Structural change was observed at retinal and Tyr backbone using *in-situ* photo-irradiated solid-state NMR. Control on temperature and light-irradiation condition enabled to trap photo-intermediates of CS* in 13-*cis* photocycle and N in all-*trans* photocycle in wild type sample. To increase the yield of CS*-intermediate, same measurements were conducted on Y185F mutant, which has higher ratio of 13-*cis* at ground state, to find the retinal conformation at CS*-intermediate to be 13-*cis*, 15-*syn*. Tyr backbone in WT showed similar signal pattern in CS*- and N-intermediates indicating the functional importance of CS*-intermediate. These results deepen the mechanistic understanding of bacteriorhodopsin and the application of this method to other rhodopsins should expand the knowledge on the unclear photocyclic process.

These works on retinal-binding site provided us some facts that crucial interactions around retinal are held at ground state to maintain the functionality and the interaction change induces structural change in protein which change was induced by conformational change of retinal. The data obtained at ground state should be base for the observation of structural change at photo-intermediates to track the structural change which should provide more detailed information on mechanism of each pumps.

References

1. Culhane, K. J., Liu, Y., Cai, Y. & Yan, E. C. Y. Transmembrane signal transduction by peptide hormones via family B G protein-coupled receptors. *Front. Pharmacol.* **6,** 1–23 (2015).
2. Nakanishi, K. Why 11-cis-Retinal? *Am. Zool.* **31,** 479–489 (2017).
3. Greene, V. & Lanyif, K. Proton Movements in Response for Sodium Ions in. *J. Biol. Chem.* **254,** 10986–10994 (1979).
4. Matsuno-Yagi, A. & Mukohata, Y. Two possible roles of bacteriorhodopsin; a comparative study of strains of Halobacterium halobium differing in pigmentation. *Biochem. Biophys. Res. Commun.* **78,** 237–243 (1977).
5. Matsuno-Yagi, A. & Mukohata, Y. ATP synthesis linked to light-dependent proton uptake in a red mutant strain of Halobacterium lacking bacteriorhodopsin. *Arch. Biochem. Biophys.* **199,** 297–303 (1980).
6. V.Lindley, E. & MacDonald, R. E. A second mechanism for sodium extrusion in Halobacterium halobium: A light-driven sodium pump. *Biochem. Biophys. Res. Commun.* **88,** 491–499 (1979).
7. Lanyi, J. K. & Weber, H. J. Spectrophotometric identification of the pigment associated with light-driven primary sodium translocation in Halobacterium halobium. *J. Biol. Chem.* **255,** 243–50 (1980).
8. Nagel, G. *et al.* Channelrhodopsin-1: A Light-Gated Proton Channel in Green Algae. *Science (80-.).* **296,** 2395–2398 (2002).
9. Balashov, S. P. Xanthorhodopsin: A Proton Pump with a Light-Harvesting Carotenoid Antenna. *Science (80-.).* **309,** 2061–2064 (2005).
10. Kato, H. E., Inoue, K., Kandori, H. & Nureki, O. The light-driven sodium ion pump: A new player in rhodopsin research. *BioEssays* **38,** 1274–1282 (2016).
11. Tsukamoto, T., Inoue, K., Kandori, H. & Sudo, Y. Thermal and spectroscopic characterization of a proton pumping rhodopsin from an extreme thermophile. *J. Biol. Chem.* **288,** 21581–21592 (2013).
12. Inoue, K. *et al.* A light-driven sodium ion pump in marine bacteria. *Nat. Commun.* **4,** 1678 (2013).
13. 土井聡子 & 須藤雄気. ビタミンAアルデヒドを発色団とするレチナールタンパク質の多様性と可能性 Diversityand potentialof the retinal proteins having vitamin−A aldehyde retinal as a chromophore. 日本ビタミン学会 83–86 (2015).
14. Racker, E. & Stoeckenius, W. Reconstitution of Purple Membrane Vesicles Catalyzing Light-driven Proton Uptake and Adenosine Triphosphate Formation. *J. Biol. Chem.* **249,** 662–663 (1974).

15. Kayushin, L. P. & Skulachev, V. P. Bacteriorhodopsin as an electrogenic proton pump: Reconstitution of bacteriorhodopsin proteoliposomes generating Δψ and ΔpH. *FEBS Lett.* **39,** 39–42 (1974).
16. Facciotti, M. T., Rouhani-Manshadi, S. & Glaeser, R. M. Energy transduction in transmembrane ion pumps. *Trends Biochem. Sci.* **29,** 445–451 (2004).
17. Oesterhelt, D. & Stoeckenius, W. Functions of a New Photoreceptor Membrane. *Proc. Natl. Acad. Sci.* **70,** 2853–2857 (1973).
18. Blaurock, A. E. & Stoeckenius, W. Structure of the Purple Membrane. *Nat. New Biol.* **233,** 152–155 (1971).
19. Yamashita, H. *et al.* Role of trimer–trimer interaction of bacteriorhodopsin studied by optical spectroscopy and high-speed atomic force microscopy. *J. Struct. Biol.* **184,** 2–11 (2013).
20. Oesterhelt, D. & Stoeckenius, W. Rhodopsin-like Protein from the Purple Membrane of Halobacterium halobium. *Nat. New Biol.* **233,** 149–152 (1971).
21. Luecke, H., Schobert, B., Richter, H.-T., Cartailler, J.-P. & Lanyi, J. K. Structure of bacteriorhodopsin at 1.55 Å resolution. *J. Mol. Biol.* **291,** 899–911 (1999).
22. Oesterhelt, D., Meentzen, M. & Schuhmann, L. Reversible Dissociation of the Purple Complex in Bacteriorhodopsin and Identification of 13-cis and all-trans-Retinal as its Chromophores. *Eur. J. Biochem.* **40,** 453–463 (1973).
23. Mowery, P. C. & Stoeckenius, W. Photoisomerization of the chromophore in bacteriorhodopsin during the proton pumping photocycle. *Biochemistry* **20,** 2302–2306 (1981).
24. Luecke, H. *et al.* Coupling photoisomerization of retinal to directional transport in bacteriorhodopsin. *J. Mol. Biol.* **300,** 1237–1255 (2000).
25. Henderson, R. & Unwin, P. N. T. Three-dimensional model of purple membrane obtained by electron microscopy. *Nature* **257,** 28–32 (1975).
26. Subramaniam, S. & Henderson, R. Molecular mechanism of vectorial proton translocation by bacteriorhodopsin. *Nature* **406,** 653–657 (2000).
27. Grigorieff, N., Ceska, T. A., Downing, K. H., Baldwin, J. M. & Henderson, R. Electron-crystallographic Refinement of the Structure of Bacteriorhodopsin. *J. Mol. Biol.* **259,** 393–421 (1996).
28. Pebay-Peyroula, E. X-ray Structure of Bacteriorhodopsin at 2.5 Angstroms from Microcrystals Grown in Lipidic Cubic Phases. *Science (80-.).* **277,** 1676–1681 (1997).
29. Royant, A. *et al.* Helix deformation is coupled to vectorial proton transport in the photocycle of bacteriorhodopsin. *Nature* **406,** 645–648 (2000).
30. Freier, E., Wolf, S. & Gerwert, K. Proton transfer via a transient linear water-molecule chain in a membrane protein. *Proc. Natl. Acad. Sci.* **108,** 11435–11439 (2011).
31. Grudinin, S., Büldt, G., Gordeliy, V. & Baumgaertner, A. Water Molecules and Hydrogen-

Bonded Networks in Bacteriorhodopsin—Molecular Dynamics Simulations of the Ground State and the M-Intermediate. *Biophys. J.* **88,** 3252–3261 (2005).

32. Tanimoto, T., Furutani, Y. & Kandori, H. Structural Changes of Water in the Schiff Base Region of Bacteriorhodopsin: Proposal of a Hydration Switch Model. *Biochemistry* **42,** 2300–2306 (2003).
33. Nishikawa, T., Murakami, M. & Kouyama, T. Crystal structure of the 13-cis isomer of bacteriorhodopsin in the dark-adapted state. *J. Mol. Biol.* **352,** 319–328 (2005).
34. Patzelt, H. *et al.* The structures of the active center in dark-adapted bacteriorhodopsin by solution-state NMR spectroscopy. *Proc. Natl. Acad. Sci.* **99,** 9765–9770 (2002).
35. Rothschild, K. J. Ftir difference spectroscopy of bacteriorhodopsin - toward a molecular-model. *J. Bioenerg. Biomembr.* **24,** 147–167 (1992).
36. Mathies, R. A., Lin, S. W., Ames, J. B. & Pollard, W. T. From femtoseconds to biology: mechanism of bacteriorhodopsin's light-driven proton pump. *Annu. Rev. Biophys. Biophys. Chem.* **20,** 419–518 (1991).
37. Lanyi, J. K. Proton translocation mechanism and energetics in the light-driven pump bacteriorhodopsin. *Biochim. Biophys. Acta* **1183,** 241–261 (1993).
38. Edman, K. *et al.* High-resolution X-ray structure of an early intermediate in the bacteriorhodopsin photocycle Karl. *Nature* **401,** 822–826 (1999).
39. Haupts, U. & Oesterhelt, D. CLOSING IN ON BACTERIORHODOPSIN : Progress in Understanding the Molecule. *Annu. Rev. Biophys. Biomol. Struct.* **28,** 367–399 (1999).
40. Lanyi, J. K. Proton transfers in the bacteriorhodopsin photocycle. *Biochim. Biophys. Acta - Bioenerg.* **1757,** 1012–1018 (2006).
41. Subramaniam, S. *et al.* Protein conformational changes in the bacteriorhodopsin photocycle. *J. Mol. Biol.* **287,** 145–161 (1999).
42. Schobert, B., Cupp-Vickery, J., Hornak, V., Smith, S. O. & Lanyi, J. K. Crystallographic Structure of the K Intermediate of Bacteriorhodopsin: Conservation of Free Energy after Photoisomerization of the Retinal. *J. Mol. Biol.* **321,** 715–726 (2002).
43. Matsui, Y. *et al.* Specific Damage Induced by X-ray Radiation and Structural Changes in the Primary Photoreaction of Bacteriorhodopsin. *J. Mol. Biol.* **324,** 469–481 (2002).
44. Kandori, H. *et al.* Tight Asp-85-Thr-89 association during the pump switch of bacteriorhodopsin. *Proc. Natl. Acad. Sci.* **98,** 1571–1576 (2001).
45. Lanyi, J. K. & Schobert, B. Crystallographic Structure of the Retinal and the Protein after Deprotonation of the Schiff Base : The Switch in the Bacteriorhodopsin Photocycle. *J. Mol. Biol.* **321,** 727–737 (2002).
46. Hu, J. G., Sun, B. Q., Petkova, A. T., Griffin, R. G. & Herzfeld, J. The Predischarge Chromophore in Bacteriorhodopsin: A 15 N Solid-State NMR Study of the L Photointermediate.

Biochemistry **36,** 9316–9322 (1997).

47. Kandori, H. *et al.* Water-Mediated Proton Transfer in Proteins: An FTIR Study of Bacteriorhodopsin. *J. Am. Chem. Soc.* **117,** 2118–2119 (1995).
48. Maeda, A. *et al.* Intramembrane and Carboxyl Signaling Mediated by Hydrog Groups in Bacteriorhodopsi n and Rhodopsin '. *J. Biochem.* **121,** 399–406 (1997).
49. Yamazaki, Y. *et al.* Hydrogen Bonds of Water and CO Groups Coordinate Long-Range Structural Changes in the L Photointermediate of Bacteriorhodopsin. *Biochemistry* **35,** 4063–4068 (1996).
50. Yamazaki, Y. *et al.* Water Structural Changes at the Proton Uptake Site (the Thr46-Asp96 Domain) in the L Intermediate of Bacteriorhodopsin. *Biochemistry* **34,** 7088–7093 (1995).
51. Maeda, A. *et al.* Interaction of tryptophan-182 with the retinal 9-methyl group in the L intermediate of bacteriorhodopsin. *Biochemistry* **34,** 577–582 (1995).
52. Lanyi, J. K. & Schobert, B. Structural Changes in the L Photointermediate of Bacteriorhodopsin. *J Mol Biol.* **365,** 1379–1392 (2007).
53. Kouyama, T., Nishikawa, T., Tokuhisa, T. & Okumura, H. Crystal Structure of the L Intermediate of Bacteriorhodopsin: Evidence for Vertical Translocation of a Water Molecule during the Proton Pumping Cycle. *J. Mol. Biol.* **335,** 531–546 (2004).
54. Hendrickson, F. M., Burkard, F. & Glaeser, R. M. Structural characterization of the L-to-M transition of the bacteriorhodopsin photocycle. *Biophys. J.* **75,** 1446–1454 (1998).
55. Brown, L. S. & Lanyi, J. K. Determination of the transiently lowered pKa of the retinal Schiff base during the photocycle of bacteriorhodopsin. *Proc. Natl. Acad. Sci.* **93,** 1731–1734 (1996).
56. Govindjee, R. *et al.* Lowering the intrinsic pKa of the chromophore's Schiff base can restore its light-induced deprotonation in the inactive Tyr-57 -> Asn mutant of bacteriorhodopsin. *J. Biol. Chem.* **269,** 14353–14354 (1994).
57. Braiman, M. S., Dioumaev, A. K. & Lewis, J. R. A large photolysis-induced pKa increase of the chromophore counterion in bacteriorhodopsin: implications for ion transport mechanisms of retinal proteins. *Biophys. J.* **70,** 939–947 (1996).
58. Rousso, I., Brodsky, I., Lewis, A. & Sheves, M. The role of water in retinal complexation to bacterio-opsin. *Journal of Biological Chemistry* **270,** 13860–13868 (1995).
59. Lanyi, J. K. & Schobert, B. Mechanism of Proton Transport in Bacteriorhodopsin from Crystallographic Structures of the K, L, M1, M2, and M2′ Intermediates of the Photocycle. *J. Mol. Biol.* **328,** 439–450 (2003).
60. Maeda, A., Sasaki, J., Ohkita, Y. J., Simpson, M. & Herzfeld, J. Tryptophan Perturbation in the L Intermediate of Bacteriorhodopsin: Fourier Transform Infrared Analysis with Indole-15N Shift. *Biochemistry* **31,** 12543–12545 (1992).
61. Wu, S., Chang, Y., Marti, T., Mogi, T. & Khoranat, H. G. Effects of tryptophan mutation on the deprotonation and reprotonation kinetics of the Schiff base during the photocycle of

bacteriorhodopsin. **61,** 1281–1288 (1992).

62. Kaulen, A. D. Electrogenic processes and protein conformational changes accompanying the bacteriorhodopsin photocycle. *Biochim. Biophys. Acta - Bioenerg.* **1460,** 204–219 (2000).
63. Takeda, K. *et al.* Crystal Structure of the M Intermediate of Bacteriorhodopsin: Allosteric Structural Changes Mediated by Sliding Movement of a Transmembrane Helix. *J. Mol. Biol.* **341,** 1023–1037 (2004).
64. Sass, H. J. *et al.* Structural alterations for proton translocation in the M state of wild-type bacteriorhodopsin. *Nature* **406,** 649–653 (2000).
65. Balashov, S. P., Imasheva, E. S., Govindjee, R. & Ebrey, T. G. Titration of aspartate-85 in bacteriorhodopsin: What it says about chromophore isomerization and proton release. *Biophys. J.* **70,** 473–481 (1996).
66. Richter, H. T., Brown, L. S., Needleman, R. & Lanyi, J. K. A linkage of the pK(a)'s of asp-85 and glu-204 forms part of the reprotonation switch of bacteriorhodopsin. *Biochemistry* **35,** 4054–4062 (1996).
67. Luecke, H. Structural Changes in Bacteriorhodopsin During Ion Transport at 2 Angstrom Resolution. *Science (80-.).* **286,** 255–260 (1999).
68. Hu, J. G. *et al.* Early and late M intermediates in the bacteriorhodopsin photocycle: A solid-state NMR study. *Biochemistry* **37,** 8088–8096 (1998).
69. Lansing, J. C. *et al.* Chromophore distortions in the bacteriorhodopsin photocycle: Evolution of the H-C14-C15-H dihedral angle measured by solid-state NMR. *Biochemistry* **41,** 431–438 (2002).
70. Gerwert, K., Hess, B., Soppa, J. & Oesterhelt, D. Role of aspartate-96 in proton translocation by bacteriorhodopsin. *Proc. Natl. Acad. Sci. U. S. A.* **86,** 4943–4947 (1989).
71. Sasaki, J., Shichida, Y., Lanyi, J. K. & Maeda, A. Protein changes associated with reprotonation of the Schiff base in the photocycle of Asp96→Asn bacteriorhodopsin. The M(N) intermediate with unprotonated Schiff base but N-like protein structure. *J. Biol. Chem.* **267,** 20782–20786 (1992).
72. Vonck, J. A three-dimensional difference map of the N intermediate in the bacteriorhodopsin photocycle: Part of the F helix tilts in the M to N transition. *Biochemistry* **35,** 5870–5878 (1996).
73. Rothschild, K. J. *et al.* Vibrational Spectroscopy of Bacteriorhodopsin Mutants: Evidence for the Interaction of Proline-186 with the Retinylidene Chromophore. *Biochemistry* **29,** 5954–5960 (1990).
74. Ahl, P. L., Stern, L. J., Mogi, T., Khorana, H. G. & Rothschild, K. J. Substitution of Amino Acids in Helix F of Bacteriorhodopsin: Effects on the Photochemical Cycle. *Biochemistry* **28,** 10028–10034 (1989).
75. Rothschild, K. J., He, Y.-W., Sonar, S., Marti, T. & Khorana, H. G. Vibrational Spectroscopy of

Bacteriorhodopsin Mutants. *J. Biol. Chem.* **265,** 16965–16991 (1990).

76. Ludlam, C. F. C. *et al.* Site-Directed Isotope Labeling and ATR-FTIR Difference Spectroscopy of Bacteriorhodopsin: The PeptiDe Carbonyl Group of Tyr 185 Is Structurally Active During the bR → N Transition. *Biochemistry* **34,** 2–6 (1995).
77. Schobert, B., Brown, L. S. & Lanyi, J. K. Crystallographic structures of the M and N intermediates of bacteriorhodopsin: Assembly of a hydrogen-bonded chain of water molecules between Asp-96 and the retinal Schiff base. *J. Mol. Biol.* **330,** 553–570 (2003).
78. Yamazaki, Y., Kandori, H., Needleman, R., Lanyi, J. K. & Maeda, A. Interaction of the protonated schiff base with the peptide backbone of valine 49 and the intervening water molecule in the N photointermediate of bacteriorhodopsin. *Biochemistry* **37,** 1559–1564 (1998).
79. Chen, D. & Lanyi, J. K. Structural changes in the N and N′ states of the bacteriorhodopsin photocycle. *Biophys. J.* **96,** 2779–2788 (2009).
80. Kamikubo, H. *et al.* Structure of the N intermediate of bacteriorhodopsin revealed by x-ray diffraction. *Proc. Natl. Acad. Sci.* **93,** 1386–1390 (1996).
81. Dencher, N. A., Dresselhaus, D., Zaccai, G. & Büldt, G. Structural changes in bacteriorhodopsin during proton translocation revealed by neutron diffraction. *Proc. Natl. Acad. Sci.* **86,** 7876–7879 (1989).
82. Subramaniam, S., Gerstein, M., Oesterhelt, D. & Henderson, R. Electron diffraction analysis of structural changes in the photocycle of bacteriorhodopsin. *EMBO J.* **12,** 1–8 (1993).
83. Rouhani, S. *et al.* Crystal Structure of the D85S Mutant of Bacteriorhodopsin : Model of an O-like Photocycle Intermediate. *J. Mol. Biol.* **313,** 615–628 (2001).
84. Morgan, J. E. *et al.* Structure Changes upon Deprotonation of the Proton Release Group in the Bacteriorhodopsin Photocycle. *Biophys. J.* **103,** 444–452 (2012).
85. Zhang, J. *et al.* Crystal structure of the O intermediate of the Leu93→Ala mutant of bacteriorhodopsin. *Proteins Struct. Funct. Bioinforma.* **80,** 2384–2396 (2012).
86. Tóth-Boconádi, R., Keszthelyi, L. & Stoeckenius, W. Photoexcitation of the O-intermediate in bacteriorhodopsin mutant L93A. *Biophys. J.* **84,** 3857–3863 (2003).
87. Subramaniam, S., Greenhalgh, D. a, Rath, P., Rothschild, K. J. & Khorana, H. G. Replacement of leucine-93 by alanine or threonine slows down the decay of the N and O intermediates in the photocycle of bacteriorhodopsin: implications for proton uptake and 13-cis-retinal----all-trans-retinal reisomerization. *Proc. Natl. Acad. Sci. U. S. A.* **88,** 6873–6877 (1991).
88. Luecke, H., Schobert, B., Richter, H. T., Cartailler, J. P. & Lanyi, J. K. Structure of bacteriorhodopsin at 1.55 A resolution. *J. Mol. Biol.* **291,** 899–911 (1999).
89. Sudo, Y. *et al.* Characterization of a signaling complex composed of sensory rhodopsin I and its cognate transducer protein from the eubacterium Salinibacter ruber. *Biochemistry* **48,** 10136–10145 (2009).

90. Shimono, K., Ikeura, Y., Sudo, Y., Iwamoto, M. & Kamo, N. Environment around the chromophore in pharaonis phoborhodopsin: mutation analysis of the retinal binding site. *Biochim. Biophys. Acta - Biomembr.* **1515,** 92–100 (2001).

91. Hsu, M.-F. *et al.* Structural and Functional Studies of a Newly Grouped Haloquadratum walsbyi Bacteriorhodopsin Reveal the Acid-resistant Light-driven Proton Pumping Activity. *J. Biol. Chem.* **290,** 29567–29577 (2015).

92. Sudo, Y. *et al.* A Microbial rhodopsin with a unique retinal composition shows both sensory rhodopsin II and bacteriorhodopsin-like properties. *J. Biol. Chem.* **286,** 5967–5976 (2011).

93. Inoue, K. *et al.* Absorption Spectra and Photochemical Reactions in a Unique Photoactive Protein, Middle Rhodopsin MR. *J. Phys. Chem. B* **116,** 5888–5899 (2012).

94. Kalisky, O., Goldschmidt, C. R. & Ottolenghi, M. On the photocycle and light adaptation of dark-adapted bacteriorhodopsin. *Biophys. J.* **19,** 185–189 (1977).

95. Logunov, I., Humphrey, W., Schulten, K. & Sheves, M. Molecular dynamics study of the 13-cis form (bR548) of bacteriorhodopsin and its photocycle. *Biophys. J.* **68,** 1270–1282 (1995).

96. Kandori, H. Ion-pumping microbial rhodopsins. *Front. Mol. Biosci.* **2,** 52 (2015).

97. Enami, N. *et al.* Crystal Structures of Archaerhodopsin-1 and -2: Common Structural Motif in Archaeal Light-driven Proton Pumps. *J. Mol. Biol.* **358,** 675–685 (2006).

98. Yoshimura, K. & Kouyama, T. Structural Role of Bacterioruberin in the Trimeric Structure of Archaerhodopsin-2. *J. Mol. Biol.* **375,** 1267–1281 (2008).

99. Kouyama, T. *et al.* Structure of archaerhodopsin-2 at 1.8 Å resolution. *Acta Crystallogr. Sect. D Biol. Crystallogr.* **70,** 2692–2701 (2014).

100. Tsukamoto, T. *et al.* X-ray Crystallographic Structure of Thermophilic Rhodopsin. *J. Biol. Chem.* **291,** 12223–12232 (2016).

101. Tsukamoto, T., Demura, M. & Sudo, Y. Irreversible trimer to monomer transition of thermophilic rhodopsin upon thermal stimulation. *J. Phys. Chem. B* **118,** 12383–12394 (2014).

102. Shastri, S. *et al.* Proteorhodopsin: Characterisation of 2D crystals by electron microscopy and solid state NMR. *Biochim. Biophys. Acta - Biomembr.* **1768,** 3012–3019 (2007).

103. Mehler, M. *et al.* Chromophore Distortions in Photointermediates of Proteorhodopsin Visualized by Dynamic Nuclear Polarization-Enhanced Solid-State NMR. *J. Am. Chem. Soc.* **139,** 16143–16153 (2017).

104. Mao, J. *et al.* Structural Basis of the Green–Blue Color Switching in Proteorhodopsin as Determined by NMR Spectroscopy. *J. Am. Chem. Soc.* **136,** 17578–17590 (2014).

105. Vogt, A., Wietek, J. & Hegemann, P. Gloeobacter Rhodopsin, Limitation of Proton Pumping at High Electrochemical Load. *Biophys. J.* **105,** 2055–2063 (2013).

106. Tsukamoto, T. *et al.* Salt bridge in the conserved His-Asp cluster in Gloeobacter rhodopsin contributes to trimer formation. *FEBS Lett.* **587,** 322–327 (2013).

107. Bertsova, Y. V, Bogachev, A. V & Skulachev, V. P. Proteorhodopsin from Dokdonia sp. PRO95 is a light-driven Na+-pump. *Biochem.* **80,** 449–454 (2015).

108. Kajimoto, K. *et al.* Transient Resonance Raman Spectroscopy of a Light-Driven Sodium-Ion-Pump Rhodopsin from Indibacter alkaliphilus. *J. Phys. Chem. B* **121,** 4431–4437 (2017).

109. Ernst, O. P. *et al.* Microbial and Animal Rhodopsins : Structures, Functions, and Molecular Mechanisms. *Chem. Rev.* **114,** 126–163 (2014).

110. Wang, W. *et al.* Tuning the Electronic Absorption of Protein-Embedded All-trans-Retinal. *Science (80-.).* **338,** 1340–1343 (2012).

111. Sudo, Y. *et al.* A blue-shifted light-driven proton pump for neural silencing. *J. Biol. Chem.* **288,** 20624–20632 (2013).

112. Karasuyama, M., Inoue, K., Kandori, H. & Takeuchi, I. Toward Machine Learning-based Data-driven Functional Protein Studies: Understanding Colour Tuning Rules and Predicting the Absorption Wavelengths of Microbial Rhodopsins. *bioRxiv* (2017). doi:10.1101/226118

113. Inoue, K., Nomura, Y. & Kandori, H. Asymmetric Functional Conversion of Eubacterial Light-driven Ion Pumps. *J. Biol. Chem.* **291,** 9883–9893 (2016).

114. Inoue, K. *et al.* Converting a Light-Driven Proton Pump into a Light-Gated Proton Channel. *J. Am. Chem. Soc.* **137,** 3291–3299 (2015).

115. Sasaki, J. *et al.* Conversion of bacteriorhodopsin into a chloride ion pump. *Science (80-.).* **269,** 73–75 (1995).

116. Wietek, J. *et al.* Conversion of channelrhodopsin into a light-gated chloride channel. *Science (80-.).* **344,** 409–412 (2014).

117. Berndt, A., Lee, S. Y., Ramakrishnan, C. & Deisseroth, K. Structure-guided transformation of channelrhodopsin into a light-activated chloride channel. *Science* **344,** 420–424 (2014).

118. Sudo, Y. & Spudich, J. L. Three strategically placed hydrogen-bonding residues convert a proton pump into a sensory receptor. *Proc. Natl. Acad. Sci.* **103,** 16129–16134 (2006).

119. Boyden, E. S., Zhang, F., Bamberg, E., Nagel, G. & Deisseroth, K. Millisecond-timescale, genetically targeted optical control of neural activity. *Nat. Neurosci.* **8,** 1263–1268 (2005).

120. Yizhar, O., Fenno, L. E., Davidson, T. J., Mogri, M. & Deisseroth, K. Optogenetics in Neural Systems. *Neuron* **71,** 9–34 (2011).

121. Fenno, L., Yizhar, O. & Deisseroth, K. The development and application of optogenetics. *Annu. Rev. Neurosci.* **34,** 389–412 (2011).

122. Zhang, F., Wang, L. P., Boyden, E. S. & Deisseroth, K. Channelrhodopsin-2 and optical control of excitable cells. *Nat. Methods* **3,** 785–792 (2006).

123. Nagel, G. *et al.* Light activation of Channelrhodopsin-2 in excitable cells of caenorhabditis elegans triggers rapid behavioral responses. *Curr. Biol.* **15,** 2279–2284 (2005).

124. Ishizuka, T., Kakuda, M., Araki, R. & Yawo, H. Kinetic evaluation of photosensitivity in

genetically engineered neurons expressing green algae light-gated channels. *Neurosci. Res.* **54,** 85–94 (2006).

125. Bi, A. *et al.* Ectopic Expression of a Microbial-Type Rhodopsin Restores Visual Responses in Mice with Photoreceptor Degeneration. *Neuron* **50,** 23–33 (2006).
126. Arenkiel, B. R. *et al.* In Vivo Light-Induced Activation of Neural Circuitry in Transgenic Mice Expressing Channelrhodopsin-2. *Neuron* **54,** 205–218 (2007).
127. Tomita, H. *et al.* Restoration of visual response in aged dystrophic RCS rats using AAV-mediated channelopsin-2 gene transfer. *Investig. Ophthalmol. Vis. Sci.* **48,** 3821–3826 (2007).
128. Douglass, A. D., Kraves, S., Deisseroth, K., Schier, A. F. & Engert, F. Escape Behavior Elicited by Single, Channelrhodopsin-2-Evoked Spikes in Zebrafish Somatosensory Neurons. *Curr. Biol.* **18,** 1133–1137 (2008).
129. Han, X. *et al.* Millisecond-Timescale Optical Control of Neural Dynamics in the Nonhuman Primate Brain. *Neuron* **62,** 191–198 (2009).
130. Berndt, A. *et al.* High-efficiency channelrhodopsins for fast neuronal stimulation at low light levels. *Proc. Natl. Acad. Sci.* **108,** 7595–7600 (2011).
131. Yizhar, O. *et al.* Neocortical excitation/inhibition balance in information processing and social dysfunction. *Nature* **477,** 171–178 (2011).
132. Gunaydin, L. A. *et al.* Ultrafast optogenetic control. *Nat. Neurosci.* **13,** 387–392 (2010).
133. Berndt, A., Yizhar, O., Gunaydin, L. A., Hegemann, P. & Deisseroth, K. Bi-stable neural state switches. *Nat. Neurosci.* **12,** 229–234 (2009).
134. Kleinlogel, S. *et al.* Ultra light-sensitive and fast neuronal activation with the Ca2+-permeable channelrhodopsin CatCh. *Nat. Neurosci.* **14,** 513–518 (2011).
135. Wen, L. *et al.* Opto-current-clamp actuation of cortical neurons using a strategically designed channelrhodopsin. *PLoS One* **5,** e12893 (2010).
136. Lin, J. Y., Lin, M. Z., Steinbach, P. & Tsien, R. Y. Characterization of engineered channelrhodopsin variants with improved properties and kinetics. *Biophys. J.* **96,** 1803–1814 (2009).
137. Wang, H. *et al.* Molecular determinants differentiating photocurrent properties of two channelrhodopsins from Chlamydomonas. *J. Biol. Chem.* **284,** 5685–5696 (2009).
138. Yamamoto, K. *et al.* Chronic Optogenetic Activation Augments Aβ Pathology in a Mouse Model of Alzheimer Disease. *Cell Rep.* **11,** 859–865 (2015).
139. Zhang, F. & Tzanakakis, E. S. Optogenetic regulation of insulin secretion in pancreatic β-cells. *Sci. Rep.* **7,** 9357 (2017).
140. Ohkawa, N. *et al.* Artificial association of pre-stored information to generate a qualitatively new memory. *Cell Rep.* **11,** 261–269 (2015).
141. Sasaki, T. *et al.* Application of an optogenetic byway for perturbing neuronal activity via glial

photostimulation. *Proc. Natl. Acad. Sci.* **109,** 20720–20725 (2012).

142. Kato, H. E. *et al.* Crystal structure of the channelrhodopsin light-gated cation channel. *Nature* **482,** 369–374 (2012).
143. Müller, M., Bamann, C., Bamberg, E. & Kühlbrandt, W. Projection structure of channelrhodopsin-2 at 6 Å resolution by electron crystallography. *J. Mol. Biol.* **414,** 86–95 (2011).
144. Zhang, F. *et al.* Multimodal fast optical interrogation of neural circuitry. *Nature* **446,** 633–639 (2007).
145. Chow, B. Y. *et al.* High-performance genetically targetable optical neural silencing by light-driven proton pumps. *Nature* **463,** 98–102 (2010).
146. Warschawski, D. E. *et al.* Choosing membrane mimetics for NMR structural studies of transmembrane proteins. *Biochim. Biophys. Acta - Biomembr.* **1808,** 1957–1974 (2011).
147. Walde, P., Cosentino, K., Engel, H. & Stano, P. Giant Vesicles: Preparations and Applications. *ChemBioChem* **11,** 848–865 (2010).
148. Shi, L., Kawamura, I., Jung, K.-H., Brown, L. S. & Ladizhansky, V. Conformation of a Seven-Helical Transmembrane Photosensor in the Lipid Environment. *Angew. Chemie Int. Ed.* **50,** 1302–1305 (2011).
149. Wang, S. *et al.* Solid-state NMR spectroscopy structure determination of a lipid-embedded heptahelical membrane protein. *Nat. Methods* **10,** 1007–1012 (2013).
150. Wang, S. *et al.* Solid-state NMR 13C and 15N resonance assignments of a seven-transmembrane helical protein Anabaena Sensory Rhodopsin. *Biomol. NMR Assign.* **7,** 253–256 (2013).
151. Takegoshi, K., Nakamura, S. & Terao, T. 13C–1H dipolar-driven 13C–13C recoupling without 13C rf irradiation in nuclear magnetic resonance of rotating solids. *J. Chem. Phys.* **118,** 2325–2341 (2003).
152. Takegoshi, K., Nakamura, S. & Terao, T. 13C–1H dipolar-assisted rotational resonance in magic-angle spinning NMR. *Chem. Phys. Lett.* **344,** 631–637 (2001).
153. Morcombe, C. R., Gaponenko, V., Byrd, R. A. & Zilm, K. W. Diluting Abundant Spins by Isotope Edited Radio Frequency Field Assisted Diffusion. *J. Am. Chem. Soc.* **126,** 7196–7197 (2004).
154. Bax, A. & Ikura, M. An efficient 3D NMR technique for correlating the proton and15N backbone amide resonances with the α-carbon of the preceding residue in uniformly15N/13C enriched proteins. *J. Biomol. NMR* **1,** 99–104 (1991).
155. Grzesiek, S. & Bax, A. Improved 3D triple-resonance NMR techniques applied to a 31 kDa protein. *J. Magn. Reson.* **96,** 432–440 (1992).
156. Pauli, J., Baldus, M., van Rossum, B., de Groot, H. & Oschkinat, H. Backbone and Side-Chain13C and15N Signal Assignments of the α-Spectrin SH3 Domain by Magic Angle Spinning

Solid-State NMR at 17.6 Tesla. *ChemBioChem* **2,** 272–281 (2001).

157. Li, Y., Berthold, D. A., Frericks, H. L., Gennis, R. B. & Rienstra, C. M. Partial 13C and15N Chemical-Shift Assignments of the Disulfide-Bond-Forming Enzyme DsbB by 3D Magic-Angle Spinning NMR Spectroscopy. *ChemBioChem* **8,** 434–442 (2007).
158. Kawanabe, A., Furutani, Y., Jung, K. H. & Kandori, H. Photochromism of Anabaena sensory rhodopsin. *J. Am. Chem. Soc.* **129,** 8644–8649 (2007).
159. Higman, V. A. *et al.* The Conformation of Bacteriorhodopsin Loops in Purple Membranes Resolved by Solid-State MAS NMR Spectroscopy. *Angew. Chemie Int. Ed.* **50,** 8432–8435 (2011).
160. Franks, T. W., Kloepper, K. D., Wylie, B. J. & Rienstra, C. M. Four-dimensional heteronuclear correlation experiments for chemical shift assignment of solid proteins. *J. Biomol. NMR* **39,** 107–131 (2007).
161. Shen, Y., Delaglio, F., Cornilescu, G. & Bax, A. TALOS+: A hybrid method for predicting protein backbone torsion angles from NMR chemical shifts. *J. Biomol. NMR* **44,** 213–223 (2009).
162. Mak-Jurkauskas, M. L. *et al.* Energy transformations early in the bacteriorhodopsin photocycle revealed by DNP-enhanced solid-state NMR. *Proc. Natl. Acad. Sci.* **105,** 883–888 (2008).
163. Bajaj, V. S., Mak-Jurkauskas, M. L., Belenky, M., Herzfeld, J. & Griffin, R. G. Functional and shunt states of bacteriorhodopsin resolved by 250 GHz dynamic nuclear polarization-enhanced solid-state NMR. *Proc. Natl. Acad. Sci.* **106,** 9244–9249 (2009).
164. Rosay, M. *et al.* High-Frequency Dynamic Nuclear Polarization in MAS Spectra of Membrane and Soluble Proteins. *J. Am. Chem. Soc.* **125,** 13626–13627 (2003).
165. Wind, R. A., Duijvestijn, M. J., van der Lugt, C., Manenschijn, A. & Vriend, J. Applications of dynamic nuclear polarization in 13C NMR in solids. *Prog. Nucl. Magn. Reson. Spectrosc.* **17,** 33–67 (1985).
166. Goldman, M. *Spin Temperature and Nuclear Magnetic Resonance in Solids (Clarendon Press, Oxford)*. (1970).
167. Leeder, A. J. *et al.* Synthesis of isotopically labeled all- trans retinals for DNP-enhanced solid-state NMR studies of retinylidene proteins. *J. Label. Compd. Radiopharm.* 1–13 (2017). doi:10.1002/jlcr.3576
168. Hong, M. Solid-State Dipolar INADEQUATE NMR Spectroscopy with a Large Double-Quantum Spectral Width. *J. Magn. Reson.* **136,** 86–91 (1999).
169. Becker-Baldus, J. *et al.* Enlightening the photoactive site of channelrhodopsin-2 by DNP-enhanced solid-state NMR spectroscopy. *Proc. Natl. Acad. Sci.* **112,** 9896–9901 (2015).
170. Bruun, S. *et al.* Light–Dark Adaptation of Channelrhodopsin Involves Photoconversion between the all-trans and 13-cis Retinal Isomers. *Biochemistry* **54,** 5389–5400 (2015).
171. Evans, J. N. S. *Biomolecular NMR spectroscopy*. (Oxford University Press, 1995).

172. Stejskal, E. O. & Memory, J. D. *High resolution NMR in the solid state: fundamentals of CP/MAS*. (1994).
173. 齋藤肇, 安藤勲 & 内藤晶. *NMR分光学―基礎と応用―*. (東京化学同人, 2008).
174. Bertini, I., McGreevy, K. S. & and Parigi, G. *NMR of Biomolecules: Towards Mechanistic Systems Biology*. (Wiley-VCH Verlag GmbH & Co. KGaA, 2012). doi:10.1002/9783527644506
175. Manolikas, T., Herrmann, T. & Meier, B. H. Protein structure determination from 13C spin-diffusion solid-state NMR spectroscopy. *J. Am. Chem. Soc.* **130,** 3959–3966 (2008).
176. Szeverenyi, N. M., Sullivan, M. J. & Maciel, G. E. Observation of spin exchange by two-dimensional fourier transform 13C cross polarization-magic-angle spinning. *J. Magn. Reson.* **47,** 462–475 (1982).
177. Separovic, F. & Naito, A. *Advances in Biological Solid-State NMR: Proteins and Membrane-Active Peptides (New Developments in NMR)*. (2014). doi:Book_Doi 10.1039/9781782627449
178. Yomoda, H. *et al.* Color-discriminating retinal configurations of sensory rhodopsin i by photo-irradiation solid-state NMR spectroscopy. *Angew. Chemie - Int. Ed.* **53,** 6960–6964 (2014).
179. Tomonaga, Y. *et al.* An Active Photoreceptor Intermediate Revealed by In Situ Photoirradiated Solid-State NMR Spectroscopy. *Biophys. J.* **101,** L50–L52 (2011).
180. Li, H., Sineshchekov, O. A., da Silva, G. F. Z. & Spudich, J. L. In Vitro Demonstration of Dual Light-Driven Na+/H+ Pumping by a Microbial Rhodopsin. *Biophys. J.* **109,** 1446–1453 (2015).
181. Bertsova, Y. V, Arutyunyan, A. M. & Bogachev, A. V. Na+-translocating rhodopsin from Dokdonia sp. PRO95 does not contain carotenoid antenna. *Biochem.* **81,** 414–419 (2016).
182. Bogachev, A. V., Bertsova, Y. V., Verkhovskaya, M. L., Mamedov, M. D. & Skulachev, V. P. Real-time kinetics of electrogenic Na+ transport by rhodopsin from the marine flavobacterium Dokdonia sp. PRO95. *Sci. Rep.* **6,** 21397 (2016).
183. Kato, H. E. *et al.* Structural basis for Na+ transport mechanism by a light-driven Na+ pump. *Nature* **521,** 48–53 (2015).
184. Kwon, S.-K. *et al.* Genomic Makeup of the Marine Flavobacterium Nonlabens (Donghaeana) dokdonensis and Identification of a Novel Class of Rhodopsins. *Genome Biol. Evol.* **5,** 187–199 (2013).
185. Balashov, S. P. *et al.* Light-Driven Na + Pump from Gillisia limnaea : A High-Affinity Na + Binding Site Is Formed Transiently in the Photocycle. *Biochemistry* **53,** 7549–7561 (2014).
186. Kwon, Y. M., Kim, S. Y., Jung, K. H. & Kim, S. J. Diversity and functional analysis of light-driven pumping rhodopsins in marine Flavobacteria. *Microbiologyopen* **5,** 212–223 (2016).
187. Tsunoda, S. P. *et al.* Functional characterization of sodium-pumping rhodopsins with different pumping properties. *PLoS One* **12,** e0179232 (2017).
188. Yoshizawa, S. *et al.* Functional characterization of flavobacteria rhodopsins reveals a unique class of light-driven chloride pump in bacteria. *Proc. Natl. Acad. Sci.* **111,** 6732–6737 (2014).

189. Hoque, M. R. *et al.* A Chimera Na+-Pump Rhodopsin as an Effective Optogenetic Silencer. *PLoS One* **11,** e0166820 (2016).

190. Goto, K. *et al.* Functional analyses of Na+-pumping rhodopsin from Truepera radiovictrix. in *The 52nd Annual Meeting of the Biophysical Society of Japan* 1P247 (2014).

191. Ernst, O. P. *et al.* Microbial and Animal Rhodopsins: Structures, Functions, and Molecular Mechanisms. *Chem. Rev.* **114,** 126–163 (2014).

192. Inoue, K., Kato, Y. & Kandori, H. Light-driven ion-translocating rhodopsins in marine bacteria. *Trends Microbiol.* **23,** 91–98 (2015).

193. Kato, Y., Inoue, K. & Kandori, H. Kinetic Analysis of H + –Na + Selectivity in a Light-Driven Na + -Pumping Rhodopsin. *J. Phys. Chem. Lett.* **6,** 5111–5115 (2015).

194. da Silva, G. F. Z., Goblirsch, B. R., Tsai, A.-L. & Spudich, J. L. Cation-Specific Conformations in a Dual-Function Ion-Pumping Microbial Rhodopsin. *Biochemistry* **54,** 3950–3959 (2015).

195. Gushchin, I. *et al.* Crystal structure of a light-driven sodium pump. *Nat. Struct. Mol. Biol.* **22,** 390–395 (2015).

196. Inoue, K., Konno, M., Abe-Yoshizumi, R. & Kandori, H. The Role of the NDQ Motif in Sodium-Pumping Rhodopsins. *Angew. Chemie Int. Ed.* **54,** 11536–11539 (2015).

197. Konno, M. *et al.* Mutant of a Light-Driven Sodium Ion Pump Can Transport Cesium Ions. *J. Phys. Chem. Lett.* **7,** 51–55 (2016).

198. Melnikov, I. *et al.* Fast iodide-SAD phasing for high-throughput membrane protein structure determination. *Sci. Adv.* **3,** e1602952 (2017).

199. Henrich, E. *et al.* From Gene to Function: Cell-Free Electrophysiological and Optical Analysis of Ion Pumps in Nanodiscs. *Biophys. J.* **113,** 1331–1341 (2017).

200. Sato, M. *et al.* Role of Putative Anion-Binding Sites in Cytoplasmic and Extracellular Channels of Natronomonas pharaonis Halorhodopsin †. *Biochemistry* **44,** 4775–4784 (2005).

201. Ono, H., Inoue, K., Abe-Yoshizumi, R. & Kandori, H. FTIR Spectroscopy of a Light-Driven Compatible Sodium Ion-Proton Pumping Rhodopsin at 77 K. *J. Phys. Chem. B* **118,** 4784–4792 (2014).

202. Tahara, S. *et al.* Ultrafast Photoreaction Dynamics of a Light-Driven Sodium-Ion-Pumping Retinal Protein from Krokinobacter eikastus Revealed by Femtosecond Time-Resolved Absorption Spectroscopy. *J. Phys. Chem. Lett.* **6,** 4481–4486 (2015).

203. Suomivuori, C.-M., Gamiz-Hernandez, A. P., Sundholm, D. & Kaila, V. R. I. Energetics and dynamics of a light-driven sodium-pumping rhodopsin. *Proc. Natl. Acad. Sci.* **114,** 7043–7048 (2017).

204. Kandori, H., Inoue, K. & Tsunoda, S. P. Light-driven sodium-pumping rhodopsin : A new concept of active transport. *Chem. Rev.* (2018).

205. Gushchin, I. *et al.* Structure of the light-driven sodium pump KR2 and its implications for

optogenetics. *FEBS J.* **283,** 1232–1238 (2016).

206. Mogi, T., Stern, L. J., Marti, T., Chao, B. H. & Khorana, H. G. Aspartic acid substitutions affect proton translocation by bacteriorhodopsin. *Proc. Natl. Acad. Sci.* **85,** 4148–4152 (1988).
207. Shibata, M., Yoshitsugu, M., Mizuide, N., Ihara, K. & Kandori, H. Halide Binding by the D212N Mutant of Bacteriorhodopsin Affects Hydrogen Bonding of Water in the Active Site. *Biochemistry* **46,** 7525–7535 (2007).
208. Abe-Yoshizumi, R., Inoue, K., Kato, H. E., Nureki, O. & Kandori, H. Role of Asn112 in a Light-Driven Sodium Ion-Pumping Rhodopsin. *Biochemistry* **55,** 5790–5797 (2016).
209. Park, S. H. *et al.* Structure of the chemokine receptor CXCR1 in phospholipid bilayers. *Nature* **491,** 779–783 (2012).
210. Lakshmi, K. V *et al.* Solid State 13C and 15N NMR Investigations of the N Intermediate of Bacteriorhodopsin. *Biochemistry* **33,** 8853–8857 (1994).
211. Ahuja, S. *et al.* Helix movement is coupled to displacement of the second extracellular loop in rhodopsin activation. *Nat. Struct. Mol. Biol.* **16,** 168–175 (2009).
212. Eilers, M. *et al.* Structural Transitions of Transmembrane Helix 6 in the Formation of Metarhodopsin I. *J. Phys. Chem. B* **116,** 10477–10489 (2012).
213. Herzfeld, J. *et al.* Solid-state carbon-13 NMR study of tyrosine protonation in dark-adapted bacteriorhodopsin. *Biochemistry* **29,** 5567–5574 (1990).
214. Kato-Toma, Y., Iwashita, T., Masuda, K., Oyama, Y. & Ishiguro, M. pKa measurements from nuclear magnetic resonance of tyrosine-150 in class C beta-lactamase. *Biochem. J.* **371,** 175–181 (2003).
215. Zhu, J., Lau, J. Y. C. & Wu, G. A Solid-State 17 O NMR Study of l -Tyrosine in Different Ionization States: Implications for Probing Tyrosine Side Chains in Proteins. *J. Phys. Chem. B* **114,** 11681–11688 (2010).
216. Oshima, K. *et al.* Characterization of photo-intermediates in the photo-reaction pathways of a bacteriorhodopsin Y185F mutant using in situ photo-irradiation solid-state NMR spectroscopy. *Photochem. Photobiol. Sci.* **14,** 1694–1702 (2015).
217. Picas, L., Montero, M. T., Morros, A., Vázquez-Ibar, J. L. & Hernández-Borrell, J. Evidence of phosphatidylethanolamine and phosphatidylglycerol presence at the annular region of lactose permease of Escherichia coli. *Biochim. Biophys. Acta - Biomembr.* **1798,** 291–296 (2010).
218. Furutani, Y., Shimizu, H., Asai, Y., Oiki, S. & Kandori, H. Specific interactions between alkali metal cations and the KcsA channel studied using ATR-FTIR spectroscopy. *Biophys. Physicobiology* **12,** 37–45 (2015).
219. Oesterhelt, D. & Stoeckenius, W. Rhodopsin-like protein from the purple membrane of Halobacterium halobium. *Nat. New Biol.* **233,** 149–152 (1971).
220. Crocker, E. *et al.* Dipolar assisted rotational resonance NMR of tryptophan and tyrosine in

rhodopsin. *J. Biomol. NMR* **29,** 11–20 (2004).

221. Fung, B. M., Khitrin, A. K. & Ermolaev, K. An Improved Broadband Decoupling Sequence for Liquid Crystals and Solids. *J. Magn. Reson.* **142,** 97–101 (2000).
222. Shoji, A. *et al.* 15N NMR Chemical Shift Tensors and Conformation of Some 15N-Labeled Polypeptides in the Solid State. *Macromolecules,* **22,** 2860–2863 (1989).
223. Hempelmann, F. *et al.* His75−Asp97 Cluster in Green Proteorhodopsin. *J. Am. Chem. Soc.* **133,** 4645–4654 (2011).
224. Ding, X., Zhao, X. & Watts, A. G-protein-coupled receptor structure, ligand binding and activation as studied by solid-state NMR spectroscopy. *Biochem. J.* **450,** 443–457 (2013).
225. Farrar, M. R. *et al.* Solid state NMR study of [epsilon-13C]Lys-bacteriorhodopsin: Schiff base photoisomerization. *Biophys. J.* **65,** 310–315 (1993).
226. Eilers, M., Reeves, P. J., Ying, W., Khorana, H. G. & Smith, S. O. Magic angle spinning NMR of the protonated retinylidene Schiff base nitrogen in rhodopsin: Expression of 15N-lysine- and 13C-glycine-labeled opsin in a stable cell line. *Proc. Natl. Acad. Sci.* **96,** 487–492 (1999).
227. Harbison, G. S. *et al.* Dark-adapted bacteriorhodopsin contains 13-cis,15-syn and all-trans,15-anti retinal Schiff bases. *Proc. Natl. Acad. Sci. U. S. A.* **81,** 1706–1709 (1984).
228. Ono, H., Inoue, K., Abe-Yoshizumi, R. & Kandori, H. FTIR Spectroscopy of a Light-Driven Compatible Sodium Ion-Proton Pumping Rhodopsin at 77 K. *J. Phys. Chem. B* **118,** 4784–4792 (2014).
229. de Groot, H. J. M. *et al.* Solid-state 13C and 15N NMR study of the low pH forms of bacteriorhodopsin. *Biochemistry* **29,** 6873–6883 (1990).
230. Sharif, S., Denisov, G. S., Toney, M. D. & Limbach, H. H. NMR Studies of Coupled Low- and High-Barrier Hydrogen Bonds in Pyridoxal-5′-phosphate Model Systems in Polar Solution Shasad. *J. Am. Chem. Soc.* **129,** 6313–6327 (2007).
231. Inoue, K., Tsukamoto, T. & Sudo, Y. Molecular and evolutionary aspects of microbial sensory rhodopsins. *Biochim. Biophys. Acta - Bioenerg.* **1837,** 562–577 (2014).
232. Goncalves, J. A. *et al.* Highly conserved tyrosine stabilizes the active state of rhodopsin. *Proc. Natl. Acad. Sci.* **107,** 19861–19866 (2010).
233. Ding, X. *et al.* Mediation mechanism of tyrosine 185 on the retinal isomerization equilibrium and the proton release channel in the seven-transmembrane receptor bacteriorhodopsin. *Biochim. Biophys. Acta - Bioenerg.* **1857,** 1786–1795 (2016).
234. Kawamura, I., Kihara, N., Ohmine, M., Nishimura, K. & Tuzi, S. Solid-State NMR Studies of Two Backbone Conformations at Tyr185 as a Function of Retinal Configurations in the Dark , Light , and Pressure Adapted Bacteriorhodopsins. *J. Am. Chem. Soc.* **129,** 1016–1017 (2007).
235. Pfleger, N., Lorch, M., Woerner, A. C., Shastri, S. & Glaubitz, C. Characterisation of Schiff base and chromophore in green proteorhodopsin by solid-state NMR. *J. Biomol. NMR* **40,** 15–21

(2008).

236. Mak-Jurkauskas, M. L. *et al.* Energy transformations early in the bacteriorhodopsin photocycle revealed by DNP-enhanced solid-state NMR. *Proc. Natl. Acad. Sci.* **105,** 883–888 (2008).

237. Luecke, H., Schobert, B., Lanyi, J. K., Spudich, E. N. & Spudich, J. L. Crystal Structure of Sensory Rhodopsin II at 2.4 Angstroms: Insights into Color Tuning and Transducer Interaction. *Science (80-.).* **293,** 1499–1504 (2001).

238. Kawanabe, A. & Kandori, H. Photoreactions and Structural Changes of Anabaena Sensory Rhodopsin. *Sensors* **9,** 9741–9804 (2009).

239. Krebs, M. P. & Khorana, H. G. Mechanism of light-dependent proton translocation by bacteriorhodopsin. *J. Bacteriol.* **175,** 1555–1560 (1993).

240. Sudo, Y., Furutani, Y., Kandori, H. & Spudich, J. L. Functional Importance of the Interhelical Hydrogen Bond between Thr 204 and Tyr 174 of Sensory Rhodopsin II and Its Alteration during the Signaling Process. *J. Biol. Chem.* **281,** 34239–34245 (2006).

241. Shevchenko, V. *et al.* Sodium and Engineered Potassium Light-Driven Pumps. in *Optogenetics* (ed. Appasani, K.) 79–92 (Cambridge University Press, 2017). doi:10.1017/9781107281875.008

242. Nagel, G. *et al.* Channelrhodopsin-2, a directly light-gated cation-selective membrane channel. *Proc Natl Acad Sci U S A* **100,** 13940–13945 (2003).

243. Niho, A. *et al.* Demonstration of a Light-Driven SO 4 2– Transporter and Its Spectroscopic Characteristics. *J. Am. Chem. Soc.* **139,** 4376–4389 (2017).

244. Ito, S. *et al.* Unique Hydrogen Bonds in Membrane Protein Monitored by Whole Mid-IR ATR Spectroscopy in Aqueous Solution. *J. Phys. Chem. B* **122,** 165–170 (2018).

245. Hontani, Y. *et al.* The photochemistry of sodium ion pump rhodopsin observed by watermarked femto- to submillisecond stimulated Raman spectroscopy. *Phys. Chem. Chem. Phys.* **18,** 24729–24736 (2016).

246. Shigeta, A. *et al.* Solid-State Nuclear Magnetic Resonance Structural Study of the Retinal-Binding Pocket in Sodium Ion Pump Rhodopsin. *Biochemistry* **56,** 543–550 (2017).

247. Munowitz, M., Bachovchin, W. W., Herzfeld, J., Dobson, C. M. & Griffin, R. G. Acid-base and tautomeric equilibria in the solid-state - n-15 nmr-spectroscopy of histidine and imidazole. *J. Amer. Chem. Soc.* **104,** 1192–1196 (1982).

248. Liu, A. Z., Hu, W. D., Majumdar, A., Rosen, M. K. & Patel, D. J. NMR detection of side chain-side chain hydrogen bonding interactions in C-13/N-15-labeled proteins. *J. Biomol. NMR* **17,** 305–310 (2000).

249. Hu, J., Griffin, R. G. & Herzfeld, J. Synergy in the spectral tuning of retinal pigments: complete accounting of the opsin shift in bacteriorhodopsin. *Proc. Natl. Acad. Sci.* **91,** 8880–8884 (1994).

250. Mehler, M. *et al.* The EF Loop in Green Proteorhodopsin Affects Conformation and Photocycle dynamics. *Biophys. J.* **105,** 385–397 (2013).

251. Yoshitsugu, M., Shibata, M., Ikeda, D., Furutani, Y. & Kandori, H. Color Change of Proteorhodopsin by a Single Amino Acid Replacement at a Distant Cytoplasmic Loop. *Angew. Chemie Int. Ed.* **47,** 3923–3926 (2008).

252. Lanyi, J. K. Mechanism of Ion Transport. *J. Biol. Chem.* **204,** 18–21 (1997).

253. Lanyi, J. K. Molecular Mechanism of Ion Transport in Bacteriorhodopsin: Insights from Crystallographic, Spectroscopic, Kinetic, and Mutational Studies. *J. Phys. Chem. B* **104,** 11441–11448 (2000).

254. Roepe, P. D., Ahl, P. L., Herzfeld, J., Lugtenburg, J. & Rothschild, K. J. Tyrosine protonation changes in bacteriorhodopsin. A Fourier transform infrared study of BR548 and its primary photoproduct. *J. Biol. Chem.* **263,** 5110–5117 (1988).

255. Iwasa, T., Tokunaga, F. & Yoshizawa, T. Photochemical reaction of 13-cis-bacteriorhodopsin studied by low temperature spectroscopy. *Photochem. Photobiol.* **33,** 539–545 (1981).

256. Song, L., Yang, D., El-Sayed, M. A. & Lanyi, J. K. Retinal Isomer Composition in Some Bacteriorhodopsin Mutants under Light and Dark Adaptation Conditions. *J. Phys. Chem.* **99,** 10052–10055 (1995).

257. Dunach, M., Marti, T., Khorana, H. G. & Rothschild, K. J. Uv-visible spectroscopy of bacteriorhodopsin mutants: substitution of Arg-82, Asp-85, Tyr-185, and Asp-212 results in abnormal light-dark adaptation. *Proc. Natl. Acad. Sci.* **87,** 9873–9877 (1990).

258. Sonar, S., Krebs, M. P., Khorana, H. G. & Rothschild, K. J. Static and time-resolved absorption spectroscopy of the bacteriorhodopsin mutant Tyr-185 → Phe: Evidence for an equilibrium between bR570 and an O-like species. *Biochemistry* **32,** 2263–2271 (1993).

259. He, Y., Krebs, M. P., Fischer, W. B., Khorana, H. G. & Rothschild, K. J. FTIR Difference Spectroscopy of the Bacteriorhodopsin Mutant Tyr-185→Phe: Detection of a Stable O-like Species and Characterization of Its Photocycle at Low Temperature. *Biochemistry* **32,** 2282–2290 (1993).

260. He, Y., Krebs, M. P., Fischer, W. B., Khorana, H. G. & Rothschild, K. J. FTIR difference spectroscopy of the bacteriorhodopsin mutant Tyr-185 .fwdarw. Phe: Detection of a stable O-like species and characterization of its photocycle at low temperature. *Biochemistry* **32,** 2282–2290 (1993).

261. Rath, P., Krebs, M. P., He, Y., Khorana, H. G. & Rothschild, K. J. Fourier transform Raman spectroscopy of the bacteriorhodopsin mutant Tyr-185 .fwdarw. Phe: Formation of a stable O-like species during light adaptation and detection of its transient N-like photoproduct. *Biochemistry* **32,** 2272–2281 (1993).

262. Shibata, M. & Kandori, H. FTIR Studies of Internal Water Molecules in the Schiff Base Region of Bacteriorhodopsin. *Biochemistry* **44,** 7406–7413 (2005).

263. Richter, H. T., Needleman, R. & Lanyi, J. K. Perturbed interaction between residues 85 and 204

in Tyr-185-->Phe and Asp-85-->Glu bacteriorhodopsins. *Biophys. J.* **71,** 3392–3398 (1996).

264. Lakshmi, K. V. *et al.* Solid State 13C and 15N NMR Investigations of the N Intermediate of Bacteriorhodopsin. *Biochemistry* **33,** 8853–8857 (1994).
265. Harbison, G. S. *et al.* Solid-state carbon-13 NMR studies of retinal in bacteriorhodopsin. *Biochemistry* **23,** 2662–2667 (1984).
266. Smith, S. *et al.* Structure and Protein Environment of the Retinal Chromophore in Light- and Dark-Adapted Bacteriorhodopsin Studied. *Biochemistry* 8897–8904 (1989).
267. Oesterhelt, D. & Stoeckenius, W. Isolation of the Cell Membrane of Halobacterium halobium and Its Fractionation into Red and Purple Membrane. *Methods Enzym.* **31,** 667–678 (1974).
268. Kawamura, I. *et al.* Participation of the BC loop in the correct folding of bacteriorhodopsin as revealed by solid-state NMR. *Photochem. Photobiol.* **85,** 624–630 (2009).
269. Lozier, R. H., Bogomolni, R. A. & Stoeckenius, W. Bacteriorhodopsin: a light-driven proton pump in Halobacterium Halobium. *Biophys. J.* **15,** 955–962 (1975).
270. Bennett, A. E., Rienstra, C. M., Auger, M., Lakshmi, K. V. & Griffin, R. G. Heteronuclear decoupling in rotating solids. *J. Chem. Phys.* **103,** 6951–6958 (1995).
271. Lansing, J. C., Hu, J. G., Belenky, M., Griffin, R. G. & Herzfeld, J. Solid-State NMR Investigation of the Buried X−Proline Peptide Bonds of Bacteriorhodopsin †. *Biochemistry* **42,** 3586–3593 (2003).
272. Kawamura, I. *et al.* Dynamic aspects of extracellular loop region as a proton release pathway of bacteriorhodopsin studied by relaxation time measurements by solid state NMR. *Biochim. Biophys. Acta - Biomembr.* **1768,** 3090–3097 (2007).
273. Kawamura, I. *et al.* Solid-state NMR studies of two backbone conformations at Tyr185 as a function of retinal configurations in the dark, light, and pressure adapted bacteriorhodopsins. *J. Am. Chem. Soc.* **129,** 1016–1017 (2007).
274. Patzelt, H. *et al.* Towards structural investigations on isotope labelled native bacteriorhodopsin in detergent micelles by solution-state NMR spectroscopy. *J. Biomol. NMR* **10,** 95–106 (1997).
275. Rath, P., Krebs, M. P., He, Y., Khorana, H. G. & Rothschild, K. J. Fourier Transform Raman Spectroscopy of the Bacteriorhodopsin Mutant Tyr-185→Phe: Formation of a Stable O-like Species during Light Adaptation and Detection of Its Transient N-like Photoproduct. *Biochemistry* **32,** 2272–2281 (1993).
276. Sonar, S., Krebs, M. P., Khorana, H. G. & Rothschild, K. J. Static and time-resolved absorption spectroscopy of the bacteriorhodopsin mutant Tyr-185 .fwdarw. Phe: Evidence for an equilibrium between bR570 and an O-like species. *Biochemistry* **32,** 2263–2271 (1993).
277. Tuzi, S., Naito, A. & Saitô, H. Local protein structure and dynamics at kinked transmembrane α-helices of [1-13C]Pro-labeled bacteriorhodopsin as revealed by site-directed solid-state 13C

NMR. *J. Mol. Struct.* **654,** 205–214 (2003).

278. Hu, J. G., Griffin, R. G. & Herzfeld, J. Synergy in the Spectral Tuning of Retinal Pigments - Complete Accounting of the Opsin Shift in Bacteriorhodopsin. *Proc. Natl. Acad. Sci. U. S. A.* **91,** 8880–8884 (1994).

List of figures

List of tables

Acknowledgement

First of all, all works cannot be described without my supervisor Assoc. Prof. Izuru Kawamura. The three years of PhD under him gave so many memories that I don't know where to start, but one thing I have to write on here is that he was always supportive and gave his power fully to pull my knowledge and ability to the best. He always showed a step forward of what I see or think so that I can reach to the point. Step by step, I could develop my faculties in every direction with my speed. The projects here were conducted and concluded after the repeated discussion; in one of the projects the discussion was held every day over a month to understand the phenomenon and to come to the conclusion. During the time, intense data analysis and paper reading in short term with time pressure gave me confidence to be capable of harder tasks. The three years were very dense and I cannot thank enough for his teaching, help and encourage.

Secondly, Prof. Akira Naito who supervised me from my bachelor. He took a lead in my project, especially during my bachelor and master. The project on the bacteriorhodopsin taught me the delight of finding a new phenomenon which is barely reported. Without this project, I wouldn't have get the curiosity to the protein studies this much. Later in PhD, he supported me very much on discussions by giving me a new insight.

I would also show my great appreciation to my collaborator, Prof. Hideki Kandori, Assoc. Prof. Keiichi Inoue, Dr. Shota Ito, Dr. Rei Abe-Yoshizumi and Ms. Sahoko Tomida at Nagoya Institute of Technology. When my supervisor first brought me a new project of KR2, I was thrilled to be able to collaborate with Kandori group. Several visits for sample preparation and discussions and discussions over mail and phone calls always raised my motivation to the research projects. They always indirectly kept reminding me of what a powerful researcher is and what I need to be like them.

In addition to them, Professor Akimori Wada and Dr. Takashi Okitsu at Kobe Pharmaceutical University provided specifically labeled retinal and Professor Satoru Tuzi at University of Hyogo supported us by providing mutant strains of *H. salinarum*.

I would acknowledge Prof. Chojiro Kojima, Prof. Kensei Kobayashi, Prof. Yoshihiro Kubota, and Prof. Kazuhisa Sakakibara for my thesis examination.

All my work has been done with all support from all the lab members I spent with and I would like to show my appreciation here.

Last but not least. I am grateful to my parents for supporting nine-years of my university days for all aspects.

13. Mar. 2018

Arisu Shigeta